NOISE TRANSMISSION PATH IDENTIFICATION IN A RECIPROCATING FREON COMPRESSOR

by

David Larry Young, Jr.

Thesis submitted to the Faculty of the

Virginia Polytechnic Institute and State University

in partial fulfillment of the requirements for the degree of

MASTER OF SCIENCE

in

Mechanical Engineering

APPROVED:

L. D. Mitchell

L.D. Mitchell, Chairman

C.J. Hurst

C E Knight

C.E. Knight

August, 1995

Blacksburg, Virginia

NOISE TRANSMISSION PATH IDENTIFICATION IN A RECIPROCATING FREON COMPRESSOR

by

David Larry Young, Jr.

Committee Chairman: Larry D. Mitchell
Mechanical Engineering

(ABSTRACT)

A hermetic reciprocating freon compressor was instrumented for noise transmission path identification. A mix of force gages, pressure transducers, and an accelerometer were installed to identify the main transmission paths. Triaxial force gages were installed and calibrated to measure the three forces transmitted from each suspension spring to the shell. The three triaxial force gages, along with a pressure transducer measuring the dynamic pressure inside the shell, were used in a multiple reference frequency response function (FRF) analysis with the sound pressure from an external microphone as the reference output. The multiple reference FRF analysis indicates that the suspension springs are the dominant noise transmission path in this compressor.

A scanning laser velocimeter was used to measure the operating shape of one of the compressor harmonic responses. This harmonic shape was interesting because it is a significant sound radiator at a frequency well below the first structural mode identified by both experimental modal and finite element model analysis. The vibration pattern appears to be a combination of rigid-body motion of the compressor shell in response to

the orbiting spring forces and a circumferential acoustic mode inside the shell. The sound intensity pattern radiated by a regular version of the same compressor model closely resembles the vibration pattern driven by the rigid-body motion. This indicates that the spring forces actually drive the sound radiation at this frequency.

ACKNOWLEDGEMENTS

I would like to thank my advisor, Dr. Larry Mitchell for his input and guidance during the Bristol Project and for his patience with the extended preparation time of this thesis. Thanks go to Dr. Hurst and Dr. Knight who also collaborated on the Bristol Project, and to David Gilliam who served as our liaison with Bristol Compressors. Thanks also go to Bristol Compressors, Inc. and the Virginia Center for Innovative Technology for their funding of this research.

TABLE OF CONTENTS

LIST OF FIGURES

NOMENCLATURE

x	Input time history
y	Output time history
n	Noise time history
h	Impulse response function
X	Input linear spectrum
Y	Output linear spectrum
N	Noise linear spectrum
H	Frequency response function
R	Correlation function
$E[\ ]$	Expectation operator
S	Two-sided power density function
G	One-sided power density function
f	Frequency
*	Complex conjugate
T	Time period
τ	Time delay
γ^2	Coherence
^{T}	Hermitian transpose
m	Number of system inputs
$\hat{}$	Estimate, prediction
L	Conditioned frequency response function
$'$	Virtual coherence function component
t	Time
ζ	Damping ratio
B_e	Resolution bandwidth
B_r	Half-power point bandwidth

1.0 INTRODUCTION

Reciprocating freon compressors are commonly used in industrial and residential air conditioning and heat pump applications. Compressor manufacturers are interested in understanding how internal, structural, and acoustical energy travels to become acoustical energy outside of the sealed shell. Basic understanding of this nature will allow new designs to be developed that will be quieter than present units.

1.1 Project Overview

This project began with a request from Bristol Compressors, Inc. for help in reducing the acoustic noise emissions of the H23A compressor. The H23A is a hermetically sealed two-cylinder reciprocating freon compressor line with cooling capacities ranging from 2.5 to 5 tons (8.8 to 17.6 kW). The problem was approached by a team of three groups specializing in the acoustic modeling and analysis, experimental modal analysis, and finite element modeling. The acoustics group identified the frequencies with significant acoustic radiation levels and the associated acoustic intensity patterns of the shell of an operating compressor. The modal analysis group identified the resonance frequencies and vibration patterns of the compressor shell, valve plate assembly, and assembled compressor. The results of this dynamic finite element analysis were compared with the results of the experimental modal analysis to validate and refine the finite element model of the shell.

As this initial phase of the project was nearing completion, the main goal of the project was expanded. This new goal was to put in place at Bristol Compressors the technology to prevent the design of new compressors that produce significant acoustic noise. The development of this technology will require a multiple disciplinary approach consisting of acoustic modeling and measurement, experimental modal analysis, mechanical forcing function measurement and prediction, and finite element modeling. The expected interaction of these disciplines is shown in Fig. 1-1. The development of this technology is expected to be a long-term effort.

1.2 Goals of the Experimental Analysis

This experimental analysis of the H23A compressor is part of the long-term technology development concentrating on the mechanical and acoustic forcing functions. The primary goal of the experimental analysis is to identify and to quantify the mechanical and acoustic transmission paths that drive the compressor shell acoustic noise radiation. The identification of the acoustic and mechanical noise sources in the compressor is also desired. This is accomplished by instrumenting the compressor with a strategic mix of force gages, pressure transducers, and accelerometers. The force gages can measure the forces that are transmitted to the shell by the compressor support springs.

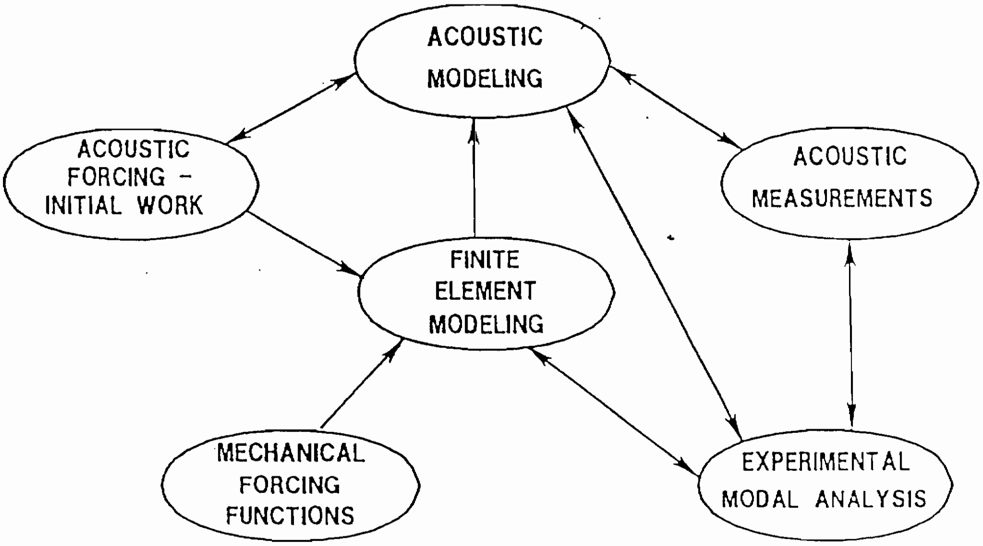

Fig. 1-1: Expected interaction of the disciplines required to design quieter compressors (after [1])

These are measurements that should give a good representation of the mechanical forcing functions driving the shell. These forcing functions can then be used to drive the finite element model of the assembled compressor. The dynamic response of the finite element model driven by these forces can be sent to an acoustic radiation prediction program. The acoustic predictions can be compared to the acoustic measurements of an operating compressor to verify and refine the accuracy of the finite element model along with the experimental measurement and analysis.

This experimental analysis requires the instrumentation of a H23A623 compressor which contains a single-phase electric motor and has a cooling capacity of 5 tons (17.6 kW). The output of the various transducers are measured with a Zonic System 7000 multichannel fast Fourier transform analyzer and the data is stored on a Hewlett Packard 385 workstation. Several methods for analyzing the content of the measured signals and identifying the relationships between the internal measurements and the external microphone measurement are used to ascertain the primary noise paths in the compressor and the probable sources. When the primary mechanical and acoustic paths are identified, the necessary compressor modifications can be determined with a high probability of reducing the noise radiation levels. If these modifications are effective then the validity of the methods and analysis is supported.

1.3 Literature Review

A search was initiated of the available literature on noise source and path identification methods. The ideal method identifies the primary transmission paths along with their contribution to the external noise measured by the microphone. The instrumentation for the test compressor was selected with the goal of having each measured signal representing one of the potential transmission paths or internal sources. The reciprocating compressor is a harmonically driven system so that high correlation between the measurements is expected. This resulted in a literature search that concentrated on methods to solve the multiple-input/single-output (MISO) model with correlated inputs. The derivation and application of these MISO model solutions are presented in Chapter 2.

The basic principles and statistics of signal measurement and processing, including the multiple-input/output relationships, are covered in several texts written by Bendat and Piersol [2,3]. These two texts cover the statistics, error sources, and the basic computational algorithms for the MISO problem in detail. Several papers cover various aspects of the input/output relationships. Bendat and Halvorsen [4] look at the basics of the single input-single output model concentrating on the common error sources and how to minimize them. Dodds and Robson [5] present the basics of partial coherence analysis. Partial coherence attempts to remove the correlated portion of each input through conditioning. The inputs are processed in order removing the portion of each input that is correlated to the inputs processed before it. The frequency response functions and coherence between the conditioned inputs and the output can then be solved and provide insight into the structure of the system. A disadvantage of this method is the solution is dependent on the input order. If the order of the inputs is changed, the solution is likely to change.

Another analysis method is to solve for the optimal frequency response functions for the actual system inputs. In this analysis the importance of a source or path can be determined by calculating the model output as if the input signal passing through its frequency response function (FRF) were blocked. This solution has an advantage over the partial coherence analysis since it solves the model for the actual inputs but it does not provide a simple coherence value relationship between the inputs and outputs like the conditioned partial coherence analysis. Romberg [6] provides a computational algorithm for solving the multiple input problem. Bendat [7] concentrates on the statistical errors in the analysis of SISO and MISO systems. Seybert and Hamilton [8] concentrate on errors caused by time delay between the input and the output, which can be a problem in acoustic measurements since it takes time for a pressure wave to travel from a structure to the microphone. Bendat [9] presents some of the more recent analysis procedures for multiple input/output problems.

There are several sources that describe applications of the multiple-input/output methods. Trethewey and Evensen [10,11,12,13,14,15] successfully developed and applied multiple-input modeling techniques to identify the structural noise generating mechanisms in gravity-drop forge hammers. The vibrations of the structural members of the forge hammer were correlated to a microphone measurement during each cycle of the hammer operation. This followed the work by Chung, Crocker, and Hamilton [16] and Alfredson [17] on the identification of the noise mechanisms in diesel engines. Chung, Crocker, and Hamilton determined the frequency response functions between the cylinder pressure measurements and the sound pressure measured with a microphone. Alfredson used near-field microphones to identify the areas of the engine surface that were radiating significant acoustic noise and correlated them to a microphone farther away from the engine. He used both the optimal FRF solution and the partial coherence analysis.

A different method of analyzing the multiple-input/output model was developed and applied by Price and Bernhard [18], Leuridan, Roesens, and Otte [19], and Otte, Sas, and Snoeys [20]. This method attempts to remove the correlation between the inputs as in the partial coherence analysis. The inputs are uncorrelated by performing a singular valued decomposition of the input cross-spectral matrix which determines the uncorrelated components of the measured inputs. The frequency response functions and coherence between these linearly independent virtual inputs, or principal components, and the measured output can be calculated. The relationship between the transformed virtual inputs and the physical, measured inputs is not very clear. Ufford and Bernhard [21,22] presented a technique for analyzing the multiple-input/output model by performing singular valued decompositions of the input, output, and the augmented cross-spectral matrices to determine the number of dominant independent components in the input and output measurements. This "Number of Incoherent Sources" (NIS) technique can give an indication of the number of independent sources in the input and output but requires a basic understanding of the system to interpret.

1.4 Summary of Thesis Arrangement

This thesis is divided into seven chapters. The first is the introduction which presents the project overview, goals of the experimental analysis, and literature review. The second chapter introduces the basis and derivation of the spectral multiple input models for source identification. These models include Partial Coherence analysis, Multiple FRF analysis, and a brief explanation of recent developments in Virtual Coherence and related methods of analysis. The third chapter describes the hardware selection, installation, calibration, and compressor assembly response changes caused by the instrumentation installation. The fourth chapter details the experimental analysis of the compressor including the transducer measurements and multiple-reference FRF analysis. The fifth chapter describes the setup and measurement of the 343 Hz operating shape of the compressor using a scanning laser velocimeter. This operating shape was measured because of high sound radiation at a frequency well below the structural mode frequencies. The sixth and seventh chapters cover the conclusions and recommendations, respectively. Appendix A lists the transducers that were installed in the instrumented compressor. Appendix B contains the linear spectrums, in magnitude and phase format, for the measured time signals presented in the fourth chapter.

2.0 MULTIPLE-INPUT/OUTPUT MODELS

This chapter will develop the basic theory and application of multiple-input/output frequency-domain models for system analysis. The basic theory of linear systems and frequency response function (FRF) estimation are developed for the single input-single output (SISO) model, then extended to multiple input-single output (MISO) problems. The common sources of error in the measurement of data and their effects are also presented. The statistics that support the modeling process are not presented in this chapter but are explained in detail in several sources [2,3]. The general presentation of the MISO model development follows that of Trethewey [15].

2.1 Linear Systems

The frequency-domain analysis methods assume a constant parameter linear system that is physically realizable and stable. The output, or response, of this type of system, shown in Fig. 2-1, is related to the input, or excitation, by the convolution integral:

$$y(t) = \int_{-\infty}^{\infty} h(\tau)x(t-\tau)d\tau \tag{2.1}$$

where $x(t)$ and $y(t)$ are the respective time histories of the input and output and $h(\tau)$ is the unit impulse response which describes the dynamic characteristics of the system. A

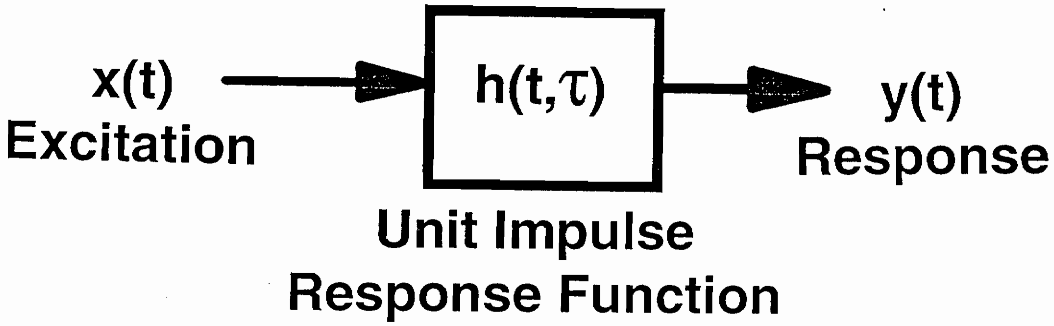

Fig. 2-1: Linear constant parameter system

physically realizable system cannot respond to the input until it is applied. This requires the unit impulse function to be zero until the input is applied. A stable system produces a bounded output in response to any possible bounded input. The output of a linear system, which is additive and homogeneous, is independent of the type or magnitude of the input. An additive system requires the output in response to the sum of several different input signals is equal to the sum of the outputs in response to each of the input signals. A homogenous system will produce the output $Cy(t)$ in response to the input $Cx(t)$ when C is an arbitrary constant. These are the basic assumptions in the formulation of the analysis of linear systems.

The response $y(t)$ can be difficult to determine from Eq. (2.1). The Fourier transform of the convolution integral yields the simpler multiplication relationship:

$$Y(f) = H(f)X(f) \tag{2.2}$$

in the frequency domain. The Fourier transforms are defined as:

$$X(f) = \int_{-\infty}^{\infty} x(\tau)e^{-i2\pi f\tau}d\tau \tag{2.3}$$

$$Y(f) = \int_{-\infty}^{\infty} y(\tau)e^{-i2\pi f\tau}d\tau \tag{2.4}$$

$$H(f) = \int_{-\infty}^{\infty} h(\tau)e^{-i2\pi f\tau}d\tau \tag{2.5}$$

The FRF $H(f)$ is a complex function in the frequency domain which contains all the dynamic characteristics of the system. This FRF can be expressed in either the rectangular coordinate form with real and imaginary components or in the polar form with magnitude and phase. The magnitude $|H(f)|$ is commonly referred to as the gain factor and $\phi(f)$ is the phase. The gain factor represents the amplification of the input signal and the phase describes the delay between the input and output signals.

The frequency response function, as shown in Eq. (2.2), is equivalent to the ratio of the excitation and response Fourier transforms:

$$H(f)=Y(f)/X(f) \tag{2.6}$$

which implies that the FRF of an unknown system can be determined from knowledge of its response to a known input. The integrals in Eqs. (2.3,2.4) are impossible to evaluate when $x(t)$ and $y(t)$ are continuous random signals. Because of this problem it is not possible in many cases to determine the FRF directly from Eq. (2.6). Instead consider the auto and cross correlation functions:

$$R_{XX}(\tau) = E[x(t)x(t+\tau)] = \lim_{T\to\infty} \frac{1}{2T}\int_{-T}^{T} x(t)x(t+\tau)dt \tag{2.7}$$

$$R_{YY}(\tau) = E[y(t)y(t+\tau)] = \lim_{T\to\infty} \frac{1}{2T}\int_{-T}^{T} y(t)y(t+\tau)dt \tag{2.8}$$

$$R_{XY}(\tau) = E[x(t)y(t+\tau)] = \lim_{T\to\infty} \frac{1}{2T}\int_{-T}^{T} x(t)y(t+\tau)dt \tag{2.9}$$

where $E[\ \ ]$ is an expectation operator. These correlation functions contain the statistical characteristics of the original time histories but cannot be transformed back to the time histories themselves. The Fourier transforms of the correlation functions can be evaluated if the functions exist and satisfy the conditions:

$$\int_{-\infty}^{\infty} |R(\tau)| \, d\tau < \infty \quad \textit{and} \quad R(\tau \rightarrow \infty) = 0 \tag{2.10}$$

Most physical signals satisfy this condition which means frequency-domain information can be obtained for time signals whose Fourier transforms cannot be evaluated.

The Fourier transforms of the correlation functions yield the following relationships between the two-sided auto and cross-spectral power density functions and the corresponding correlation functions:

$$S_{XX}(f) = \int_{-\infty}^{\infty} R_{XX}(\tau) e^{-i2\pi f} \, d\tau \qquad -\infty \leq f \leq \infty \tag{2.11}$$

$$S_{YY}(f) = \int_{-\infty}^{\infty} R_{YY}(\tau) e^{-i2\pi f} \, d\tau \qquad -\infty \leq f \leq \infty \tag{2.12}$$

$$S_{XY}(f) = \int_{-\infty}^{\infty} R_{XY}(\tau) e^{-i2\pi f} \, d\tau \qquad -\infty \leq f \leq \infty \tag{2.13}$$

These relations are called the *Wiener-Khinchine relations* in honor of the mathematicians, N. Wiener and A.I. Khinchine, who independently proved this Fourier transform relationship. The autospectral density functions S_{XX} and S_{YY} are real nonnegative even functions of f while the cross-spectral density S_{XY} is a complex function of f. To simplify the interpretation of the frequency the one-sided power spectral density functions are often used:

$$G_{XX}(f) = 2S_{XX}(f) \qquad 0 \le f \le \infty \tag{2.14}$$

$$G_{YY}(f) = 2S_{YY}(f) \qquad 0 \le f \le \infty \tag{2.15}$$

$$G_{XY}(f) = 2S_{XY}(f) \qquad 0 \le f \le \infty \tag{2.16}$$

The power spectral density functions can be determined by using the expected values of the Fourier transforms of the time-history signals:

$$G_{XX}(f) = 2 \lim_{T \to \infty} \frac{1}{T} E[X^*(f,T)X(f,T)] \tag{2.17}$$

$$G_{YY}(f) = 2 \lim_{T \to \infty} \frac{1}{T} E[Y^*(f,T)Y(f,T)] \tag{2.18}$$

$$G_{XY}(f) = 2 \lim_{T \to \infty} \frac{1}{T} E[X^*(f,T)Y(f,T)] \tag{2.19}$$

where the * denotes the complex conjugate. In practical applications T is finite and the data is discrete instead of continuous. Because of this condition, the estimates of the spectral density functions is improved by averaging n distinct records using the relations:

$$G_{XX}(f) = \frac{2}{nT} \sum_{i=1}^{n} [X_i^*(f,T)X_i(f,T)] \tag{2.20}$$

$$G_{YY}(f) = \frac{2}{nT} \sum_{i=1}^{n} [Y_i^*(f,T) Y_i(f,T)] \tag{2.21}$$

$$G_{XY}(f) = \frac{2}{nT} \sum_{i=1}^{n} [X_i^*(f,T) Y_i(f,T)] \tag{2.22}$$

where n is the number of records of time duration *T* that are averaged. These estimates are subject to bias and estimation errors which will be discussed in section 2.6.

Multiplying both sides of Eq. (2.2) by $2/T\, X^*(f)$ and using the expectation function yields the relationship:

$$\frac{2}{T} E[X_i^*(f,T) Y_i(f,T)] = H(f) \frac{2}{T} E[X_i^*(f,T) X_i(f,T)] \tag{2.23}$$

Both sides of Eq. (2.2) can be multiplied by $2/T\; Y^*(f)$ and applying the expectation function yields another relationship:

$$\frac{2}{T} E[Y_i^*(f,T) Y_i(f,T)] = H(f) \frac{2}{T} E[Y_i^*(f,T) X_i(f,T)] \tag{2.24}$$

These two equations imply that the frequency response function can be estimated from the ratio of an autospectrum and the cross-spectrum. The FRF implied in Eq. (2.3) is referred to as the H_1 estimator and has the form:

$$H_1(f) = \frac{G_{XY}(f)}{G_{XX}(f)} \tag{2.25}$$

The other FRF estimator is not as commonly used and is known as the H_2 estimator and has the form:

$$H_2(f) = \frac{G_{YY}(f)}{G_{YX}(f)} \tag{2.26}$$

These two relationships can estimate the dynamic characteristics of a system by using the input and output Fourier transforms of the system. The H_1 estimator is not sensitive to output extraneous noise and the H_2 estimator is not sensitive to input noise. There are several other FRF estimators that have been developed such as the H_c [23,24], H_v [25], and H_s [26] estimators. Each estimator makes a different assumption on the characteristic of the extraneous noise in the system input and output and some are limited to use with single input systems.

The ordinary coherence function, which applies to all of the estimators, defined by:

$$\gamma^2(f) = \frac{G_{XY}(f)G_{YX}(f)}{G_{XX}(f)G_{YY}(f)} \tag{2.27}$$

is a measure of the correlation between the input and output signals. It is a real-valued function of f with a value between 0 and 1. When the output is highly correlated with the input the coherence value will be near unity and near zero when the two are not related. The coherence is an index which indicates the potential error in the FRF estimation. Coherence values near unity indicate an accurate FRF estimate and low coherence values introduce uncertainty about the estimation. The auto and cross-spectrums used in the FRF and coherence calculations need to be the averaged from a number of distinct blocks of time data. This averaging smooths the power spectra estimates and reduces the effects of some errors that are present with discretely sampled time data.

In normal applications the coherence will not equal unity because of conditions that violate those of the ideal linear system. Most of the major sources of error in multiple-input modeling will be covered in Section 2.6. One of the most common conditions is extraneous noise in the measurements. Precautions must be taken to prevent extraneous noise from becoming a significant part of an input or output measurement. Bias errors in the spectral estimate will also reduce the coherence. There are several sources of bias error including resolution bias error from using too wide of a bandwidth, or too low of a frequency resolution, in the analysis. There are also bias errors in the FRF estimates that result when too few of data records are used for averaging. A nonlinear system will reduce the coherence since there is not a constant linear relationship between the input and output. The output is not linearly related to and, thus, not highly coherent with the input. The FRF for a nonlinear system will be some linearized fit between the input and output. Another condition that can reduce the coherence is when the measured inputs are not the only sources contributing to the output, that is, there is another unmeasured input that is driving the system. When analyzing FRF's it is always good practice to check the coherence to determine the degree of confidence in the estimate.

2.2 Estimation of Optimal Frequency Response Functions

The development of the FRF estimator relation given in Eq. (2.23) assumes that the response is totally due to the input passing through the system. This does not address the problem of extraneous noise in the input or output signals. One expected problem, especially in acoustic measurements outside of an anechoic environment, is noise in the output signal. The output $y(t)$ is then the sum of the actual system output and the noise. The noise $n(t)$ can represent either extraneous noise, such as AC power, line noise, background environmental acoustic noise, or the system response to an input other than the measured $x(t)$.

It is important to determine if the FRF estimator will accurately determine the true FRF under the condition of output noise. The relationship between the output and excitation for the system represented in Fig. 2-2 is:

$$Y(f) = H(f)X(f) + N(f) \tag{2.28}$$

where $Y(f)$, $H(f)$, and $X(f)$ are defined in Eqs. (2.3,2.4,2.5) and $N(f)$ is the Fourier transform of the noise $n(t)$. The relationship for $N(f)$ and its complex conjugate in terms of the other variables are:

$$N(f) = Y(f) - H(f)X(f) \tag{2.29}$$

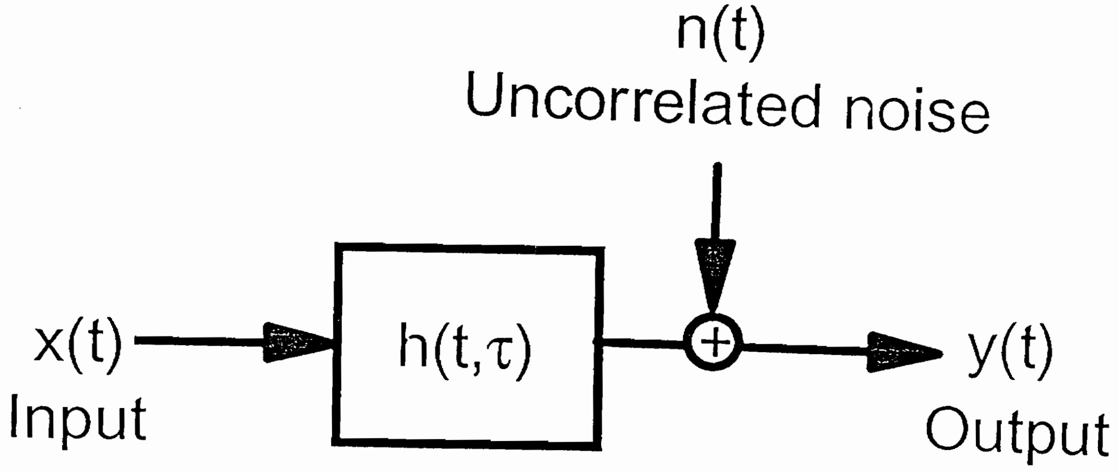

Fig. 2-2: Single input - single output system with uncorrelated output noise

$$N^*(f) = Y^*(f) - H^*(f)X^*(f) \tag{2.30}$$

Multiplying Eq. (2.29) by Eq. (2.30) and performing the expectation of the product yields:

$$\begin{aligned} E[N^*(f)N(f)] &= E[Y^*(f)Y(f)] - H(f)E[X(f)Y^*(f)] \\ &\quad - H^*(f)E[X^*(f)Y(f)] + H(f)H^*(f)E[X^*(f)X(f)] \end{aligned} \tag{2.31}$$

Multiplying by *2/T* and using the relations of Eqs. (2.20,2.21,2.22) this equation becomes in the limit:

$$\begin{aligned} G_{nn}(f) &= G_{yy}(f) - H(f)G_{yx}(f) - H^*(f)G_{xy}(f) \\ &\quad + H^*(f)H(f)G_{xx}(f) \end{aligned} \tag{2.32}$$

where $G_{nn}(f)$ is the autospectrum of the uncorrelated noise. The FRF estimate of $H(f)$ which minimizes $G_{nn}(f)$ in the least-squares sense is desired. By holding $H^*(f)$ constant, taking the partial derivative of $G_{nn}(f)$ with respect to $H(f)$ and setting it to zero, the following result is obtained:

$$\frac{\partial G_{nn}(f)}{\partial H(f)} = -G_{yx}(f) + H^*(f)G_{xx}(f) = 0 \tag{2.33}$$

Rearranging for the FRF relationship yields:

$$H^*(f) = \frac{G_{yx}(f)}{G_{xx}(f)} \tag{2.34}$$

If this process is repeated with $H(f)$ held constant and the partial derivative is taken with respect to $H^*(f)$, it yields the following result:

$$H(f) = \frac{G_{xy}(f)}{G_{xx}(f)} \tag{2.35}$$

The least squares estimates in Eq. (2.34,2.35) are equal to the expression developed in Eq. (2.25), which indicates that the H_1 estimator will yield the correct representation of the system when the noise term $n(t)$ is uncorrelated with the input $x(t)$. Improper estimates will be made, however, if there is noise at the input which will contaminate the estimate by making the denominator of Eq. (2.35) $G_{xx}(f)+G_{mm}(f)$, where m is the subscript indication of input noise.

The H_1 estimator will yield an accurate FRF in the presence of uncorrelated output noise. Uncorrelated noise in the input or output signals will lower the coherence value from unity for the H_1 and H_2 estimators and introduce uncertainty into the estimates produced by these two estimators. If noise on the input is assumed and minimized in the FRF estimator development presented above, the H_2 estimator will result. Noise on the input will yield an H_1 FRF estimate that is biased low and noise on the output will yield an H_2 FRF estimate that is biased high relative to the actual FRF. The H_1 and H_2 estimators can be used to find the upper and lower bounds of the FRF estimate. The FRF estimates are biased since the uncorrelated noise will add to the autospectrum value while the cross-spectrum will remain unbiased. It is difficult in many cases to determine the exact source of error except in situations where the H_c [23,24] estimator can be applied. A coherence value near unity for both estimators indicates an accurate FRF estimate but a low value does not indicate a poor FRF estimate if the proper estimator is used.

2.3 Multiple Input System Modeling

The concepts developed for single-input systems can be easily extended to the multiple-input/single-output system shown in Fig. 2-3. The system output $y(t)$ is the summation of the outputs $y_i(t)$ which are generated by the m inputs $x_i(t)$ passing through m distinct transmission paths H_i. Beginning with the system output summation relationship:

$$y(t) = \sum_{i=1}^{m} y_i(t) \tag{2.36}$$

and combining with Eq. (2.1):

$$y(t) = \sum_{i=1}^{m} \int_{-\infty}^{\infty} h_i(\tau) x_i(t-\tau) d\tau \tag{2.37}$$

Taking the Fourier transforms of both sides Eq. (2.37) becomes:

$$Y(f) = \sum_{i=1}^{m} H_i(f) X_i(f) \tag{2.38}$$

Multiplying this by $2/T\ Y^*(f)$, where $Y^*(f)$ is the complex conjugate of the system output, and performing the expectation leads to the autospectrum of the system output:

$$G_{yy} = \sum_{i=1}^{m} H_i(f) G_{yi}(f) \tag{2.39}$$

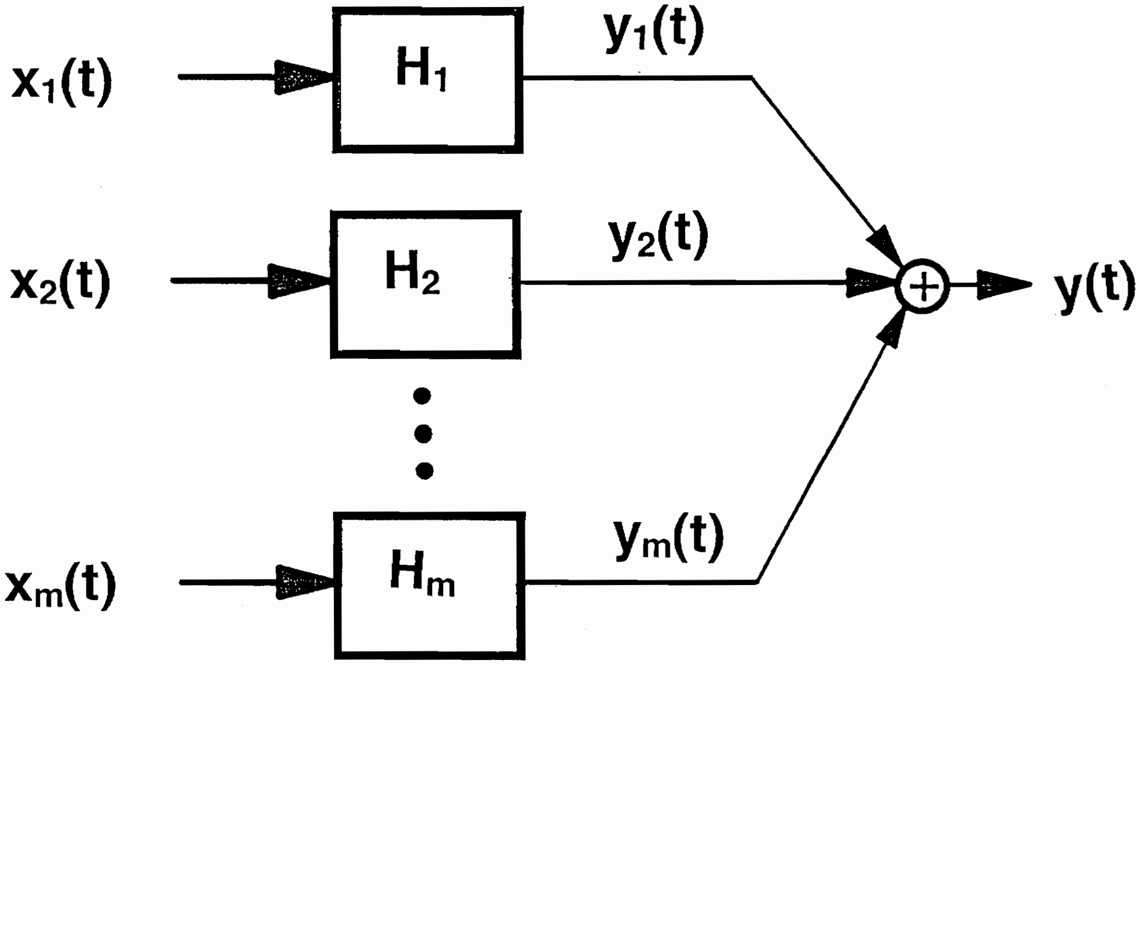

Fig. 2-3: Multiple input - single output system

Similarly, taking Eq. (2.38) and multiplying by $2/T\, X_i^*(f)$, where $X_i^*(f)$ is the complex conjugate of the Fourier transform of the i^{th} input, and performing the expectation yields:

$$G_{iy}(f) = \sum_{j=1}^{m} H_j(f) G_{ij}(f) \tag{2.40}$$

Recognizing that $G_{yi}(f) = G^*_{iy}(f)$, Eqs. (2.39,2.40) can be combined to obtain:

$$G_{yy}(f) = \sum_{i=1}^{m} \sum_{j=1}^{m} H_i^*(f) H_j(f) G_{ij}(f) \tag{2.41}$$

where $G_{ij}(f)$ is the cross-spectrum between the i^{th} and j^{th} inputs and when $i = j$ it is the autospectrum of i^{th} input. This equation states that the output autospectrum can the expressed as the summation of the products of the appropriate auto and cross spectral terms of the m inputs and the m frequency response functions.

This relationship between the input auto and cross spectrums and the outputs can be represented by the following matrix relationship:

$$[G_{xx}(f)]\{H(f)\} = \{G_{xy}\} \tag{2.42}$$

where $[G_{xx}(f)]$ is a m x m matrix called the input spectral density matrix which contains the input autospectra on the diagonal and the cross-spectral terms off the diagonal as follows:

$$[G_{xx}(f)] = \begin{bmatrix} G_{11}(f) & G_{12}(f) & G_{13}(f) & \cdots & G_{1m}(f) \\ \vdots & \vdots & \vdots & & \vdots \\ G_{m1}(f) & G_{m2}(f) & G_{m3}(f) & \cdots & G_{mm}(f) \end{bmatrix} \tag{2.43}$$

The input spectral density matrix is Hermitian which means it can be totally defined by the upper or lower triangular portion of the matrix since $G_{ij}^{*}(f) = G_{ji}(f)$. The m dimensional FRF vector $\{H(f)\}$ and input-output cross-spectral vector $\{G_{xy}(f)\}$ are represented as follows:

$$\{H(f)\} = \begin{Bmatrix} H_1(f) \\ H_2(f) \\ \bullet \\ \bullet \\ \bullet \\ H_m(f) \end{Bmatrix} \qquad \{G_{xy}(f)\} = \begin{Bmatrix} G_{1y}(f) \\ G_{2y}(f) \\ \bullet \\ \bullet \\ \bullet \\ G_{my}(f) \end{Bmatrix} \tag{2.44}$$

The matrix form of the output autospectrum relationship given in Eq. (2.41) is:

$$G_{yy}(f) = \{H^{*}(f)\}^{T}\,[G_{xx}(f)]\,\{H(f)\} \tag{2.45}$$

The FRF vector for a system can be determined by solving the matrix relationship in Eq. (2.42). The input spectral density matrix and the input-output cross-spectral vector can be estimated from the physical inputs and output of the system. The development of the model for multiple inputs presented above assumes that the output is entirely due to the linear effects of the m inputs. If the model is extended to account for uncorrelated noise at the output as shown in Fig. 2-4, the Fourier transform of the output becomes:

$$Y(f) = \sum_{i=1}^{m} Y_i(f) + N(f) \tag{2.46}$$

where

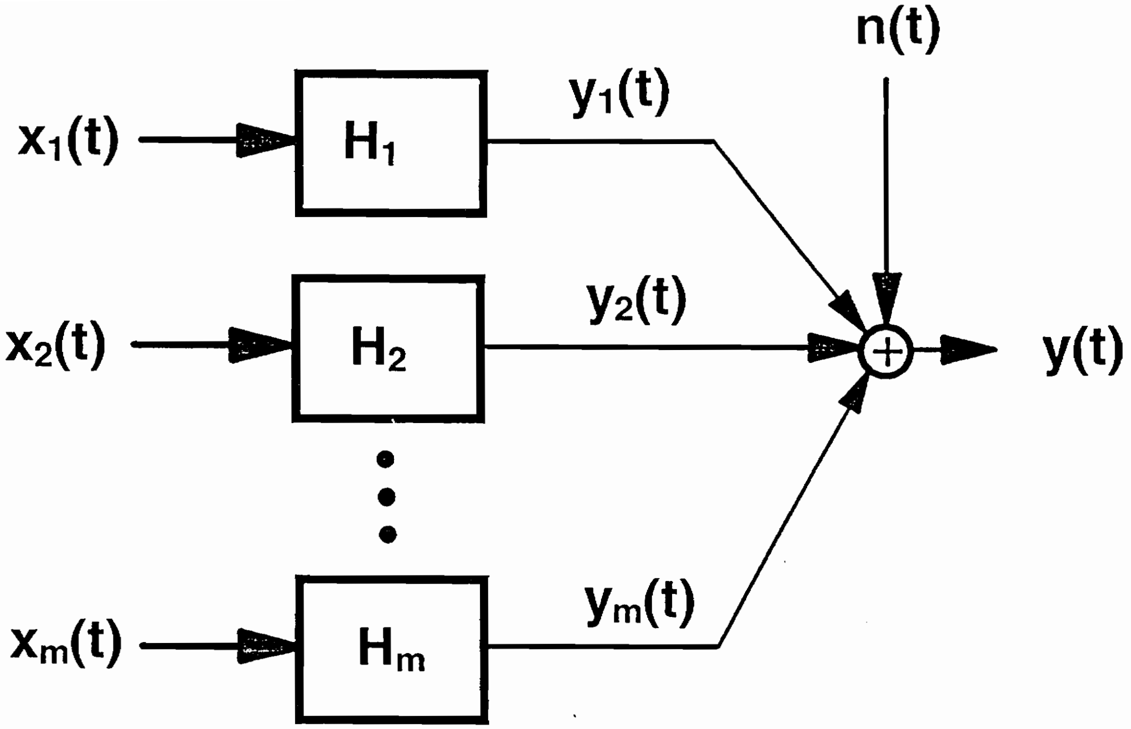

Fig. 2-4: Multiple input - single output system with uncorrelated output noise

$$Y_i(f) = H_i(f)\ X_i(f) \tag{2.47}$$

is the portion of the output caused by input $X_i(f)$. Multiplying Eq. (2.47) by $2/T\ Y^*(f)$ and performing the expectation yields:

$$G_{yy} = \sum_{i=1}^{m}\sum_{j=1}^{m} H_i^*(f)G_{ij}(f)H_j(f) + G_{nn}(f) \tag{2.48}$$

From Eqs. (2.46,2.47) the Fourier transform of the noise term, $N(f)$, and its complex conjugate, $N^*(f)$, are:

$$N(f) = Y(f) - \sum_{i=1}^{m} H_i(f)X_i(f) \tag{2.49}$$

$$N^*(f) = Y^*(f) - \sum_{i=1}^{m} H_i^*(f)X_i^*(f) \tag{2.50}$$

Taking the product of Eqs. (2.49,2.50), multiplying by $2/T$, and performing the expectation yields the autospectrum of the uncorrelated noise as a function of the FRF vector $\{H(f)\}$:

$$\begin{aligned} G_{nn}(f) = G_{yy}(f) - \sum_{i=1}^{m} H_i(f)G_{yi}(f) - \sum_{j=1}^{m} H_j^*(f)G_{jy}(f) + \\ \sum_{i=1}^{m}\sum_{j=1}^{m} H_j^*(f)H_i(f)G_{ji}(f) \end{aligned} \tag{2.51}$$

This relationship can be used to determine the optimal FRF vector $\{H(f)\}$ which minimizes the noise autospectrum $G_{nn}(f)$ in a least-squares sense. The components of the optimal vector are determined by forming the partial derivative of $G_{nn}(f)$ in Eq. (2.51) with respect to $H^*_i(f)$ while holding $H_i(f)$ constant, then setting it equal to zero to obtain:

$$\frac{\partial G_{nn}(f)}{\partial H_i^*(f)} = -\ G_{jy}(f) + \sum_{i=1}^{m} H_i(f) G_{ji}(f) = 0 \tag{2.52}$$

The relationship for the optimal FRF follows directly from Eq. (2.52) is:

$$G_{jy}(f) = \sum_{i=1}^{m} H_i(f) G_{ji}(f) \tag{2.53}$$

which can be recognized as another form of the matrix relationship shown in Eq. (2.42) for a noise-free system.

The linear least-squares approximation of the output using m specified inputs requires the solution of the m x m matrix equation presented in Eq. (2.42) for the FRF vector $\{H(f)\}$. As the number m of inputs increases, the approximation should improve until the "model" autospectrum $\hat{G}_{yy}(f)$ approaches the overall output $G_{yy}(f)$. The relation between the model and overall outputs is:

$$G_{yy}(f) = \hat{G}_{yy}(f) + G_{nn}(f) \tag{2.54}$$

where

$$\hat{G}_{yy}(f) = \sum_{j=1}^{m} \sum_{i=1}^{m} H_j^*(f) H_i(f) G_{ji}(f) \tag{2.55}$$

and $G_{nn}(f)$ is the noise autospectrum. The smaller the $G_{nn}(f)$, the better the model. The magnitude of the noise autospectrum relative to the output $G_{yy}(f)$ is an index to the accuracy of the model.

The multiple coherence function serves the same purpose for multiple-input systems as the ordinary coherence function does for the single input system. The multiple coherence can be defined as:

$$\gamma^2_{x:y}(f) = \frac{\hat{G}_{yy}(f)}{G_{yy}(f)} = \frac{G_{yy}(f) - G_{nn}(f)}{G_{yy}(f)} = 1 - \frac{G_{nn}(f)}{G_{yy}(f)} \qquad \textbf{(2.56)}$$

The multiple coherence is a real-valued function of frequency and is bounded between zero and one. When the multiple coherence function approaches unity, the proposed model can be considered adequate. If the coherence approaches zero, the model can be considered inadequate. Thus, the multiple coherence serves as a quantitative index of the degree of confidence in the multiple input model. The inadequacy of the modeling process can't be determined until after all the analysis work has been completed. When this judgement is made, the modeling process must be repeated using signals from additional candidate sources.

2.4 Solution of the Multiple-Input Problem

It has been shown in section 2.3 that the optimal set of FRF's for a multiple-input system can be found by solving the matrix relationship in Eq. (2.42). This matrix relationship represents a set of linearly independent algebraic equations where the frequency response functions $H_i(f)$ are the unknowns. The equations can be solved directly for the FRF vector $\{H(f)\}$ by a variety of methods. In the very unusual case when the inputs are uncorrelated the off-diagonal terms of the input cross-spectral matrix will be zero. In this case the FRF vector can be solved directly by:

$$H_i(f) = \frac{G_{iy}(f)}{G_{ii}(f)} \qquad i = 1,2,...,m \tag{2.57}$$

which is identical to the H_1 FRF estimator. The system output in this case is the sum of the outputs from m single-input systems as follows:

$$|H_1(f)|^2 G_{11}(f) + |H_2(f)|^2 G_{22}(f) + \bullet\bullet\bullet + |H_m(f)|^2 G_{mm}(f) = G_{yy}(f) \tag{2.58}$$

In practice the inputs are usually correlated requiring a general solution to Eq. (2.42). A common procedure is to solve the matrix equation by Gaussian elimination and back substitution whose intermediate steps has been shown [15] to give special insight into the system being solved. This two-step process first requires matrix decomposition, or Gaussian elimination, which consists of reducing the spectral input matrix into an upper triangular form by row operations. Then the back substitution is performed to obtain the solution of the equations which yields the FRF vector. As an example of this process, consider the following 2 x 2 system:

$$\begin{bmatrix} G_{11} & G_{12} \\ G_{21} & G_{22} \end{bmatrix} \begin{Bmatrix} H_1 \\ H_2 \end{Bmatrix} = \begin{Bmatrix} G_{1y} \\ G_{2y} \end{Bmatrix} \tag{2.59}$$

Multiplying the first row by G_{21}/G_{11} and subtracting it from the second row yields:

$$\begin{bmatrix} G_{11} & G_{12} \\ 0 & G_{22}-G_{21}G_{12}/G_{11} \end{bmatrix} \begin{Bmatrix} H_1 \\ H_2 \end{Bmatrix} = \begin{Bmatrix} G_{1y} \\ G_{2y} - G_{21}G_{1y}/G_{11} \end{Bmatrix} \tag{2.60}$$

The FRF vector can then be determined by back substitution:

$$\begin{aligned} H_2 &= \frac{G_{2y} - G_{21}G_{1y}/G_{11}}{G_{22} - G_{21}G_{12}/G_{11}} \\ H_1 &= \frac{G_{1y} - G_{12}H_2}{G_{11}} \end{aligned} \tag{2.61}$$

This procedure can be applied to a general *m* x *m* system of equations. The general relations for the Gaussian decomposition are:

$$\begin{aligned} G_{iy\cdot r} &= G_{iy\cdot(r-1)} - \frac{G_{ir\cdot(r-1)}G_{ry\cdot(r-1)}}{G_{rr\cdot(r-1)}} \qquad i>r \\ G_{ij\cdot r} &= G_{ij\cdot(r-1)} - \frac{G_{ir\cdot(r-1)}G_{rj\cdot(r-1)}}{G_{rr\cdot(r-1)}} \qquad i,j>r \end{aligned} \tag{2.62}$$

where *r* represents the order of the reduction. The reduction is repeated between successive rows until the input density matrix is reduced to an upper triangular form ready for back substitution.

The back substitution can be performed to determine the estimated FRF vector $\{H(f)\}$ for the multiple input system. The FRF vector and coherence for the conditioned system can be determined from the reduced matrix. The inputs of this conditioned system are linearly uncorrelated and can be treated as separate single-input/single-output systems. This solution is the basis of the partial coherence analysis. It finds the relationship between the output and a conditioned set of inputs and can be subject to uncertainty since the solution is order dependent. The solution is order dependent since in the Gaussian elimination all content of an input that is coherent with the other inputs above it will be removed and, thus, the importance of the contribution of this input to the output may be understated. The solutions of the unconditioned multiple-input and partial coherence models are closely related and can be used together to gain an understanding of the system under analysis.

2.4.1 Partial Coherence Analysis

The conditioning of the system done by Gaussian elimination creates a system of linear independent single-input/single-output systems. The FRF vector between the conditioned input and the output can be determined by using the conditioned input auto and input-output cross spectra:

$$L_{iy} = \frac{G_{iy\bullet(i-1)!}}{G_{ii\bullet(i-1)!}} \qquad i = 1,2,\ldots,m \tag{2.63}$$

where L_{iy} represents the FRF between the conditioned input and the output. The notation

H_{iy} represents the FRF between the original input and the output. The notation *•(i-1)!* indicates the removal of all content in the auto and cross-spectra that is correlated with the previous inputs in the system. The *!* is the standard representation in mathematics for the factorial. The coherence between the conditioned inputs and the output can be calculated as follows:

$$\gamma^2_{iy\bullet(i-1)!} = \frac{|G_{iy\bullet(i-1)!}|^2}{G_{ii\bullet(i-1)!}G_{yy\bullet(i-1)!}} \tag{2.64}$$

which shows the correlation between the conditioned input and the conditioned input-output cross spectrum. If the unconditioned autospectrum of the output G_{yy} is used in Eq. (2.64), the coherence between the conditioned input and the total output can be calculated. The total partial coherence for the output can be calculated from the relationship:

$$\gamma^2_{x:y} = 1 - (1-\gamma^2_{my\bullet(m-1)!})(1-\gamma^2_{(m-1)y\bullet(m-2)!})\ldots(1-\gamma^2_{1y}) \tag{2.65}$$

This total coherence value can be used to determine the adequacy of the model and the accuracy of the FRF estimation.

2.4.2 Multiple FRF Analysis

As mentioned earlier the estimates of the FRF vector between the actual inputs and the output can be determined using a variety of matrix solution methods. The Gaussian elimination and back substitution method yields the conditioned spectra required for the partial coherence analysis during the process of solving for the FRF vector $\{H(f)\}$.

The FRF vector for the actual input can be calculated from the partial coherence frequency response functions using the following relationships:

$$H_{my} = L_{my}$$

$$H_{iy} = L_{iy} - \sum_{j=i+1}^{m} L_{ij} H_{jy} \tag{2.66}$$

where

$$L_{ij} = \frac{G_{ij \cdot (i-1)!}}{G_{ii \cdot (i-1)!}} \tag{2.67}$$

and m is the number of inputs. The multiple coherence will be the same as the total partial coherence given in Eq. (2.65) and can also be calculated from the summation relationship given in Eq. (2.55) when divided by the output autospectrum.

The summation given in Eq. (2.55) provides the tool for analyzing a system. A system with m inputs has an estimated FRF for each of the inputs. The importance of each input can be estimated by setting its associated FRF to zero and performing the summation. The importance of a group of inputs can be determined by setting their FRF values to zero and performing the summation. This sum is then divided by the output autospectrum G_{yy} or the coherent output power $\gamma^2_{x:y} G_{yy}$ to give a correlated output power ratio between the group of inputs and the output. This value can be presented as a ratio or a dB power and is useful for noise reduction analysis. By turning off each input and group of inputs and comparing the correlated powers, the importance of the individual inputs in the output can be estimated. By studying this correlated output power instead of a coherence value prevents the confusion caused by high coherence between an input and the output when the output levels are insignificant.

2.5 Virtual Coherence and Related Methods of Analysis

Several researchers have attempted to develop new methods for the analysis of systems with correlated inputs. One method attempts to separate the correlated inputs of the system into a new set of linearly independent inputs. This analysis technique was developed as virtual coherence by Price and Bernhard [18] and also by Leuridan, Roesens, and Otte [19] and Otte, Sas, and Snoeys [20] as Principal Component Analysis. This is done by performing an orthonormal transformation of the system input spectral density matrix and the input-output cross spectral vector. This singular valued decomposition of the input spectral density matrix into a ranked set of its eigenvalues creates a linearly independent set of inputs. Each of the transformed inputs represent the uncorrelated components in the set of system inputs instead of the order dependent conditioning of the partial coherence analysis. This matrix-based solution provides some useful insight into the system but many of the results are difficult to relate back to the original system since the relationship between the actual system and the transformed system is not clear.

Starting with the system model as defined in Eq. (2.42), a linear transformation is performed to create a set of incoherent "virtual" inputs also called the principal components. The input spectral density matrix G_{xx} can be diagonalized by a linear transformation of the form:

$$G_{xx}^{\prime} = P^{H} G_{xx} P \tag{2.68}$$

where P is a unitary matrix formed by writing the eigenvectors of G_{xx} as columns and G'_{xx} is the diagonal matrix of eigenvalues of G_{xx}. Since this is a Hermitian transformation, Eq. (2-68) can be rewritten as:

$$G_{xx} = P\, G_{xx}^{\prime}\, P^{H} \tag{2.69}$$

and substituting into Eq. (2.42) yields:

$$P^{H} G_{xy} = G_{xx}^{\prime} P^{H} H \tag{2.70}$$

Defining $P^{H}G_{xy}$ as the virtual cross spectral vector G'_{xy} and $P^{H}H$ as the virtual FRF vector H', the equation can be rewritten as:

$$G_{xy}^{\prime} = G_{xx}^{\prime} H^{\prime} \tag{2.71}$$

Since G'_{xx} is diagonal, the virtual FRF can be found directly from:

$$H_{i}^{\prime} = \frac{G_{iy}^{\prime}}{G_{ii}^{\prime}} \qquad i=1,2,\ldots,m \tag{2.72}$$

and the coherence between the virtual input and the output found from:

$$\gamma_{i'y}^{2} = \frac{|G_{iy}^{\prime}|^{2}}{G_{ii}^{\prime} G_{yy}} \tag{2.73}$$

and the total virtual coherence can be determined from the summation:

$$\gamma_{x:y}^{2} = \sum_{i=1}^{m} \frac{|G_{iy}^{\prime}|^{2}}{G_{ii}^{\prime} G_{yy}} \qquad \textbf{(2.74)}$$

The total coherence is bounded between zero and unity and serves the same purpose of indicating the adequacy of the model as in the multiple and partial coherence analysis. The virtual coherence analysis does not assume uncorrelated noise in the output but the level of noise in the system is indicated by the difference between 1.0 and the total virtual coherence.

This type of analysis provides several useful tools for analysis of the system under study. Studying the virtual input power spectrums, or the Number of Incoherent Sources (NIS) [21,22], gives an indication of the number and significance of the independent sources in the actual noise generation system. This solution for the eigenvalues of the input matrix $[G_{xx}]$ where the relative magnitudes of the eigenvalues indicate the importance of each of the independent virtual inputs. Eigenvalues having similar magnitudes can be considered as having almost the same importance in the actual system inputs. This in combination with a basic understanding of the system under analysis can help in identifying the sources in the actual system. The virtual FRF vector and the coherence between the virtual inputs and the output can be used to gain more insight into the system under study. One problem with this analysis is that the connection between the virtual inputs and the actual system inputs is unclear. This makes the use of this method for source or path identification very difficult and subject to much interpretation.

2.6 Bias Errors in Data Acquisition

There are several factors that can introduce errors into the measurements taken with an FFT analyzer. These bias errors will result in an estimate that will be biased low when an FRF is estimated with the H_1 estimator. The bias errors will also reduce the coherence adding to the uncertainty about how much underestimation there is in the FRF. One bias error, the resolution bias error, which is caused by Fourier Transform applied to discrete data can be reduced by proper selection of the data sampling frequency and period of sampling for each record along with the use of ensemble averaging of multiple records. This will also improve the accuracy of the FRF estimate if the system has the characteristics of constant parameter linear system.

2.6.1 Time-Delay Bias Error

Time-delay bias error [2,3,4,7,8] can become important in certain types of experiments. The source of this error is the time delay between an input measurement and the output measurement as shown in Fig. 2-5. This can become important when the input is a force or acceleration measurement on a structure and the output is a microphone positioned in the far field. There will be a delay in the microphone output associated with the time it takes the sound pressure wave to travel from the structure to the

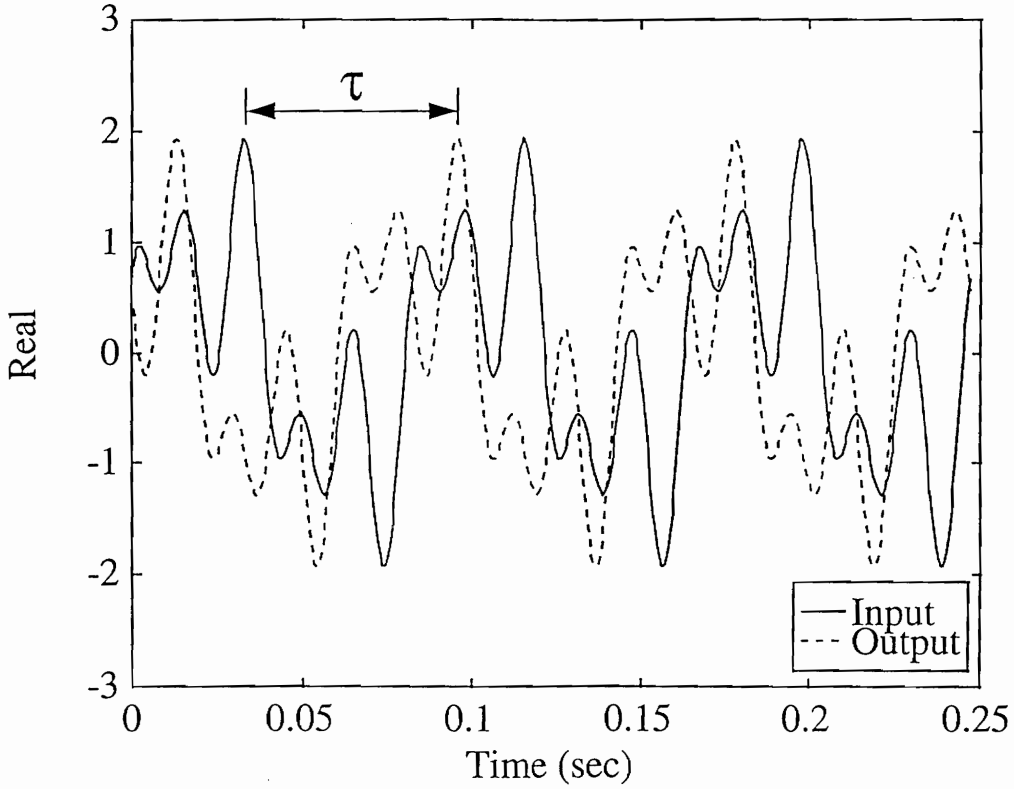

Fig. 2-5: Time delay τ between the input and output signal

microphone. If this delay period is small relative to the data sampling period, the bias effect will be small. Many FFT analyzers trigger all channels for synchronous data acquisition and do not allow a trigger delay for the output measurement. If time delay is significant and the time signal measurements were recorded on tape or a computer disk, it might be possible to realign the output data record to account for the delay.

The effect of the time delay is dependent on the type of sampling window used in acquiring the data. Windows are applied to the data to reduce the uncorrelated content in the input and output and also to reduce FFT process leakage due to signal nonperiodicity. Two of the most common sampling windows are the boxcar and Hanning which are shown in Fig. 2-6. The time-delay bias error for band-limited, Gaussian-white noise with the application of the boxcar window can be estimated using the following relationships:

$$\begin{aligned} \hat{H}_{xy} &= (1 - \frac{\tau}{T})H_{xy} \\ \hat{\gamma}^2_{xy} &= (1 - \frac{\tau}{T})^2\, \gamma^2_{xy} \end{aligned} \qquad (2.75)$$

where τ is the time delay and T is the data sampling period. The time delay bias errors calculation for the Hanning window applied to band-limited, Gaussian-white noise are more complicated and are as follows [15]:

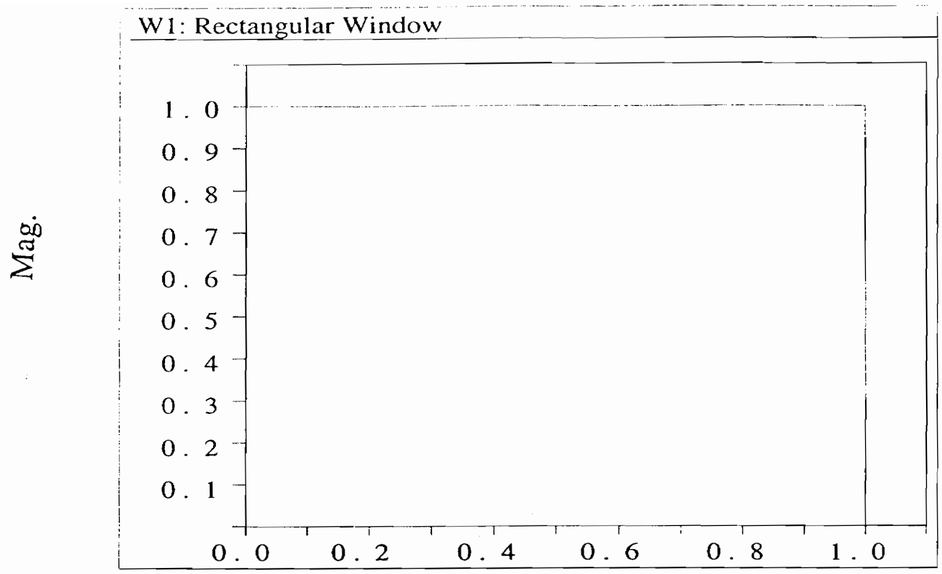

a) Boxcar

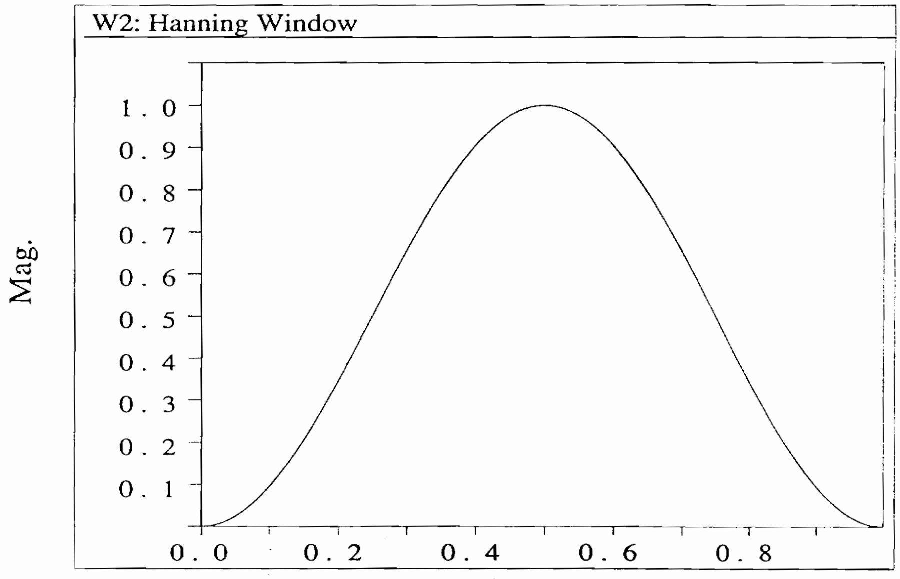

b) Hanning

Fig. 2-6: Common FFT sampling windows: (a) Boxcar, (b) Hanning

$$\hat{H}_{xy} = \frac{8}{3}L(\tau)$$

$$\hat{\gamma}_{xy}^2 = [\frac{8}{3}L(\tau)]^2 \tag{2.76}$$

where

$$\begin{aligned} L(\tau) &= \frac{T-\tau}{4T} - \frac{1}{8\pi}(1+\cos(\frac{2\pi}{T}\tau))(\sin(\frac{2\pi}{T}(T-\tau))) \\ &+ \frac{1}{8\pi}\sin(\frac{2\pi}{T}\tau)(1 - \cos(\frac{2\pi}{T}(T-\tau)w + \frac{1}{8}\cos(\frac{2\pi}{T}\tau)((1-\frac{\tau}{T}) \\ &+ \frac{\sin(\frac{4\pi}{T}(T-\tau))}{4\pi}) + \frac{1}{32\pi}\sin(\frac{2\pi}{T}\tau)(\cos(\frac{4\pi}{T}(T-\tau)) - 1) \end{aligned} \tag{2.77}$$

Plots of the bias error for time delay relative to the sampling period for FRF and coherence estimates for both the boxcar and Hanning windows are shown in Fig. 2-7. These plots show that the significance of the time delay is affected by the selection of the sampling window used in the data acquisition.

Time-delay bias errors can be estimated before an experiment is performed. In many applications it will be insignificant but in others very important. In microphone measurements it can be reduced by moving the microphone closer to the structure, but the microphone may no longer be in the far field where the structure will appear to be a point source. In recorded time measurements on tape or computer disk which have to be processed to get the Fourier transforms, the data for the output can be offset to account for the delay period and significantly reduce the bias error.

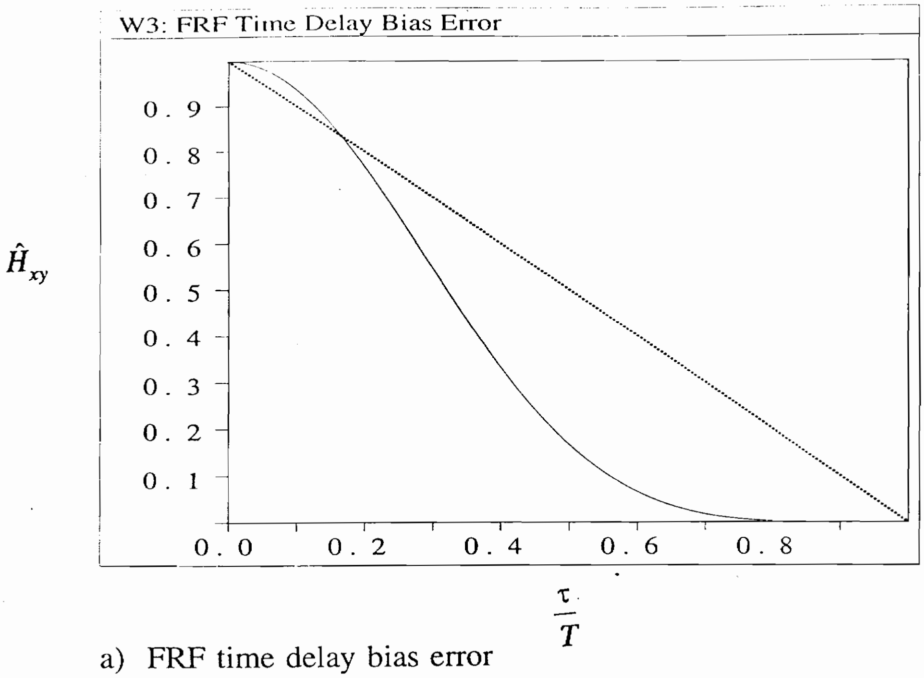

a) FRF time delay bias error

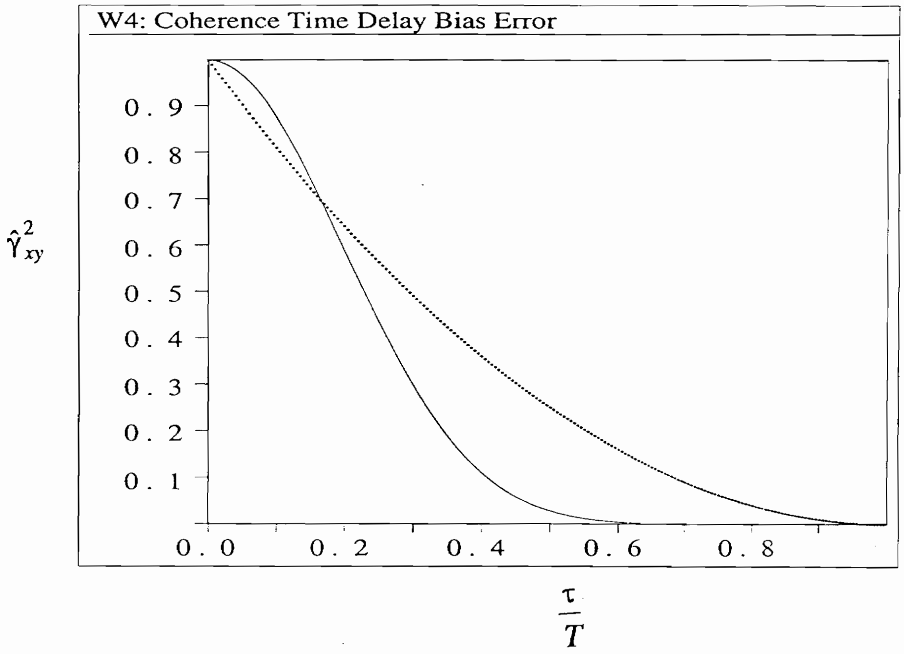

b) Coherence time delay bias error

Fig. 2-7: Time delay bias errors for the Hanning sample window (solid) and the Boxcar sample window (dotted)

2.6.2 Quantization Noise

Another source of error in data acquisition with a FFT analyzer is quantization noise. The input channels of the analyzer have A/D converters which convert the analog voltage signals from the instrumentation to a digital voltage value. The 12-bit converter is commonly used and generally has an operating voltage range of ±1 volt. This yields 4096 steps with a resolution of 0.488 mV between -1 and 1 volt. The input signal must use as much of this voltage range as is practical to reduce the error caused by these discrete steps in the digital conversion. To reduce this problem many manufacturers have an amplification/attenuation circuit before the A/D converter to scale the input to make full use of the converter voltage range. A correction factor scales the digital measurement to account for the amplification/attenuation of the input signal. Averaging of the measurements from several distinct blocks of data will also reduce the effects of quantization noise.

2.6.3 Resolution Bias Error

Another error that can affect the FRF estimation is resolution bias error. The resolution of the measurements in the frequency domain is dependent of the period of time that the input signals were continuously sampled to complete a record. The sampling rate sets the upper limit of frequency range available for analysis. The importance of this error can be explained by using a forced-single-degree-of-freedom system as an example. This example is based on those presented in references [2,7]. The FRF for a second order single-degree-of-freedom system can be represented by

$$H(f) = \frac{1}{1 - (\frac{f}{f_n})^2 + j2\zeta(\frac{f}{f_n})} \qquad (2.78)$$

where ζ is the damping ratio and f_n is the undamped natural frequency. If the input signal is theoretical white noise with autospectral density function $G_{xx}=K$, a constant, and passes through the system, the output autospectrum takes the form:

$$G_{yy} = |H|^2 G_{xx} = \frac{K}{[1 - (\frac{f}{f_n})]^2 + [2\zeta(\frac{f}{f_n})]^2} \qquad (2.79)$$

The peak value of G_{yy} occurs at the resonance frequency $f_r = f_n\sqrt{(1-2\zeta^2)}$. The expected value of the autospectrum is approximately:

$$E[\hat{G}_{yy}] \approx G_{yy} + \frac{B_e^2}{24} G_{yy}^{//} \qquad (2.80)$$

with the bias term approximated by:

$$b[\hat{G}_{yy}] \approx \frac{B_e^2}{24} G_{yy}^{//} \qquad (2.81)$$

For the case where $2\zeta^2 \ll 1$, the second derivative of G_{yy} at the frequency f_r yields:

$$G_{yy}^{//} = (\frac{-8}{B_r^2}) G_{yy} \qquad (2.82)$$

where B_r is the half-power point bandwidth of the resonance peak given by

$$B_r \approx 2\zeta f_r \tag{2.83}$$

Substituting Eq.(2.82) into Eq. (2.81) yields a normalized bias error equation

$$\varepsilon_b[\hat{G}_{yy}] = \frac{b[\hat{G}_{yy}]}{G_{yy}} \approx -\frac{1}{3}\left(\frac{B_e}{B_r}\right)^2 \tag{2.84}$$

This result can be used to approximate the maximum bias error in the autospectral density of data representing the response of lightly damped mechanical and electrical systems. The resolution bandwidth B_e should be less than the system bandwidth B_r to achieve small bias errors.

2.6.4 Other Errors

There are other errors that come from the limitation of discrete sample points acquired at a certain sample rate. This is the result of hardware limitations and the practicality of measuring and processing large amounts of data. These errors can generally be reduced by averaging and can affect the confidence in the FRF and coherence analysis. These errors are explored in great detail in a number of references [2,3,4,7] and are slightly different for single and multiple input systems. These errors can be estimated from the derivations in the references and are generally insignificant with proper experiment setup and averaging of the data.

3.0 COMPRESSOR INSTRUMENTATION

An instrumented test compressor is necessary to perform a noise transmission path and noise source study. Each transducer measurement from the instrumented compressor should be representative of one of the paths or sources. A transducer measurement that reflects more than one path or source will lead to confusion in the analysis and will make path or source determination difficult. Some assumptions about the dynamics of the compressor during operation is required to properly select the instrumentation and determine the proper installation location. The compressor environment also provides some limitations. The instrumentation must be able to operate in a mixture of freon and lubricating oil at a temperature of 200°F (93°C). The instrumentation should be shielded from the AC noise generated by the electric motor. The noise in the measurement signals must to be held to a minimum to increase the certainty in the analysis.

3.1 Hardware Selection

Each of the important noise paths and sources need to be accurately measured. The primary mechanical transmission paths between the motor and crankcase stack and the compressor external shell housing are the three support springs and the shock loop. The springs should be the dominant mechanical path since they support the compressor and are not attached to the external shell at locations that are resistant to motion. The shock loop is a long small tube that attaches to the shell at a location resistant to motion so it is probably not a dominant transmission path. The most dominant acoustic path should be the freon inside the compressor can since the compressor draws the freon for compression out of the shell. It sends the compressed freon out through the shock loop. The lubricating oil in the bottom of the shell is another possible transmission path but its dynamic behavior in the compressor is an unknown. Since there is a small amount of oil at the bottom of the can for compressor lubrication, the oil path should be less significant than the freon path.

The transducers, their mounting locations, and the number of data channels required for each transducer are listed in Table 3-1. The model and serial numbers of the installed transducers are listed in Appendix A. The locations of the transducers inside the compressor are shown in Figs. 3-1 and 3-2. Modifications to the compressor were held to a minimum to prevent changes in the compressor dynamics. The triaxial force gage installation caused some substantial shell response changes which will be discussed in detail in Section 3.3. The instrumented compressor did meet its capacity rating but was approximately 3% less efficient than the standard production compressor model.

3.1.1 Mechanical Path Transducer Selection

The three support springs should be the dominant mechanical transmission path with the shock loop playing a minor role. It is important to measure the forces between

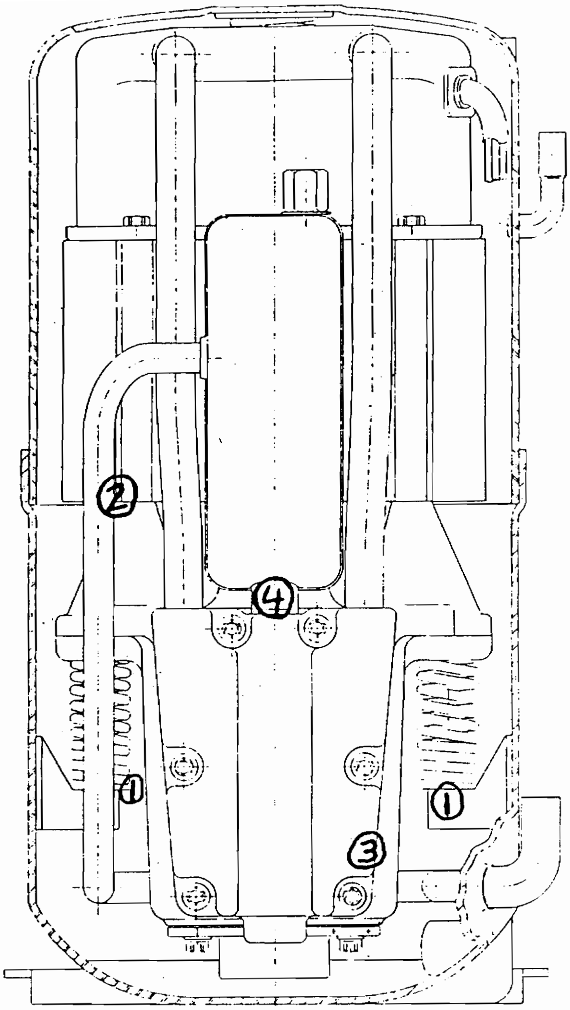

① Lower support spring triaxial force (2)

② Shock loop accelerometer

③ Suction pressure

④ Discharge muffler pressure

Fig. 3-1: Instrumentation installation location - end view (adapted from Bristol Compressors, Inc., Production Drawing)

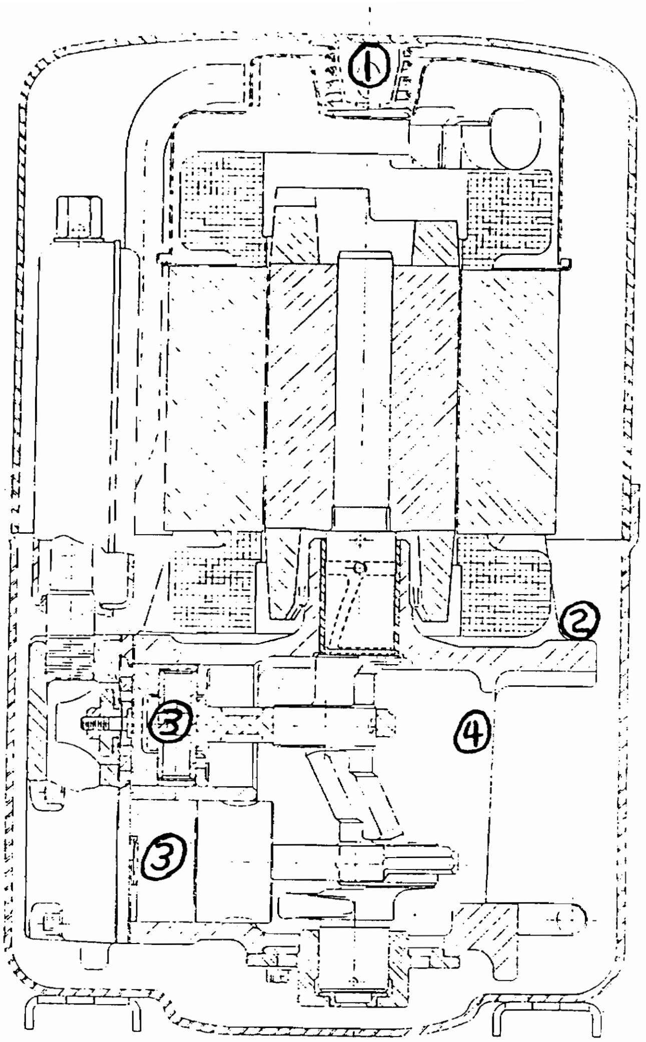

① Top support spring triaxial force

② Housing pressure

③ Cylinder pressure (2)

④ Crankshaft tach proximity probe

Fig. 3-2: Instrumentation installation location - side view (adapted from Bristol Compressors, Inc., Production Drawing)

Table 3-1: Compressor internal instrumentation

Location	Type	Channels
Top spring	Triaxial force	3
Front spring	Triaxial force	3
Back spring	Triaxial force	3
Shock Loop	Accelerometer	1
Housing pressure	Pressure	1
Suction head	Pressure	1
Discharge muffler	Pressure	1
Top cylinder	Pressure	1
Bottom cylinder	Pressure	1
Crankshaft tachometer	Proximity probe	1

the springs and the compressor housing. This is important to the transmission path determination analysis and these forces can be recorded and used to drive the finite element model of the compressor. The primary candidates for this application are piezoelectric force gages, strain gages, accelerometers, and linear velocity transducers. Each type of transducer has limitations in this compressor application.

The best candidate is the piezoelectric force gage. A regular axial force ring that is internally preloaded would be the easiest to install with little compressor modification. The main disadvantage of this type of force ring is its ability to measure the force along only one axis. The compressor support springs will be transmitting forces along all three axes with the vertical force that would be measured by a regular force ring potentially having the smallest amplitude. To accurately reflect the forcing functions on the compressor shell the lateral forces exerted by the support springs must be measured. Kistler Instrument Corp. manufactures a line of force transducers that measure in three axes. This transducer was chosen for the compressor installation which is covered in detail in Section 3.2. This transducer normally requires a 5600 lbf (25 kN) standard preload. It can be used as an axial force ring measuring only compression when used without a preload. The preload is required to generate shear forces across the quartz wafers that are sensitive to the two lateral forces. The transducers are calibrated by Kistler using their standard mounting hardware. The compressor installation requires custom mounting hardware to provide the preload and to mimic the existing compressor hardware. This will require an in-situ calibration since the standard mounting hardware is not used. It is difficult to install this transducer without changing the compressor dynamics because of changes in the effective local mass and stiffness in the spring mounts.

Strain gages could be installed to measure the strain generated in the spring retainers by the forces exerted by the springs. The relationship between the measured strains and the three axial forces would need to be determined, possibly from finite element modeling or in-situ calibration. Another problem is the AC field generated by the compressor motor will require the use of carrier amplifiers to keep the strain gage outputs from being dominated by the AC motor harmonics. Carrier amplifiers send a high frequency carrier signal across the strain gage. The changes in strain amplitude modulate this carrier signal which when demodulated yields the strain dynamics with minimal AC motor noise distortion. Care must be taken in using carrier amplifiers because the high carrier frequency makes it possible to accidently overload and destroy the strain gage. Other problems with strain gages are the frequency response and resolution limitations relative to the piezoelectric transducers. Moreover, few carrier signal conditioning systems for strain gages are marketed in the United States at this time.

Accelerometers mounted in a triaxial configuration are another possibility in this application. This triax could be mounted on the spring retainers but the accelerations will not directly represent the forces passing though the springs. This problem could be alleviated with triaxes mounted at each end of the springs to determine the relative displacement. The required 6 channels per spring would exhaust the 16 channels available in our analyzer and would require some post processing to back out the forces transmitted across the spring. This setup requires an assumption that the spring behaves as a pure spring. This assumption makes accounting for the forces from surging springs nearly impossible. Spring surge occurs when the spring is driven at or near one of its internal resonance frequencies. Traveling waves develop within the spring and the inertial forces from this surge motion will not be accounted for in the acceleration measurements. The first spring surge frequencies occur at about 370 Hz and are well within the frequency range of interest for the force evaluation.

The remaining candidate is the linear velocity transducer (LVT). This electromagnetic device has several drawbacks in this application. The size required to measure the velocities across the support springs will have a limited frequency response. The estimation of the forces exerted by the spring from the velocity measurement will be difficult. They may also be very susceptible to the AC noise radiated by the compressor motor and will also be oblivious to spring surge. Another difficulty is creating an installation that will measure the triaxial velocities without significant compressor modification and very careful alignment.

Instrumenting the shock loop to estimate the forces it exerts on the shell without substantial modification to the compressor is difficult. Strain gages will require modeling to relate the strains to the triaxial forces and will require carrier amplifiers. An accelerometer was installed on the shock loop near the muffler. This should not give a good representation of the forces exerted on the shell but it will give a measurement of the motion of the upper section of the shock loop during operation.

3.1.2 Acoustic Path and Potential Source Transducer Selection

A high sensitivity microphone was mounted on top of the crankcase on the side opposite the muffler and valve head. This should give a good indication of the pressure dynamics of the freon acoustic path inside the compressor shell. Pressure transducers were also installed in the suction head and in the discharge tube between the valve head and the muffler. These two transducers will measure the dynamics of the suction and discharge which may be potential sources of noise. The suction measurement should be important since the compressor draws the freon for compression from the external shell.

Pressure transducers were installed in each cylinder to measure the dynamics of the pressure cycle. Valve flutter during operation will potentially show up in the cylinder pressure dynamics. The compression cycle is a source of some of the noise but will not accurately reflect the kinematics of the pistons, connecting rods, and crankshaft. This makes a detailed source determination difficult. Kinematic modeling of the compressor is probably required to determine the reaction forces generated by the motion of the mechanical parts during compressor operation. This type of modeling is required to determine the internal sources of the mechanical excitations in the compressor.

A magnetic proximity probe was installed to provide a trigger for synchronous data acquisition. This is critical for time averaging of the transducer measurements to show the average compressor dynamics during the compression cycle. For the time averaging to give accurate results, each data record must be sampled at the same point in the compression cycle. This trigger can also be used to ensure that each time block used to generate the frequency-domain data starts at the same point in the compression cycle. This is important because the combination of the FFT analyzer standard sampling frequencies and time block lengths will not correspond to a exact multiple of the compressor cycle period. Triggering at the same point in the cycle ensures the same portion of the incomplete cycle is used in the frequency-domain spectral estimates. If the analyzer is allowed to trigger whenever it is ready to acquire the next time block, different portions of the incomplete cycle will be used in the frequency-domain spectral estimates. This incomplete cycle variability will lead to more variability in the autospectra and cross-specta estimates. Using the trigger for the time blocks removes one potential source of variability in the frequency-domain data.

The selection and installation of the pressure transducers, the accelerometer, and magnetic proximity probe was handled by David Gilliam at Bristol Compressors. The instrumented compressor was assembled and the compressor instrumentation was checked for proper operation at Bristol Compressors before it was sent to the Virginia Polytechnic Institute and State University lab for analysis.

3.2 Mounting, Installation, and Calibration of Triaxial Force Gages

The Kistler 9251A triaxial force gage was chosen to measure the interaction forces between the compressor support springs and the shell. These forces, if measured, can be correlated to the acoustic output of the compressor to determine the importance of the individual paths and can also be used as the phased dynamic forces to drive the finite element model of the compressor. The force gage shown in Fig. 3-3 is 0.945 in (24 mm) square with a height of 0.394 in (10 mm). It is a charge-mode piezoelectric transducer which can measure both axial and two lateral forces passing through the support springs. The force gage has a force range of 2200 lbf (9800 N) in compression and 1100 lbf (4900 N) in shear with the standard 5600 lbf (25,000 N) preload. It can withstand the freon environment and the AC field produced by the motor during compressor operation. The main disadvantages of this force gage are the required

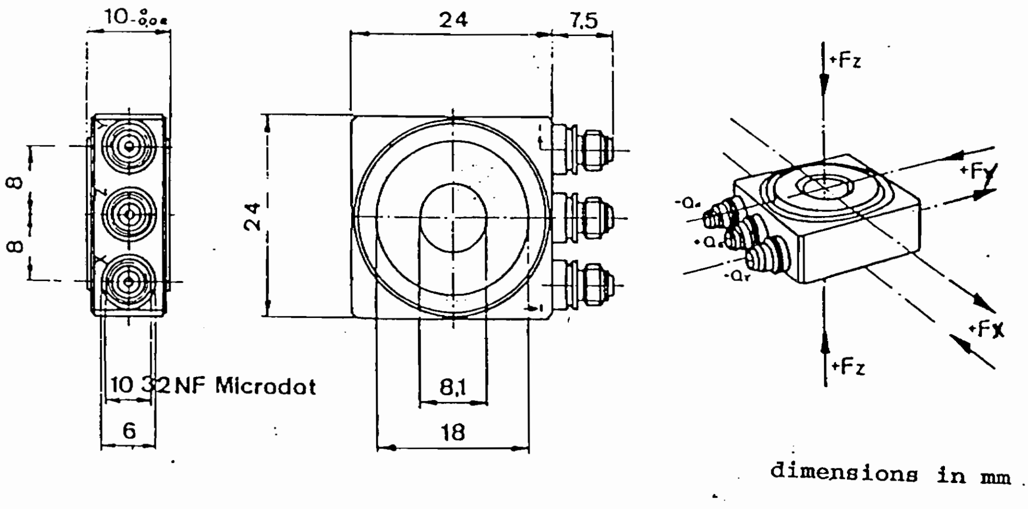

Fig. 3-3: Kistler 9251A triaxial force gage (after [27])

preload, the possibility of large moments at start-up cracking the quartz crystals, the lack of a moment measuring capability, and the modifications in the compressor shell necessary for installation.

3.2.1 Installation

A typical compressor has two identical support springs that rest on brackets spot welded to the side of the shell (see Fig. 3-4) and a centering spring at the top that rests against a mount which is spot welded to the top of the shell (see Fig. 3-5). It was a challenge to devise the mounting assemblies necessary for the force gages without significantly stiffening or mass loading the shell. Kistler approved a 3750 lbf (16,700 N) preload for our application in order to measure the lateral forces and improve its tolerance to the high moments at compressor start-up. The mating surfaces must be as smooth and plane as practical. A small boss was machined on each of these surfaces to fit within the recesses at the edge of the mounting hole in the force gage (see Fig. 3-3, Isometric view only) to aid in alignment during installation and to ensure the transmission of the lateral forces to the transducer. No modification of the force gages were required for this installation. Stops were also installed to limit the compressor motion at start-up to limit the start-up moments that will be seen by the force gages.

The standard lower spring support bracket is shown in Fig. 3-4. The spring retaining post was removed and the assembly shown in Fig. 3-6 was installed in its place. The threaded force gage mount fits inside of the bracket in place of the spring

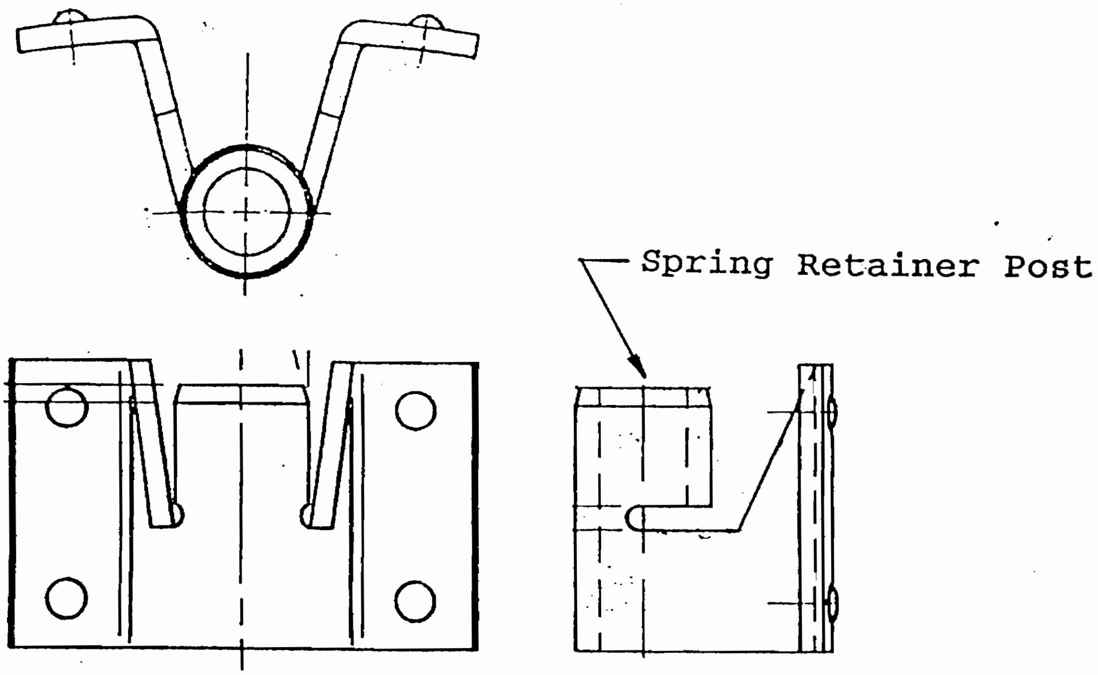

Fig. 3-4: Standard side spring mounting bracket (after [28])

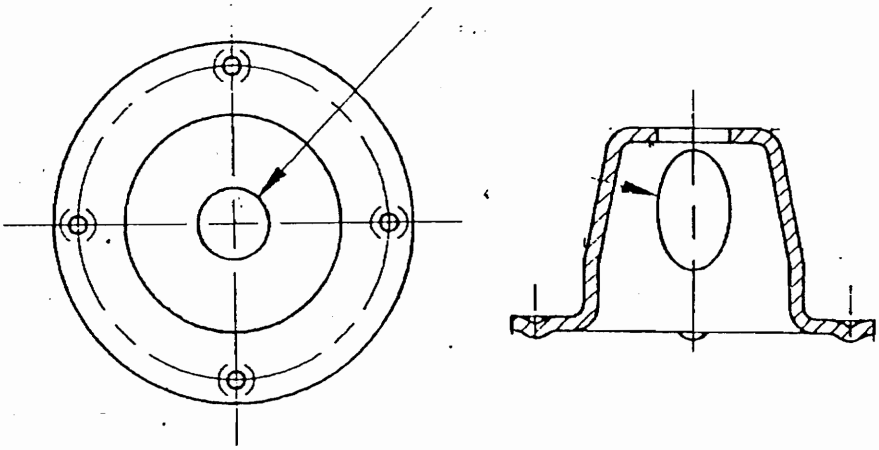

Fig. 3-5: Standard top spring retainer (after [29])

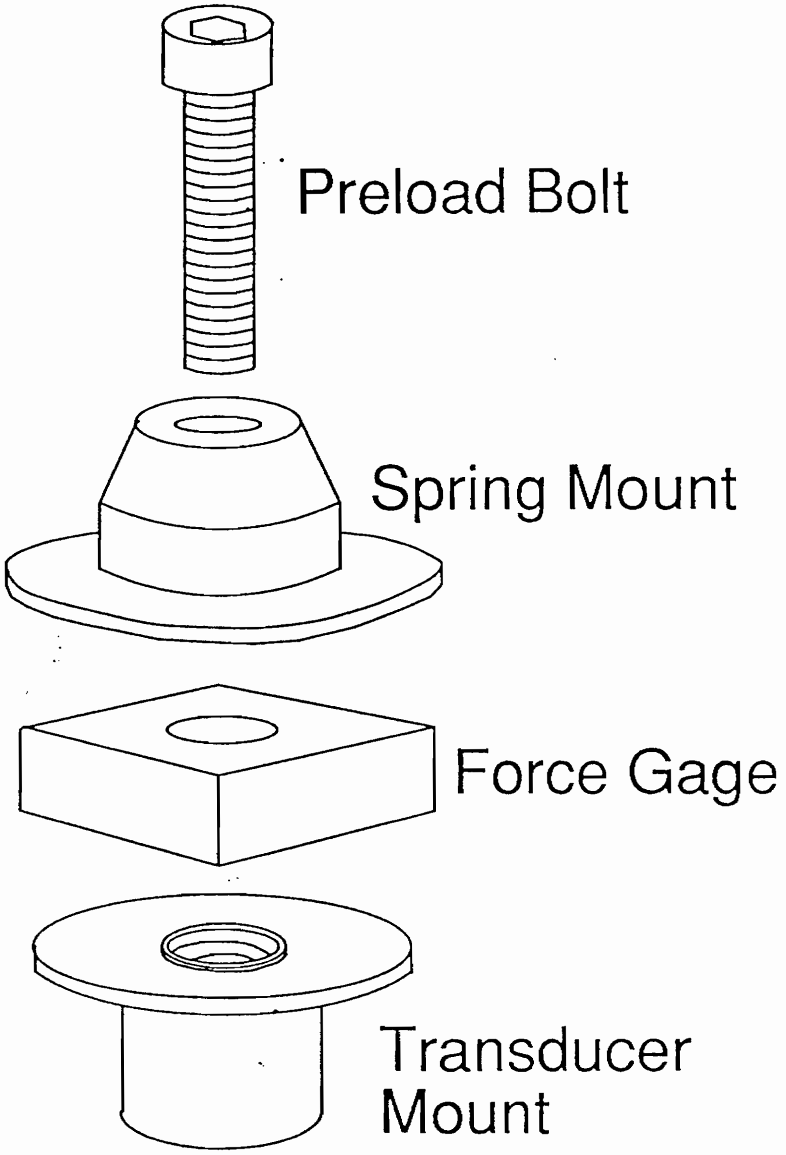

Fig. 3-6: Side spring force gage assembly (after [30])

retainer post and was silver soldered to the end of the bracket. The disk at the top of this mount provides the required mating surface for the force gage and rests on top of the modified bracket. The spring mount that fits on top of the transducer mimics the old post. It has straight sides up to the height of the original post minus the force gage height and platform thicknesses. It then slopes back to the center at approximately 10 degrees to avoid contact with the spring. The extra height ensures that the spring cannot hop off the mount. A 0.25 in (6.4 mm) Allen head bolt fits through the spring mount and force gage with the transducer mount serving as the nut. In order to keep the compressor in the same position relative to the bracket, three of the four dead coils at the base of the stock springs were removed to account for the added height from the force gage installation.

The top spring mount was more difficult to design. The standard top spring retainer is shown in Fig. 3-5. The assembly that was installed in its place is shown in Fig. 3-7. A 0.25 in (6.4 mm) thick threaded disk was silver soldered to the top of the shell to provide a solid base for the force gage. The spring mount was designed to be similar to the original spring retainer with enough clearance in the center to allow a 5/16 in (7.9 mm) hex-head bolt to be installed. The four holes in the side of the spring mount help reduce the weight. The top spring has no dead coils so the spring well in the motor cap was deepened to allow for the extra height of the force gage installation.

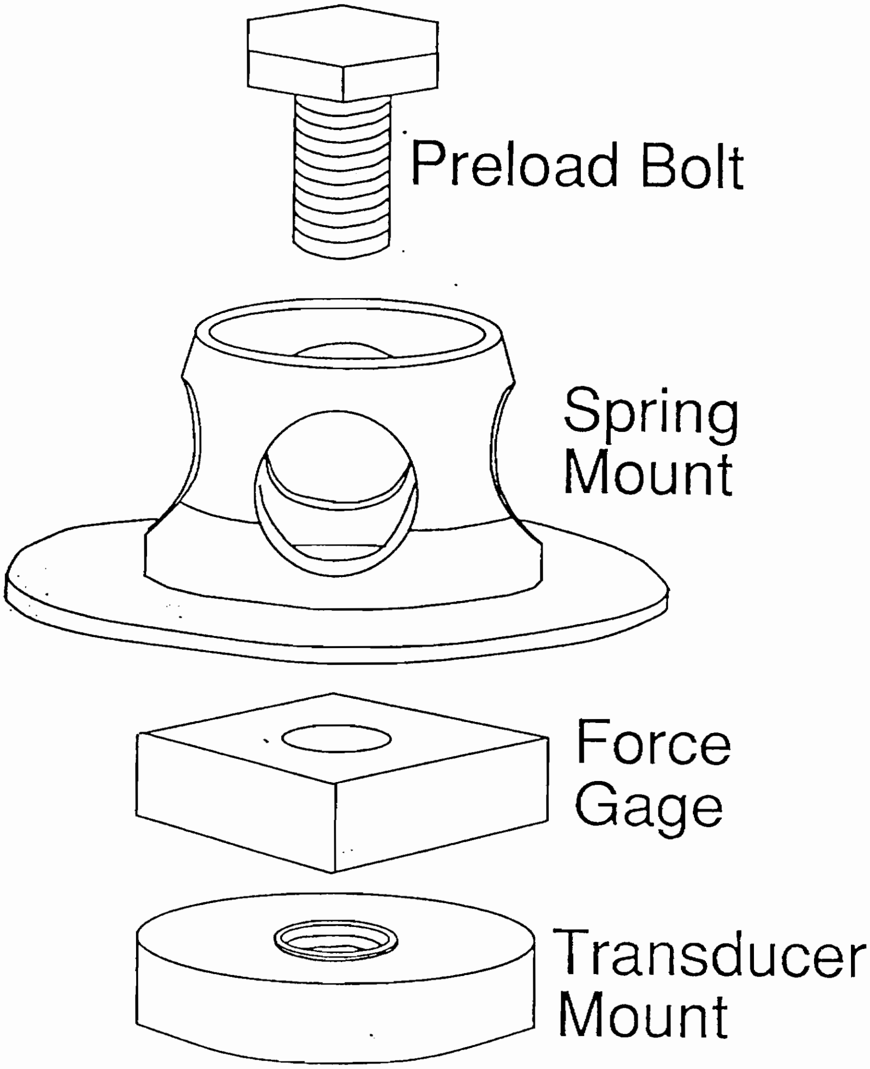

Fig. 3-7: Top spring force gage assembly (after [30])

3.2.2 Static Calibration

The unloaded sensitivity calibrations for the transducers were used when applying the preload. Once the transducers are preloaded these sensitivity values are no longer valid. Since the standard Kistler preload and hardware were not used in this application, static in-situ calibrations needed to be performed as described by Soom and Kubler [31].

The static calibration was performed using several weights ranging from 1 lbf (4.448 N) to 8.66 lbf (38.52 N). Limited clearance inside the shell prevented some weights from being used in all of the calibrations. The weights were either set on or hung from the force gage along each of its primary axes. The charge amplifier was set to the long-time constant to allow time to read the voltage output from a digital voltmeter before significant decay. The charge amplifier was reset and if there was not any significant drift in the voltage readings, the force gage was unloaded and the steady-state voltage value was recorded. A number of values were taken with each weight and averaged. These averaged values were used in the linear regression fit of the charge sensitivity. The lateral sensitivity values were averaged to find a single sensitivity value for both of these axes. A typical sensitivity calibration for all three axes is shown in Fig. 3-8.

3.2.3 Dynamic Calibration

An impact test was then performed to verify the force gage dynamic calibration.

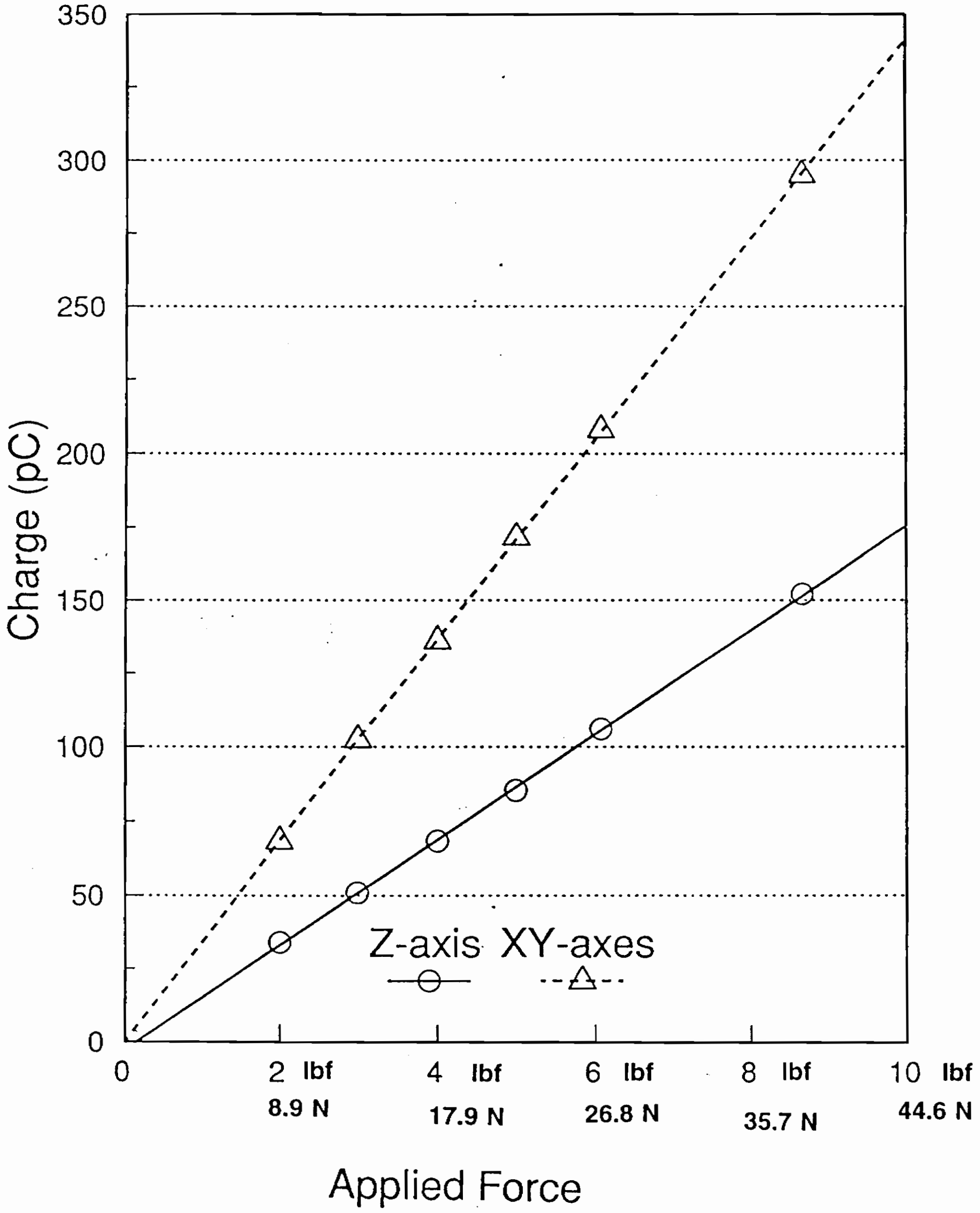

Fig. 3-8: Static calibration of back spring triaxial force gage (S/N 50090)

This type of dynamic test requires an instrumented modal hammer which has a built-in force gage and a multi-channel fast Fourier transform (FFT) analyzer. For this type of calibration the spring mount was impacted with a modal hammer along a primary axis of the force gage. The FFT analyzer is set to trigger on the impulse from the hammer and records the time responses of both the hammer and triaxial force gage. These time responses are Fourier transformed into the frequency domain. The individual channel spectra and cross spectra between the channels are averaged over several impacts to improve accuracy. The cross-spectral and auto-spectral energy densities are used to determine the frequency response function (FRF) between the hammer force and the force gage output. This FRF is the dynamic calibration of the transducer. The time responses from an impact test are shown in Fig. 3-9 and the averaged energy spectrums are shown in Fig. 3-10. The stiffness of the tip on the hammer and the compliance of the structure limit the frequency range of an impact test. The impulse in the time response narrows as the combined stiffness of the tip and structure increases. As the impulse narrows, the frequency range required to represent it increases. Quality forces are usually taken as the frequency range of the data up to the -10 dB point in the force energy density. The limit of this quality range for the energy densities shown in Fig. 3-10 is approximately 2200 Hz. The coherence between the input and output is also used as a reference to indicate FRF quality and possible bias error in the frequency response function.

The frequency response function between the hammer impact on the spring mount and the force gage response was expected to be smooth with a rise in sensitivity as the

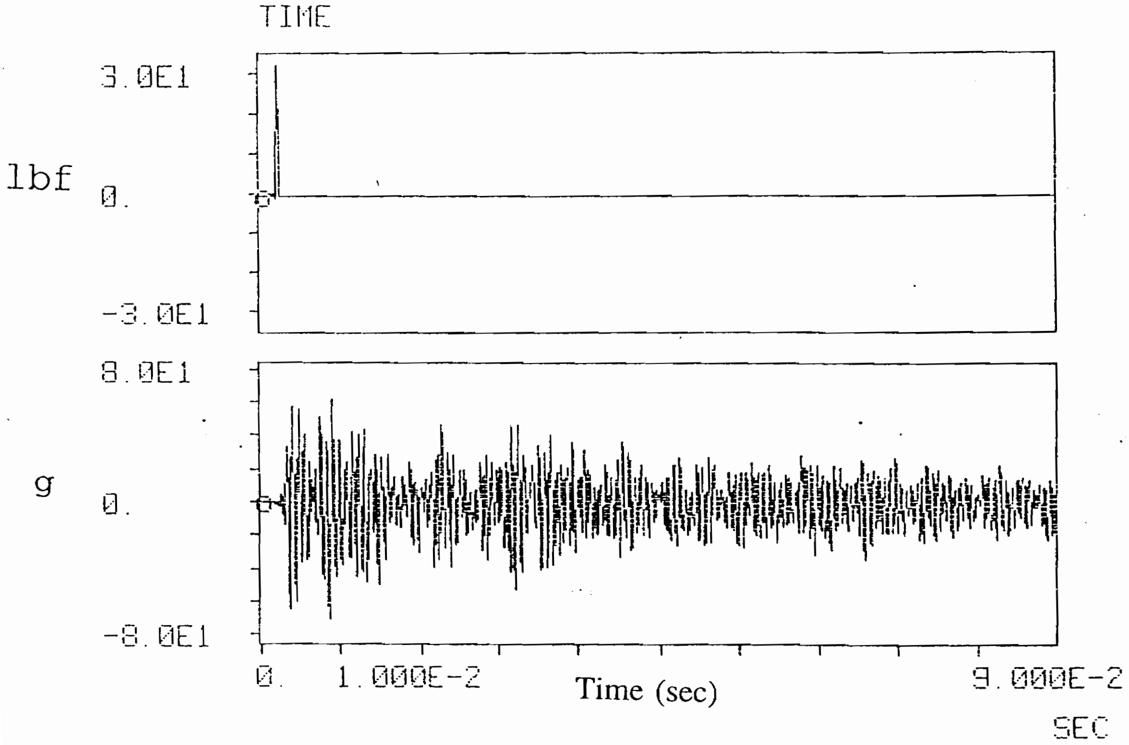

Fig. 3-9: Time responses from an impact test

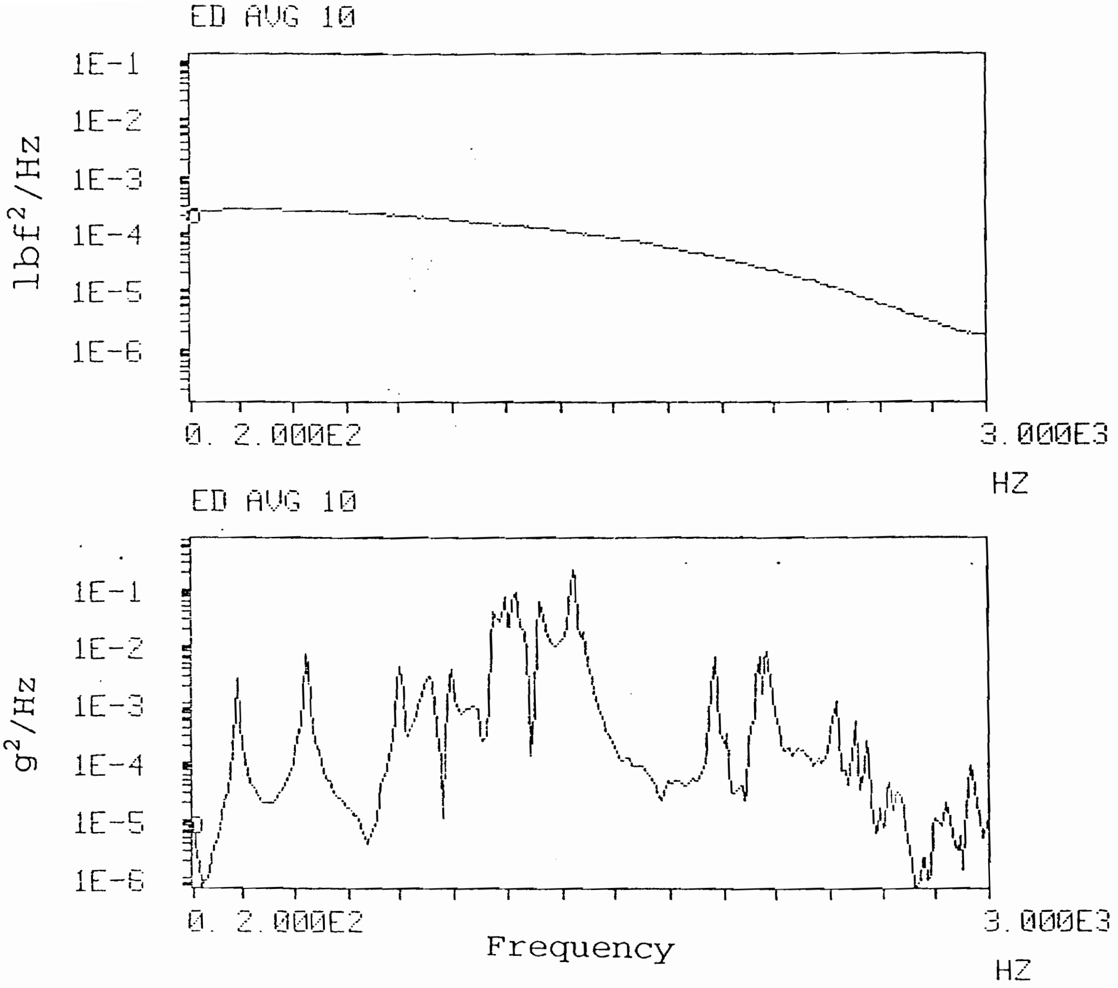

Fig. 3-10: Energy spectrums from an impact test

transducer assembly reached its first resonance frequency. The actual response, as shown in Fig. 3-11, turned out to contain a number of apparent resonances beginning at approximately 800 Hz. The time response values showed an impulse for the modal hammer and the impulse followed by a ringing from the triaxial force gage indicative of its functioning as an accelerometer. Several impact tests were then performed attempting to correlate the force gage response to the accelerations of the spring mount or the support bracket. The frequency response between the force gage and an accelerometer mounted perpendicular to the shell on the end of the lower bracket under the force gage is shown in Fig. 3-12. This indicated that the distortion in the direct impact calibration was due to the effects of the force gage assembly being mounted on a light dynamic structure and, in turn, it acting as an accelerometer. The hammer impact was on the outside of the shell at a spot of high curvature which has a lower compliance and should yield a wider frequency range of the impact. This was the only axis and mount that exhibited a fairly clean correlation between the force gage and accelerometer. This means that the spring adapter mass was acting like an inertial mass on top of a force gage. This combination made an accelerometer. The remaining comparisons for acceleration to force for the other directions had many peaks in their frequency response functions. This did not conclusively attribute the peaky FRF from the direct impact calibration shown in Fig. 3-11 to the dynamic forces from the relative motion between the spring mount and the support bracket.

Another test was devised to verify that the transducer assembly was acting like an

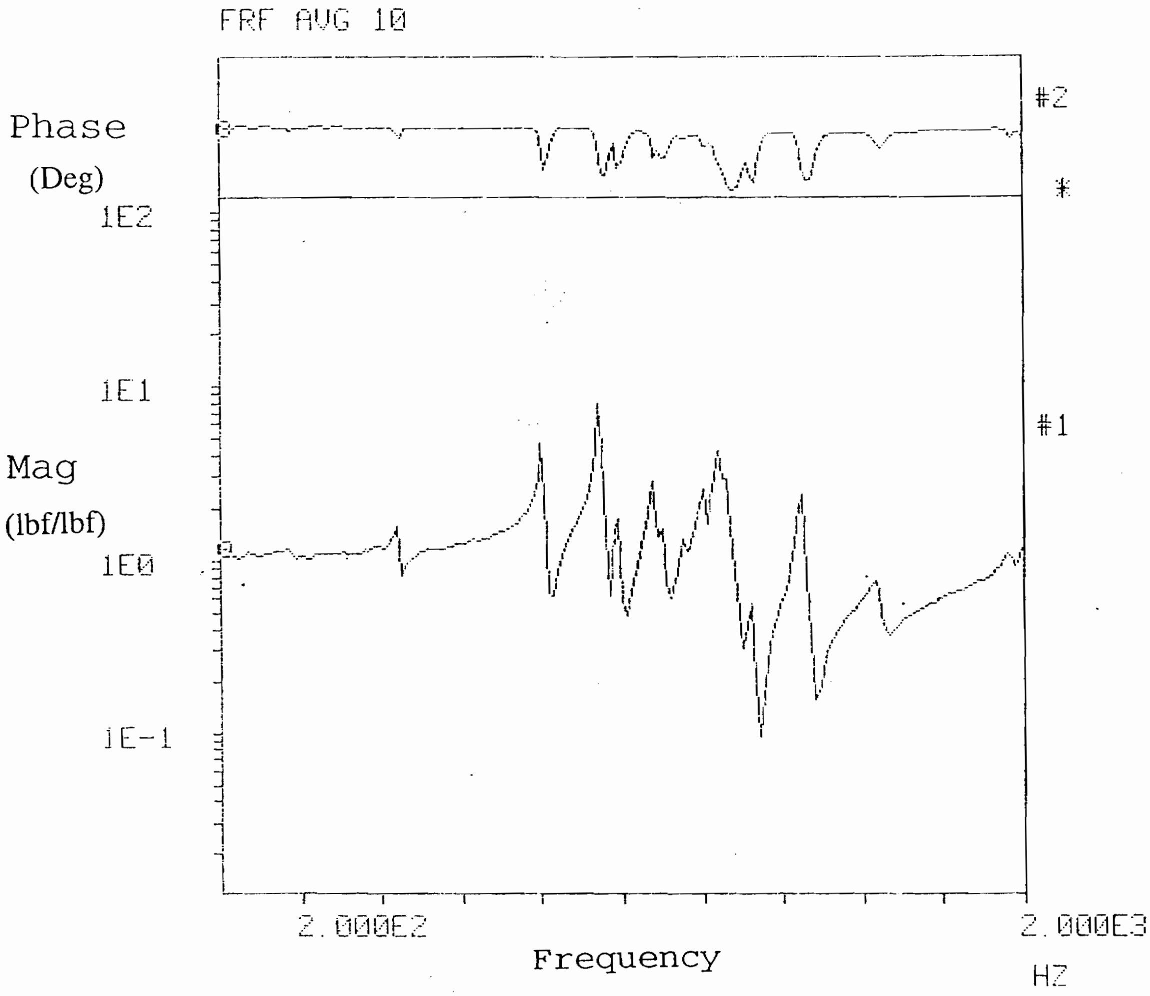

Fig. 3-11: Side spring mount FRF from direct impact

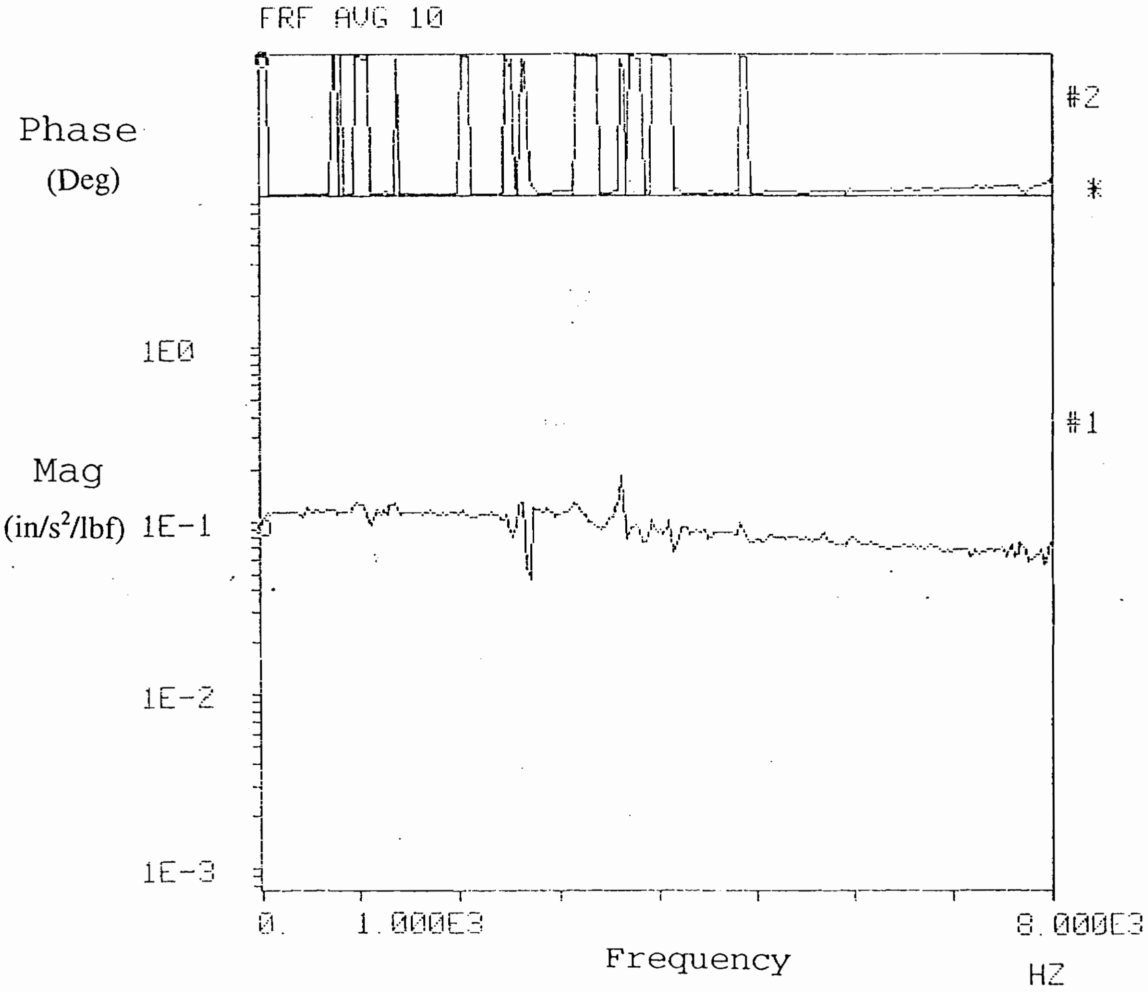

Fig. 3-12: Force gage to accelerometer FRF

accelerometer on a light dynamic structure. A solid steel cylinder with a diameter of 4.0 in (101.6 mm) and a height of 7.5 in (190.5 mm) was machined and threaded to accept the 0.25 in (6.4 mm) bolt used in the side compression mounting spring force gage assemblies. This cylinder weighed approximately 25 lb (11.34 kg) and should serve as an inertial base for the test. This cylinder was estimated to have its first transverse resonance above 12 kHz which is above our frequency range of interest. Axial modes were significantly above this frequency. One of the side force gages and its spring mount were removed and fastened to this cylinder. A direct impact test on the spring mount produced the smooth FRF shown in Fig. 3-13 which was originally expected. This helped validate the hypothesis that the distortion in the frequency response from a direct impact of the force gage was a result of the shell and bracket response showing up as inertial forces in the triaxial force gage. The force gage was then removed and reinstalled on the support spring bracket and recalibrated statically.

It should be apparent from the above work that the triaxial force gage installation has an acceleration sensitivity. Using the experiments with the accelerometer to force gage comparison when mounted on the flexible shell, one can determine the various force gage sensitivities to acceleration. The inertial mass above the side spring mount force gage is approximately 0.10 lbm (44 gm) which agrees with the FRF in Fig. 3-12. This means the force gage has an acceleration sensitivity along this axis of 0.1 lbf/g (0.44 N/g). The acceleration sensitivity for the other axes should be proportional to the calibration force sensitivity with the peaks in the other force gage to accelerometer

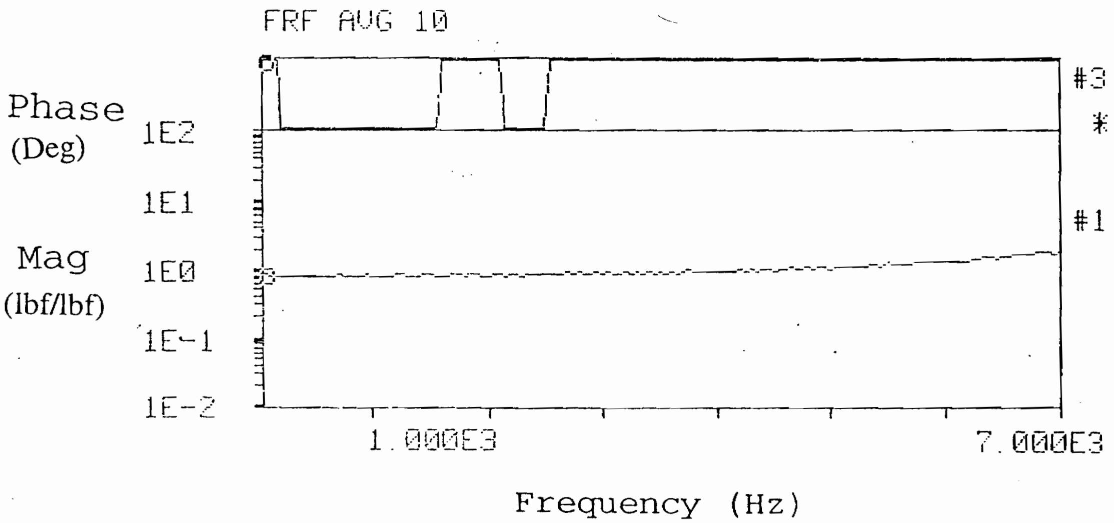

Fig. 3-13: Direct impact FRF from side spring force gage assembly mounted on the cylinder

frequency response functions the result of angular acceleration.

3.3 Compressor Assembly Response Changes Caused by the Instrumentation

The installation of the triaxial force gages did result in several compressor assembly response changes. Impact testing was performed on both a regular compressor and the instrumented compressor to find changes in the shell responses. An instrumented modal hammer was used to excite the compressor shell on the welded band where the two halves of the shell overlap. The location of the impact is shown in Fig. 3-14. Accelerometers were used to measure the shell response at the top of the external shell and three locations on the side as shown in Fig. 3-14. There were some substantial response changes at selected frequencies that may help explain why the instrumented compressor is quieter than the regular model.

The most substantial reduction in the compressor assembly response from the instrumentation occurred in the region between 900 and 1000 Hz. The overlay plot of the top response of both compressors shown in Fig. 3-15 show a 40 dB reduction in the mobility in that frequency range. The response at side location #1 shown in Fig. 3-16 shows approximately 20 dB reduction in the mobility but the response at location #2 shown in Fig. 3-17 shows little change in the range of 1000 Hz. The shell response of both compressors at location #2 between 900 and 1000 Hz is very low which may explain

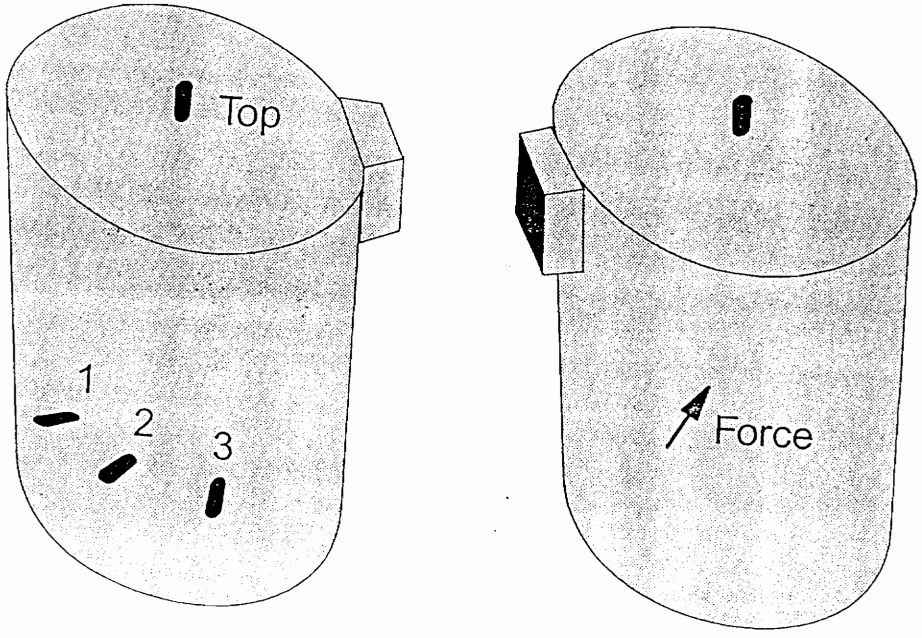

Fig. 3-14: Impact testing hammer and accelerometer locations used on both the instrumented and regular production compressor

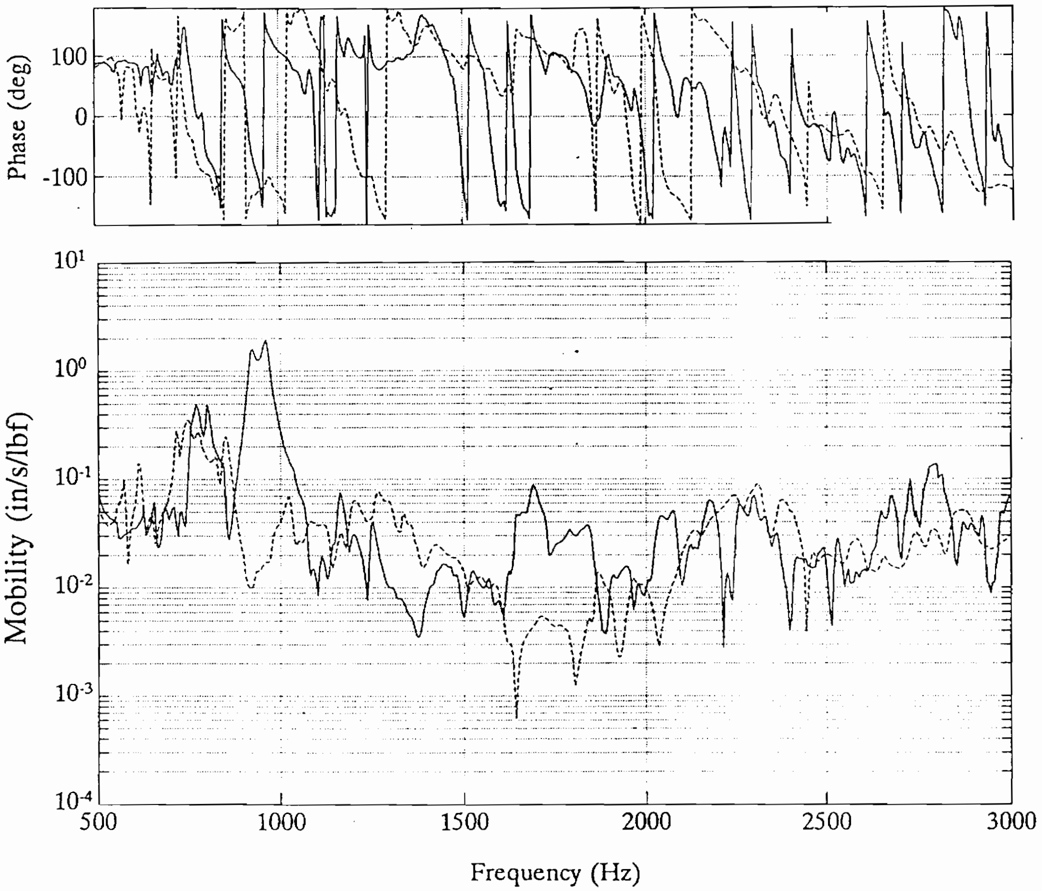

Fig. 3-15: Overlay of the compressor top mobility
———— Regular, ----- Instrumented

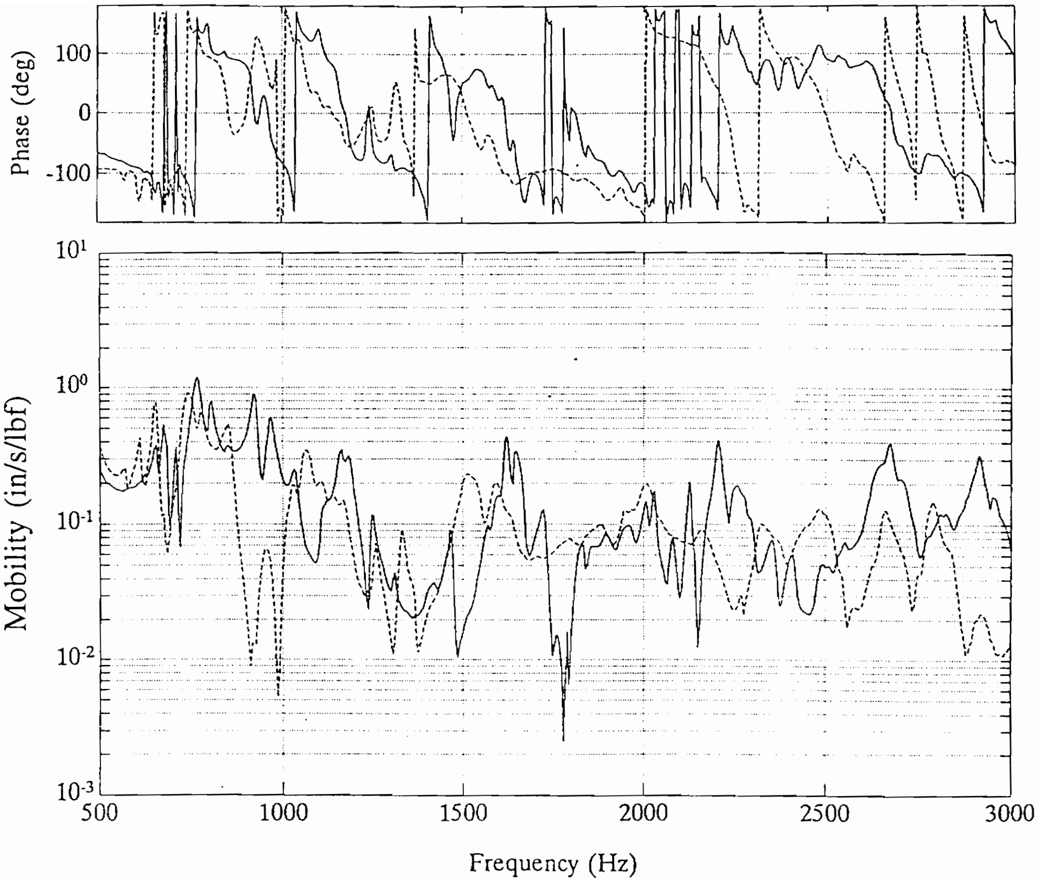

Fig. 3-16: Overlay of the mobility at side location #1
———— Regular, ----- Instrumented

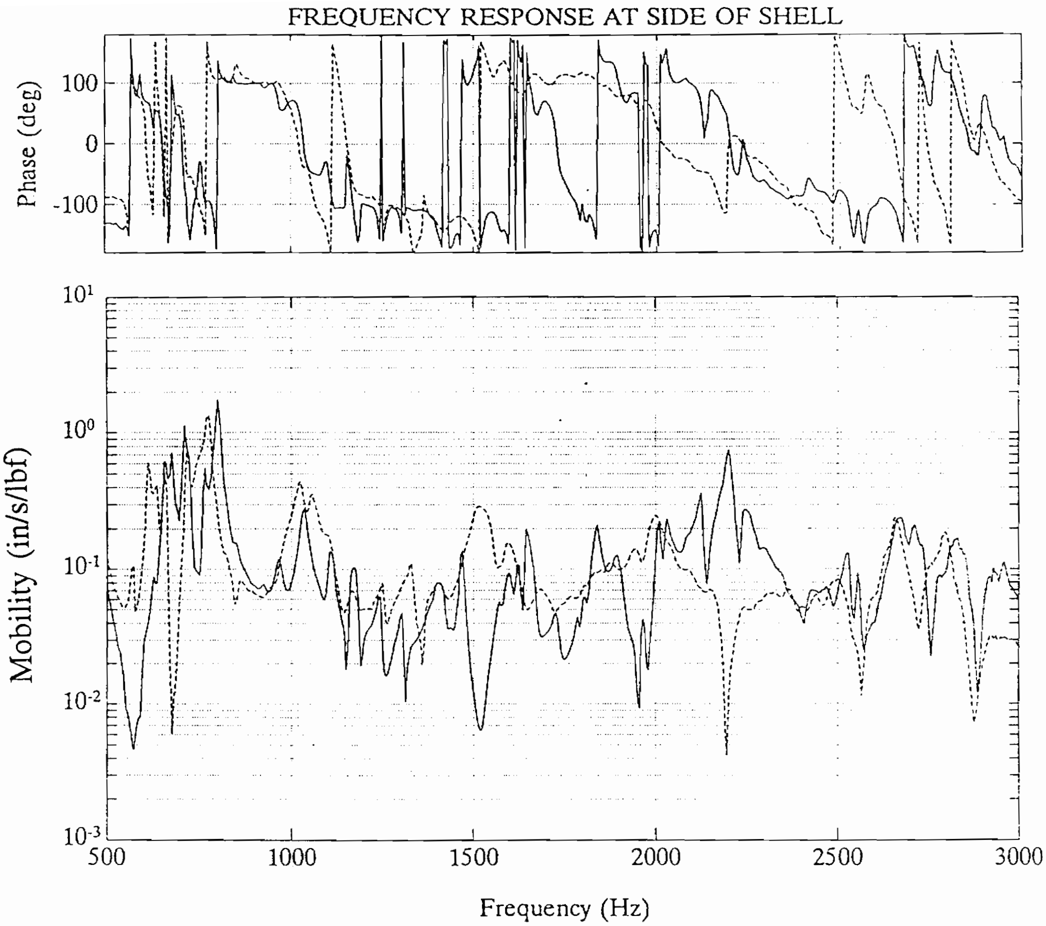

Fig. 3-17: Overlay of the mobility at side location #2
——————— Regular, ----- Instrumented

the small change in the FRF's. Since the most dominant peak on the top and substantial peaks at certain locations on the side occur in this frequency range, the reduction in response in this frequency range may be largely responsible for the instrumented compressor being quieter. The top spring force gage installation is probably responsible for this response change. The additional mass of the force gage and hardware along with the stiffening affect on the top should alter the natural frequencies and response amplitudes of the shell. Coupling between the top and side responses is indicated by these changes and has been observed in past impact testing of empty shells and assembled compressors.

The other substantial compressor assembly response change occurs at the top between 1600 and 1800 Hz. Reduction in shell response were not clear at the sides in this frequency range. The peaks in this range on the top were substantially less than the peak near 950 Hz so this reduction is probably not as important. There are some other response changes that can be attributed to either the modifications for the force gage installation or manufacturing variations. These other response changes should not substantially affect the acoustic radiation of the compressor during operation.

4.0 EXPERIMENTAL ANALYSIS OF THE COMPRESSOR

The compressor instrumentation allows several types of analyses to be performed. The most basic analysis is the recording of time-averaged, time-domain data to show the dynamic behavior during the compression cycle. This time-averaged data can be Fourier transformed into the frequency domain to determine the dominant harmonic content in each transducer measurement. These Fourier transformed forces can also be used to drive the finite element model of the compressor. The frequency-domain data required for the multiple FRF analysis will also show the harmonic content of each measurement. The multiple FRF analysis can provide additional insight into the system characteristics during operation and help determine potential noise reduction modifications.

The compressor was tested in the Noise and Vibration Control Lab at Virginia Tech. The compressor was run on a test stand located near the center of the back wall of the lab. The lab has cinder block walls with a concrete floor and is roughly 29 ft (8.8 m) wide, 49 ft (14.9 m) deep, and 14 ft (4.3 m) high. When viewing from the back of the lab, the left front corner of the lab is occupied by a pair of reverberation rooms which take up a 16 ft (4.9 m) wide and 18 ft (5.5 m) deep section of the room. The reverberation rooms have cinder block outer walls and create an L-shaped central lab area. The main entrance to the lab is to the right of the reverberation rooms. The compressor test stand provides the compressor load and is enclosed in a drywall box to prevent the freon and water flow noise from significantly affecting the acoustic measurements. Fiberglass batting was attached to the side of the box facing the compressor to reduce the reflected sound off that surface. The background noise level in the room, taken without the compressor running, was checked using a hand held sound level meter and was found to be less than 35 dB in all bands.

4.1 Transducer Measurements

The test data is acquired with a Zonic System 7000 16-channel FFT analyzer. This machine is controlled by the ZETA software on the Hewlett Packard workstation. Data is passed over the ethernet network from the analyzer to the workstation where many of the calculations are performed and the results stored. The transducers and associated hardware such as charge amplifiers and power units were connected as required for each of the tests. A Bruel & Kjær 2331 sound level meter with a 1/2 in (13 mm) microphone was used to measure the dynamic sound pressure radiated by the compressor.

4.1.1 External Microphone Measurements

One of the first steps in the data analysis is to acquire some microphone measurements to determine the peak-noise radiation frequencies. A representative time averaged trace from the microphone is shown in Fig. 4-1 and an autospectrum is shown in Fig. 4-2. Notice the harmonics of the 57 Hz operating speed of the compressor that

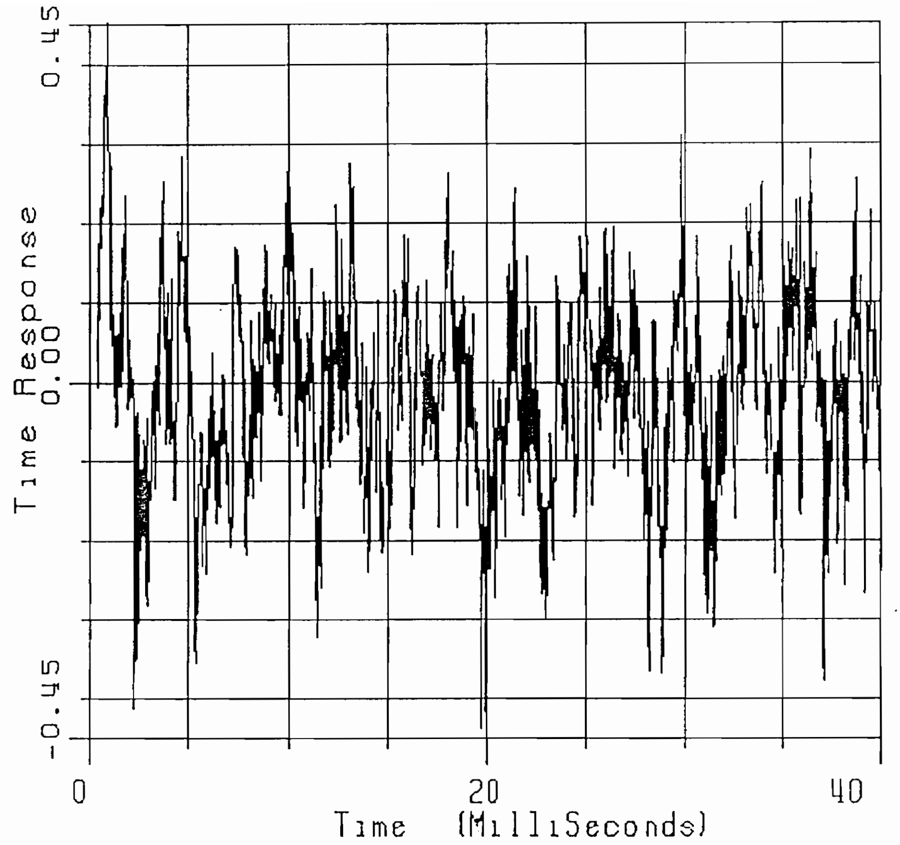

Fig. 4-1: Time averaged trace of the external microphone output using synchronous time averaging - instrumented H23A compressor

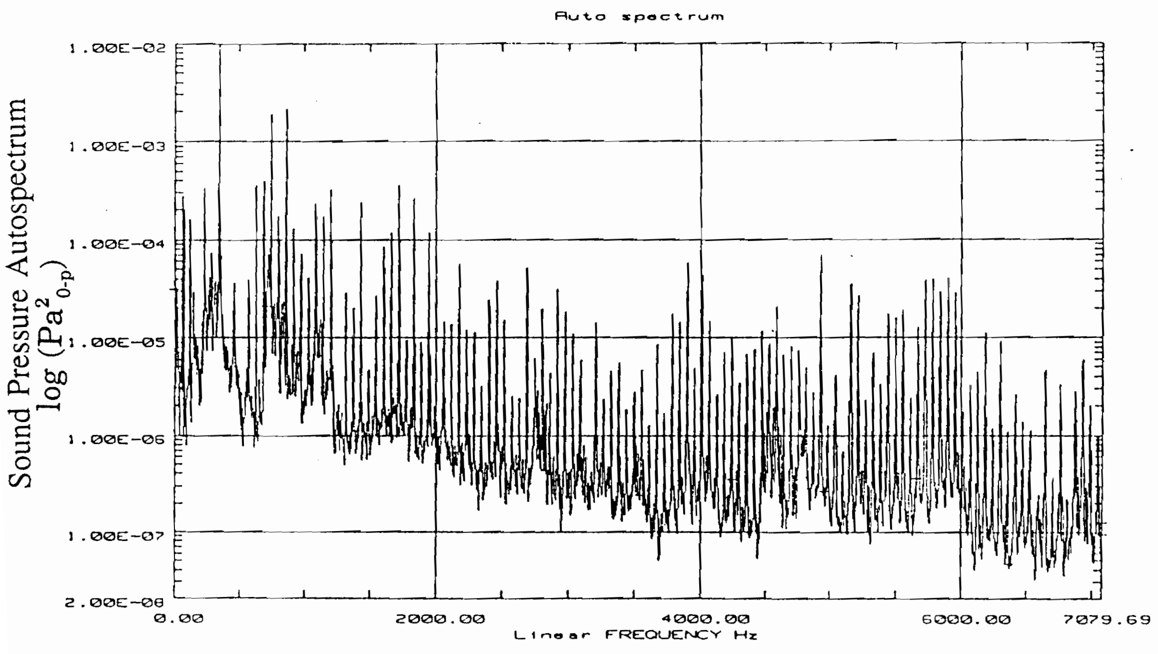

Fig. 4-2: External microphone autospectrum - instrumented H23A compressor

extend beyond 6 kHz. The most dominant peaks occur at the sixth, thirteenth, and fifteenth multiples of the operating speed. These occur at approximately 343, 745, and 860 Hz, respectively. Previous acoustic analysis of a regular compressor under normal operating conditions [1] showed dominant side radiation at 342, 741, and 969 Hz. The first two frequencies are nearly identical between the regular and instrumented compressor. The shell radiation that occurs at 970 Hz in the regular compressor has probably moved down to 860 Hz in the instrumented compressor due to the shell response changes discussed in Section 3.3.

4.1.2 Internal Compressor Measurements

All experimental measurements were made with the compressor warm and stable at the American Refrigeration Institute (ARI) standard operating condition which is approximately 76 psig (524 kPa) suction pressure and 297 psig (2048 kPa) discharge pressure. The magnetic probe pulse was used as a tach signal to trigger the data acquisition at the same point in the compression cycle. Each time block of data must be acquired at the same point in the compression cycle in order to properly time-average the dynamics of the compressor during operation.

The orientation of the three axes of each of the triaxial force gages relative to the compressor are shown in Fig. 4-3. The force gages were installed with the x-axis normal to the broad sides of the compressor, the y-axis normal to the narrow ends of the compressor, and the z-axis is the vertical axis. The top forces do not follow the right

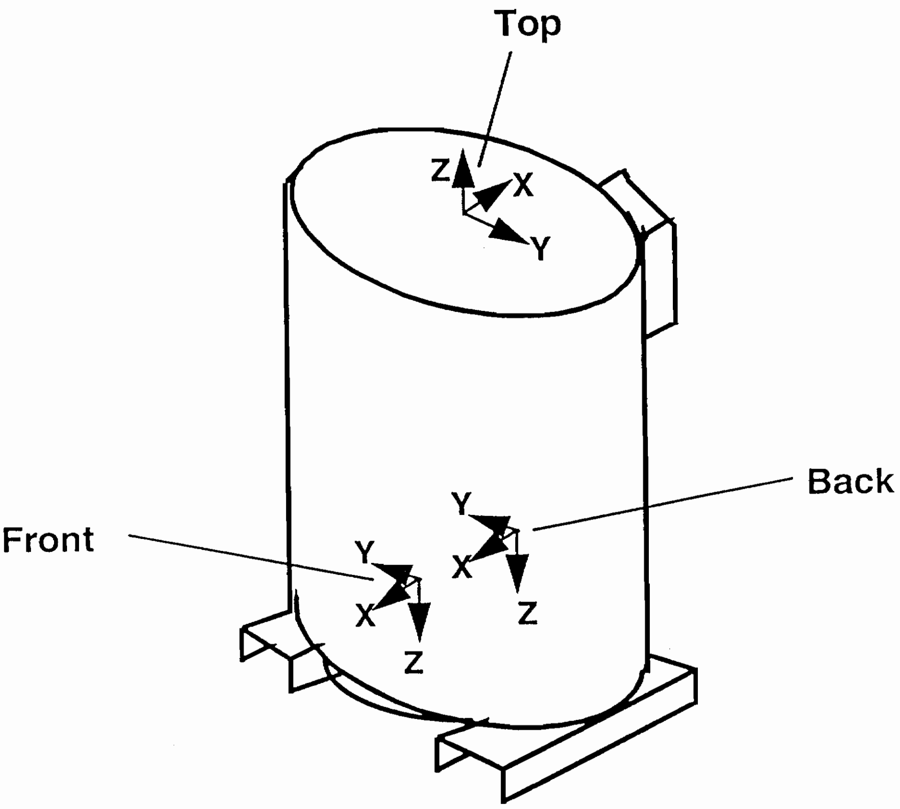

Fig. 4-3: Triaxial force gage orientation on the instrumented H23A

hand rule and are inverted relative to the two lower spring force gages. This is the result of the top spring mount installation and the force measuring characteristics of the triaxial force gage.

Two sets of time-averaged data were acquired from the 16 transducers installed in the compressor. The first set captured slightly more than two cycles of compressor operation and was acquired for time signature analysis where the signal dynamics during the cycle is the primary focus. The results from averaging 100 records of 2048 point time blocks sampled at 51.2 kHz are shown in Fig. 4-4. Most of the force signals show dominant first or second harmonic activity with the Top-Z force and shock loops as the main exceptions. There is significant higher frequency activity in the force signals with four high frequency bursts evident in a number of the force measurements. These bursts are probably valve chatter and correspond to the points in the cycle where the cylinder pressures peak and the discharge valves are opening. The cylinder time traces indicate that the discharge valves open smoothly but the discharge valves close and reopen several times during the discharge process. The discharge valves appear to close at least two to three times as the freon is being discharged from the cylinders and will create pressure pulsations in the muffler and shock loop. The biggest surprise is the high acceleration measured on the shock loop. The accelerometer was mounted on the shock loop pointed back toward the side of the muffler at a point approximately 3.5 in (89 mm) below the point where the shock loop exits the muffler. The measured acceleration is approximately 63 g peak-peak at that location and was significantly higher than expected.

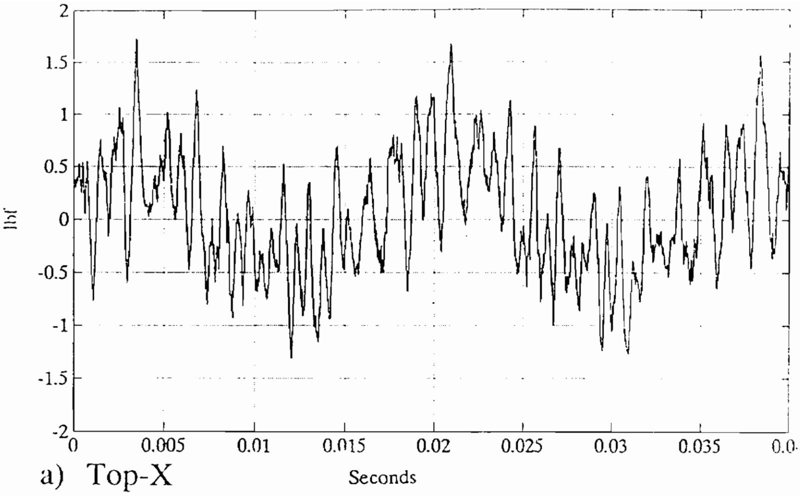

a) Top-X

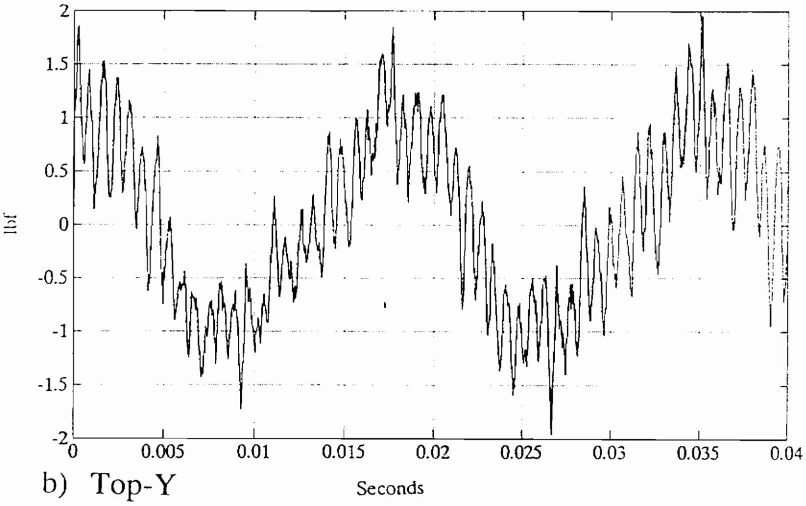

b) Top-Y

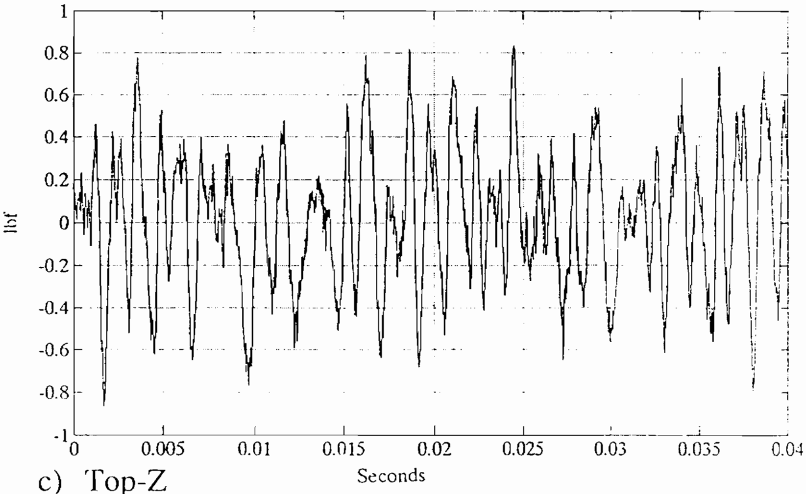

c) Top-Z

Fig. 4-4: Time-averaged transducer signals

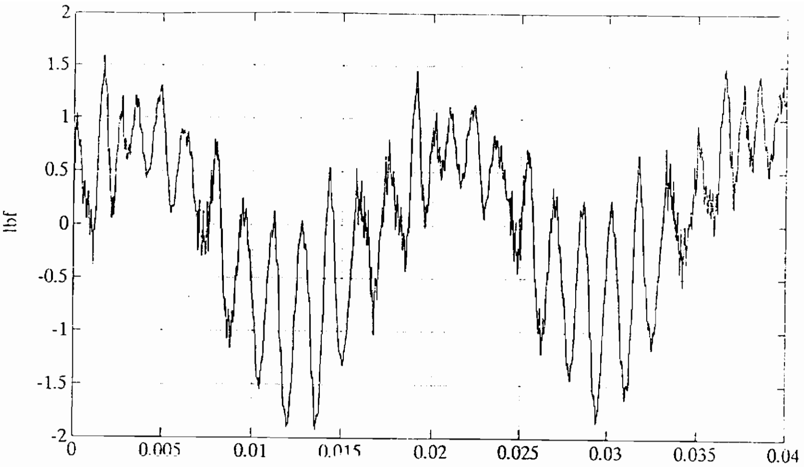

d) Front-X

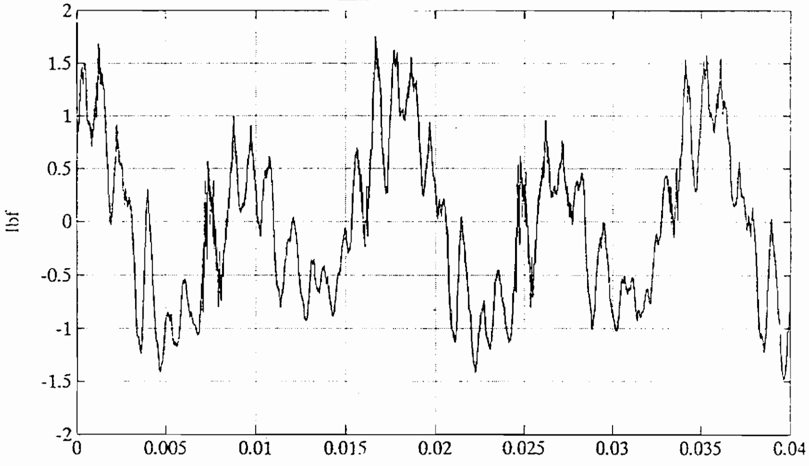

e) Front-Y

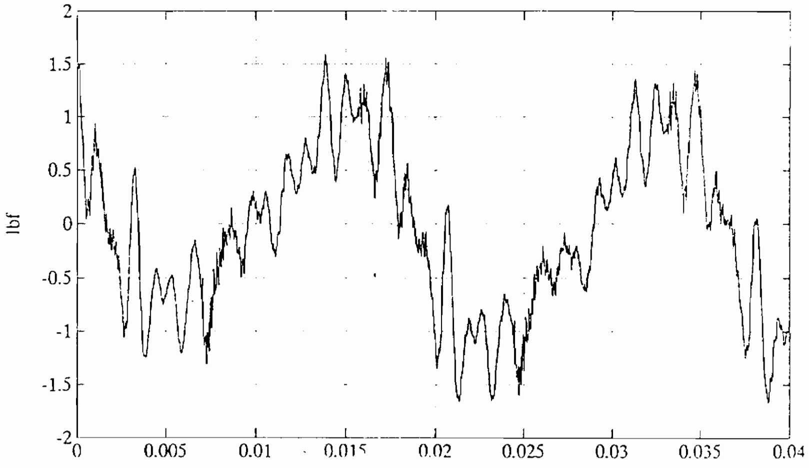

f) Front-Z

Fig. 4-4 continued

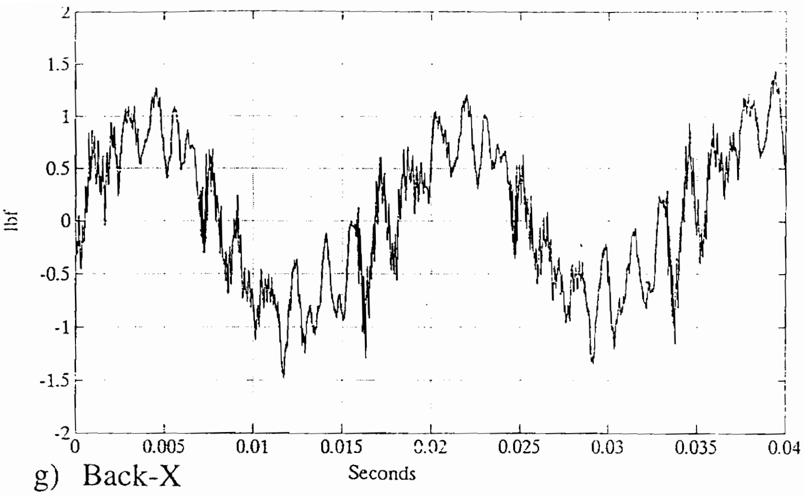

g) Back-X

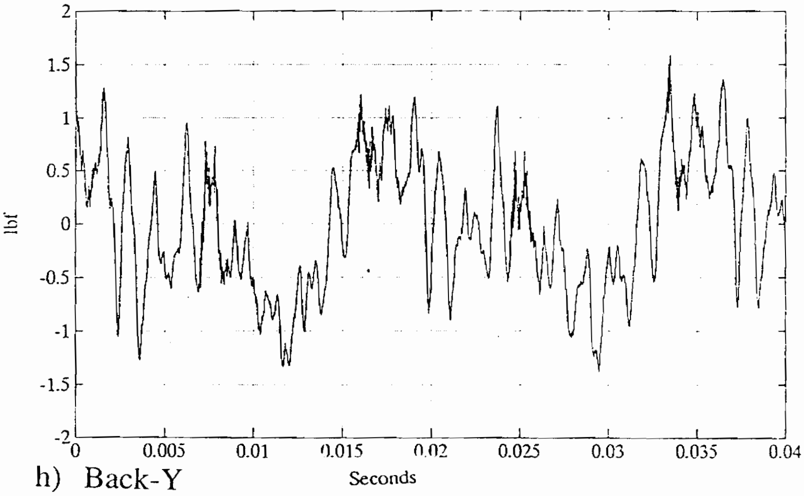

h) Back-Y

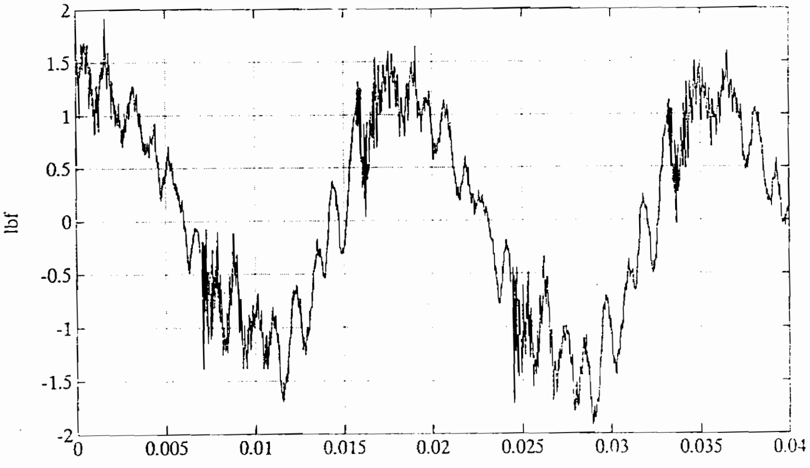

i) Back-Z

Fig. 4-4 continued

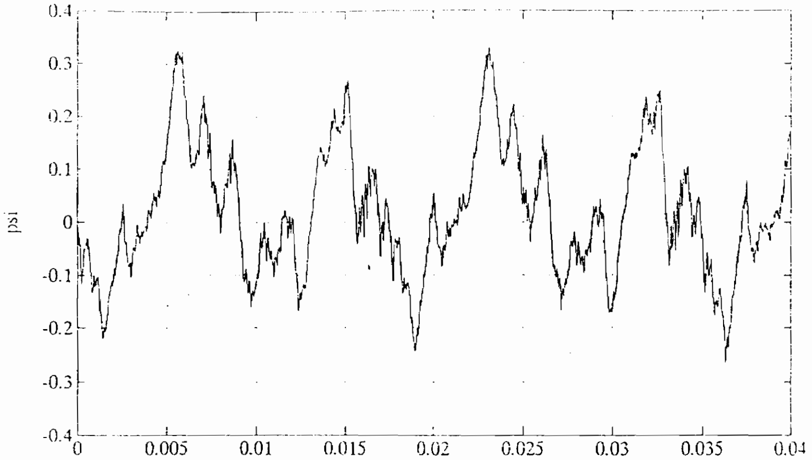

j) Housing pressure

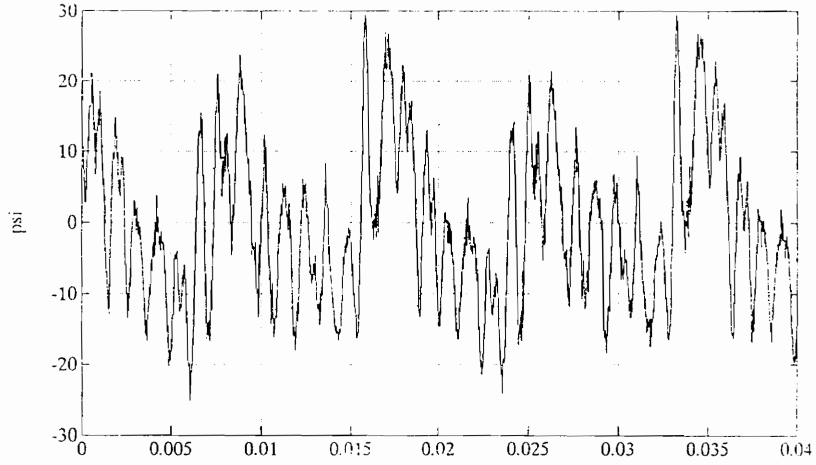

k) Muffler

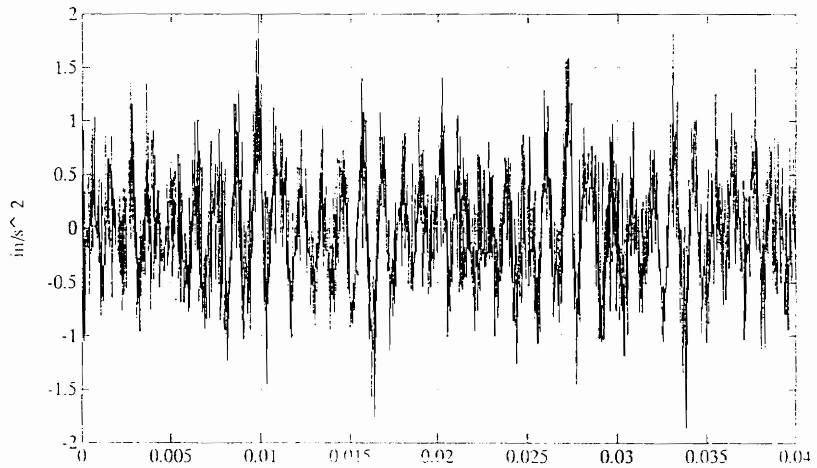

l) Shock loop

Fig. 4-4 continued

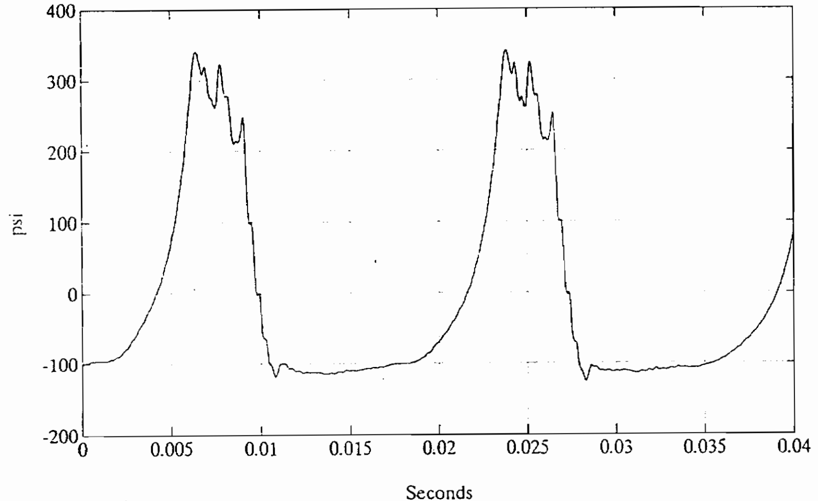

m) Top cylinder

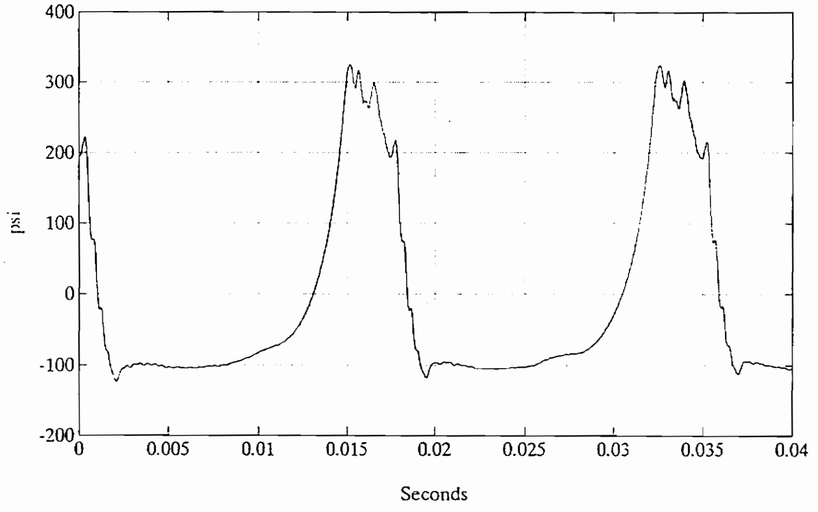

n) Bottom cylinder

Fig. 4-4 continued

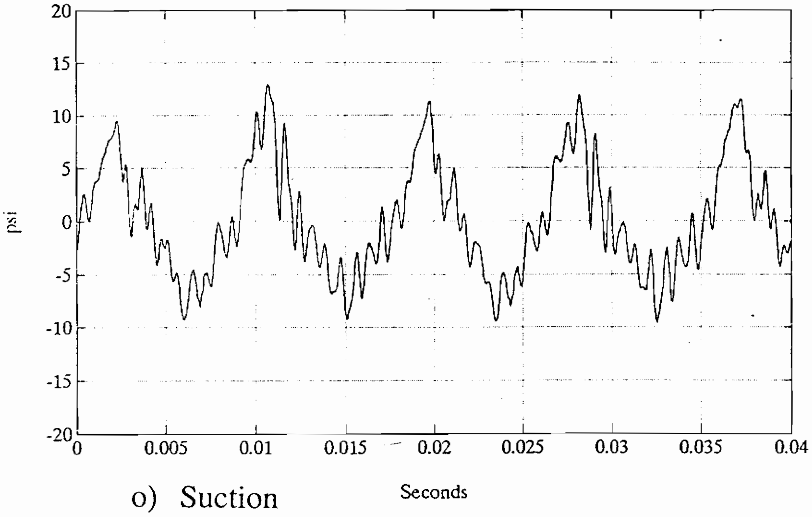

o) Suction

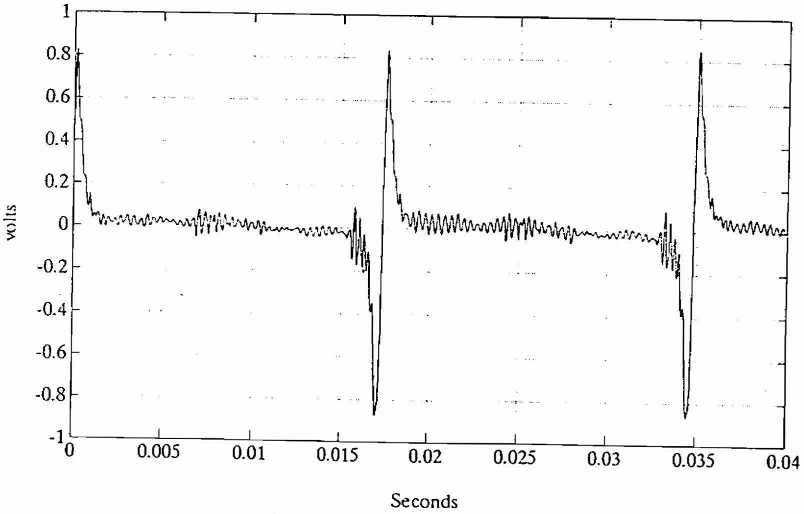

p) Tach pulse

Fig. 4-4 continued

A second set of time-averaged data was acquired with good frequency resolution of the FFT as the primary focus. The increased frequency resolution should improve the precision of the amplitude and phase values at the compressor harmonics in the FFT of each signal. The spectral values from the Fourier transforms of these time signals can be used to drive the finite element model of the compressor. The Bode plots of the complex Fourier transforms from the second set of time-averaged data are included in Appendix B. This second set of time data has a much better frequency resolution, 1.5625 Hz versus 25 Hz, than the time averages shown in Fig. 4-4 because the average of 200 records of 8192 point time blocks were acquired at a 12.8 kHz sampling rate.

Frequency-domain averaged autospectra and cross-spectra were acquired for the multiple-input single-output modeling presented in section 4.2. The autospectra for the forces, pressures, and acceleration are shown in Fig. 4-5. The autospectra have a frequency resolution of 1.5625 Hz and clearly show the rich harmonic content in each of the transducer signals.

The transducers, their time-averaged peak-to-peak magnitudes and dominant multiples of the compressor run speed are included in Table 4-1. The first and second multiple of the running speed dominate most of the transducer measurements. This is expected since one is due to running unbalances and the second due to the two compression cycles per revolution. The fifteenth multiple of the running speed, which is approximately 860 Hz, is also significant in many of the signals, especially in the shock-loop acceleration. The reaction forces that normally occur at 970 Hz in the regular

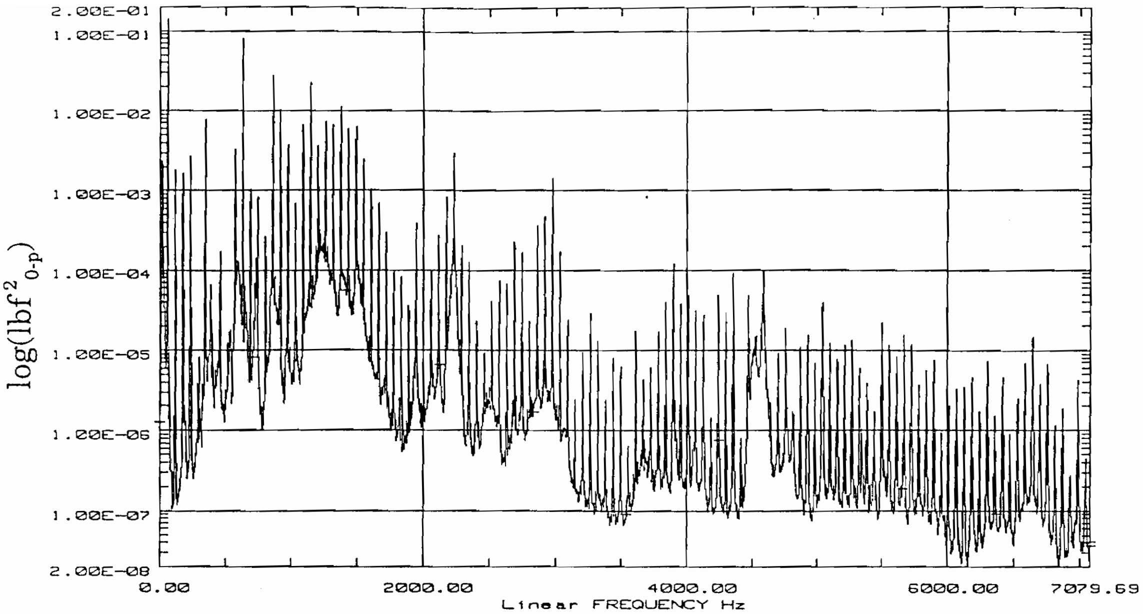

a) Top-X

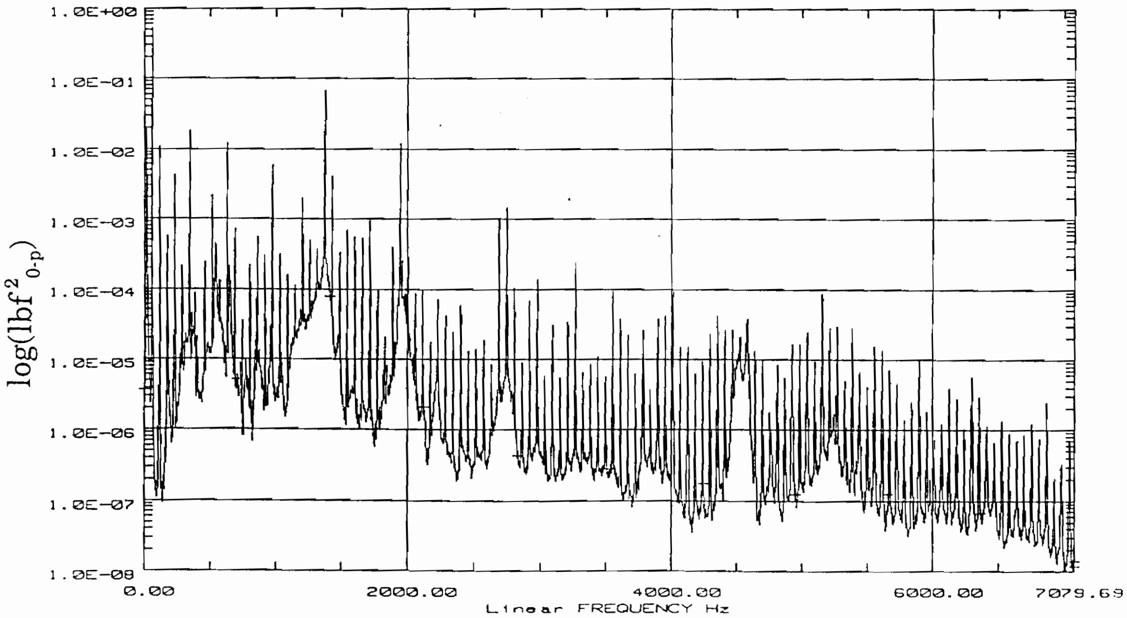

b) Top-Y

Fig. 4-5: Transducer signal autospectra corresponding to Fig. 4-4

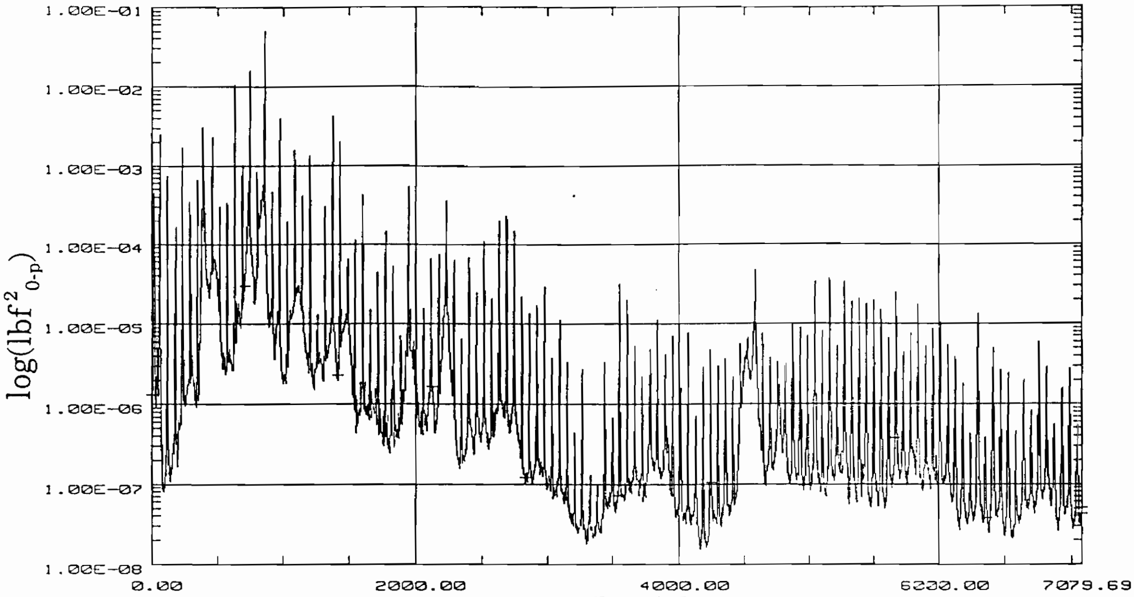

c) Top-Z

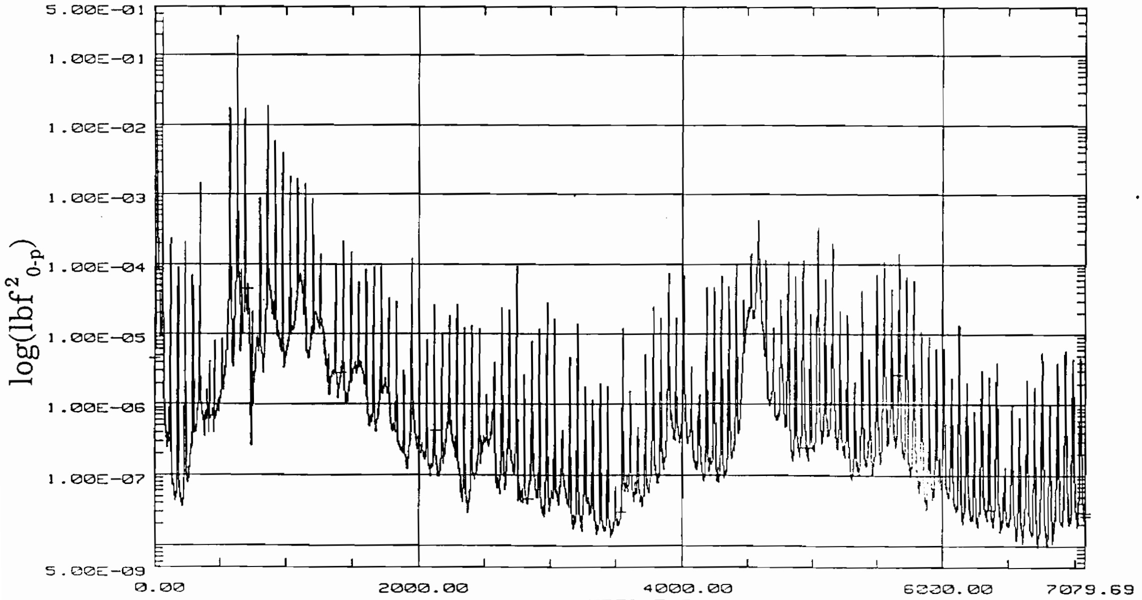

d) Front-X

Fig. 4-5 continued

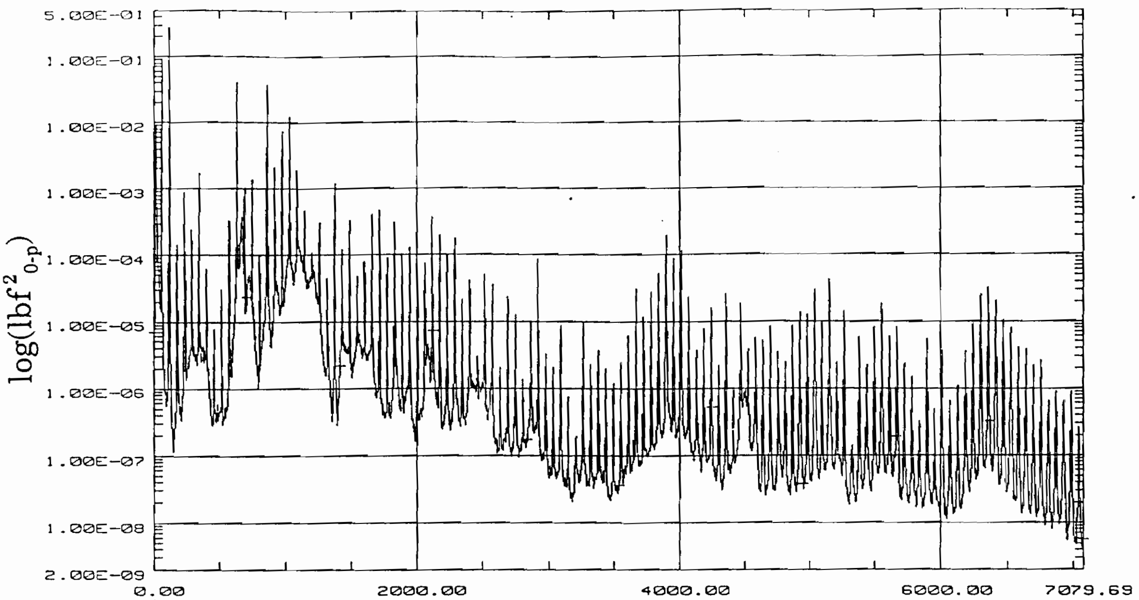

e) Front-Y

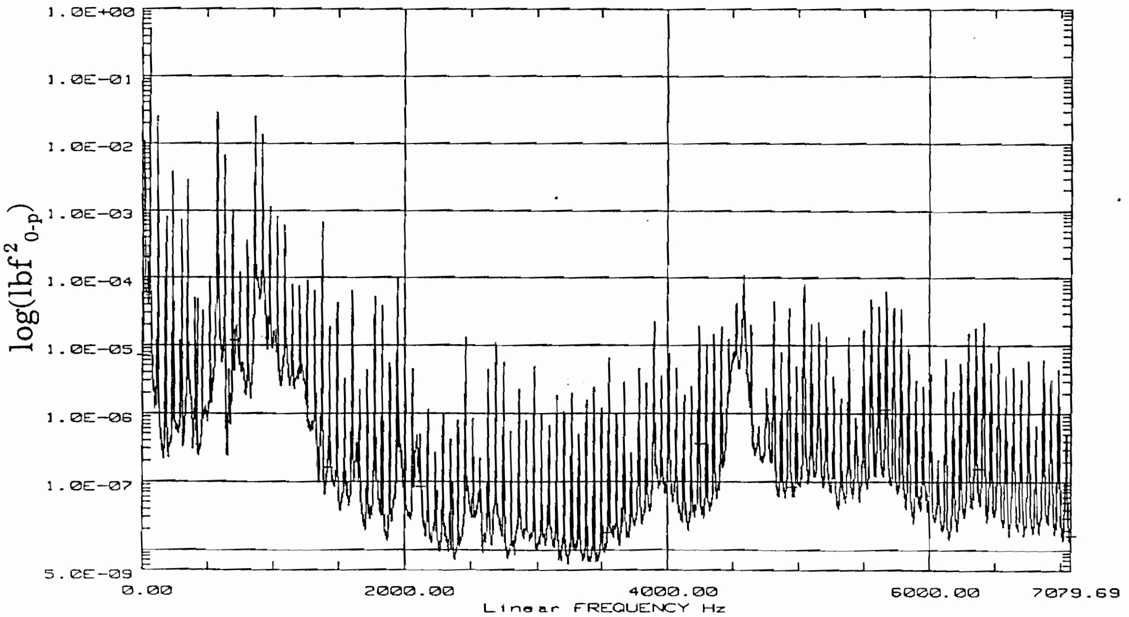

f) Front-Z

Fig. 4-5 continued

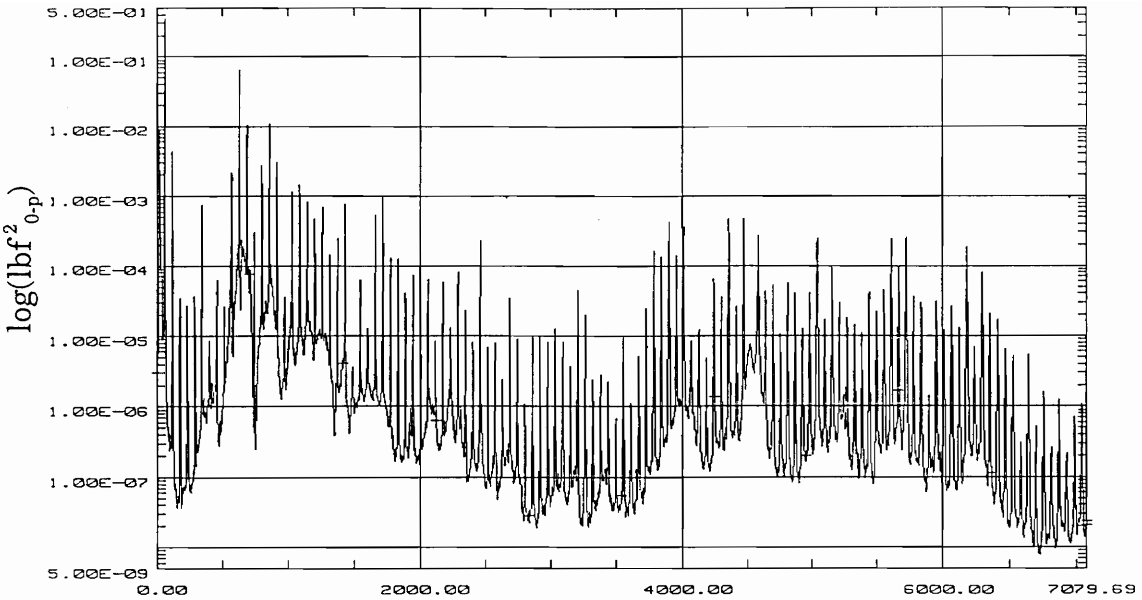

g) Back-X

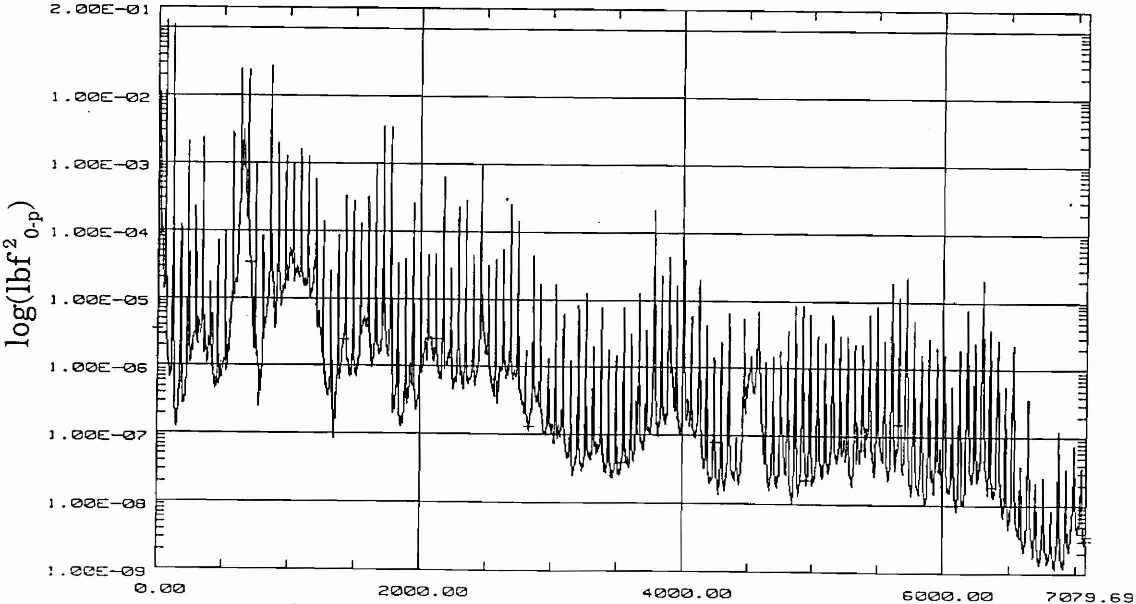

h) Back-Y

Fig. 4-5 continued

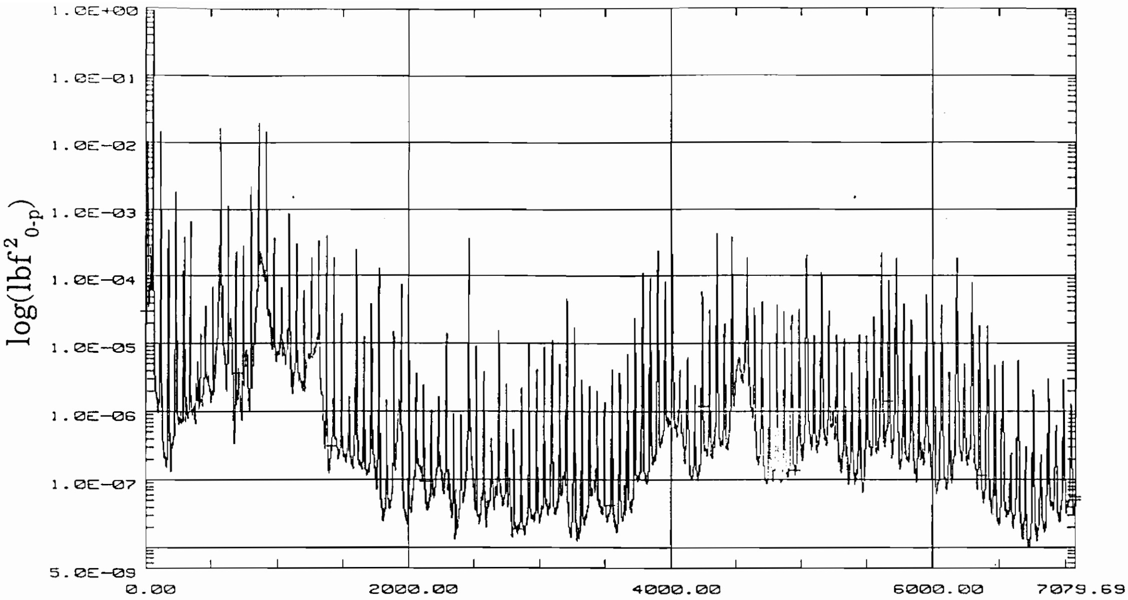

i) Back-Z

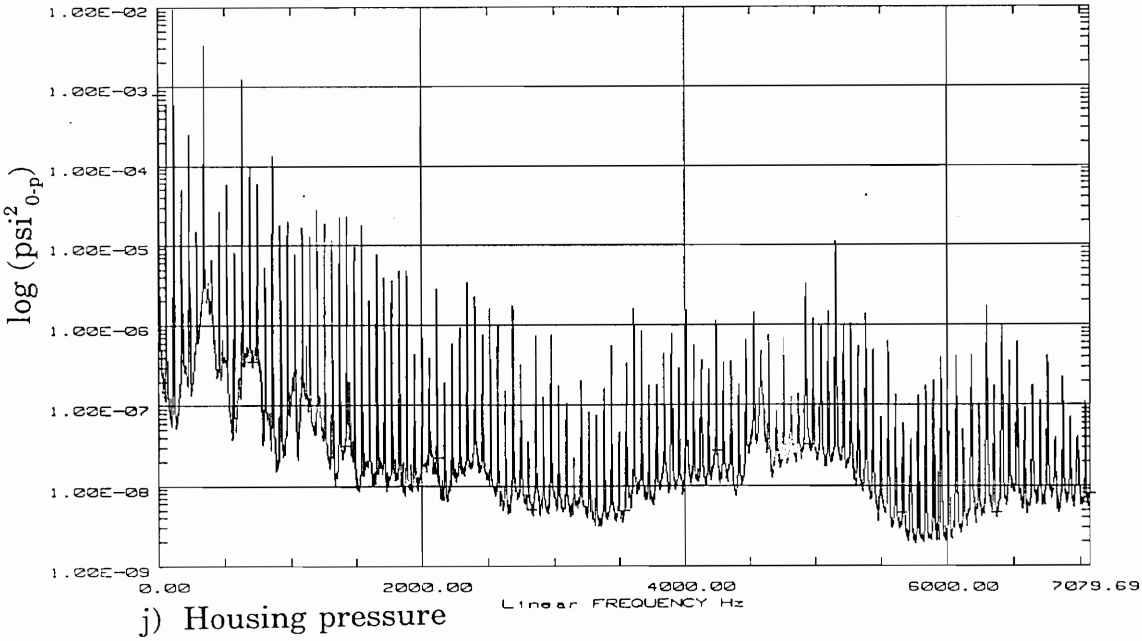

j) Housing pressure

Fig. 4-5 continued

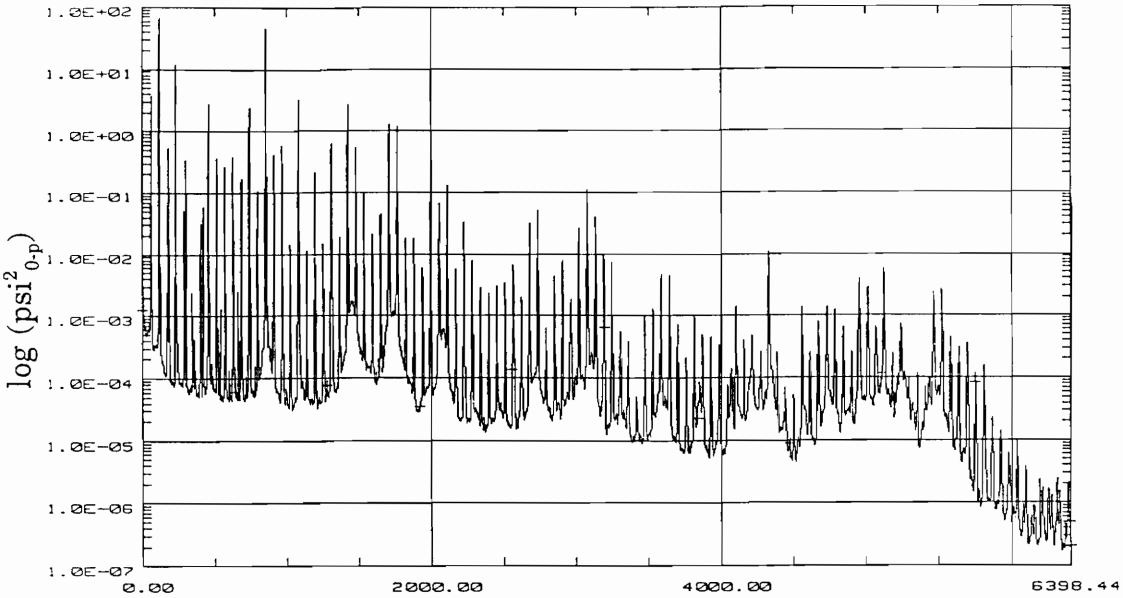

k) Muffler

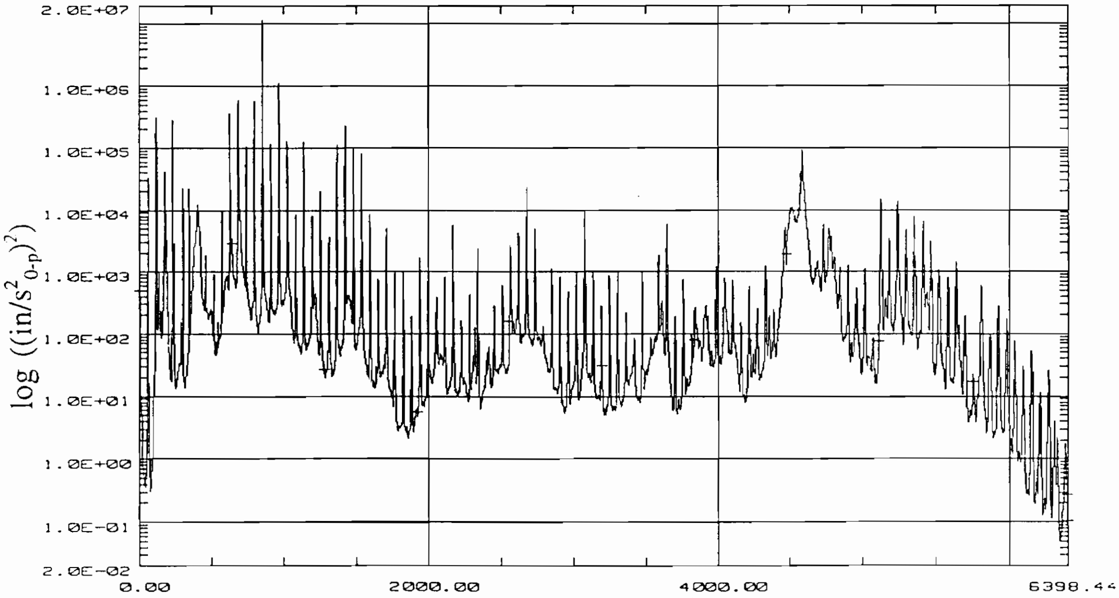

l) Shock loop

Fig. 4-5 continued

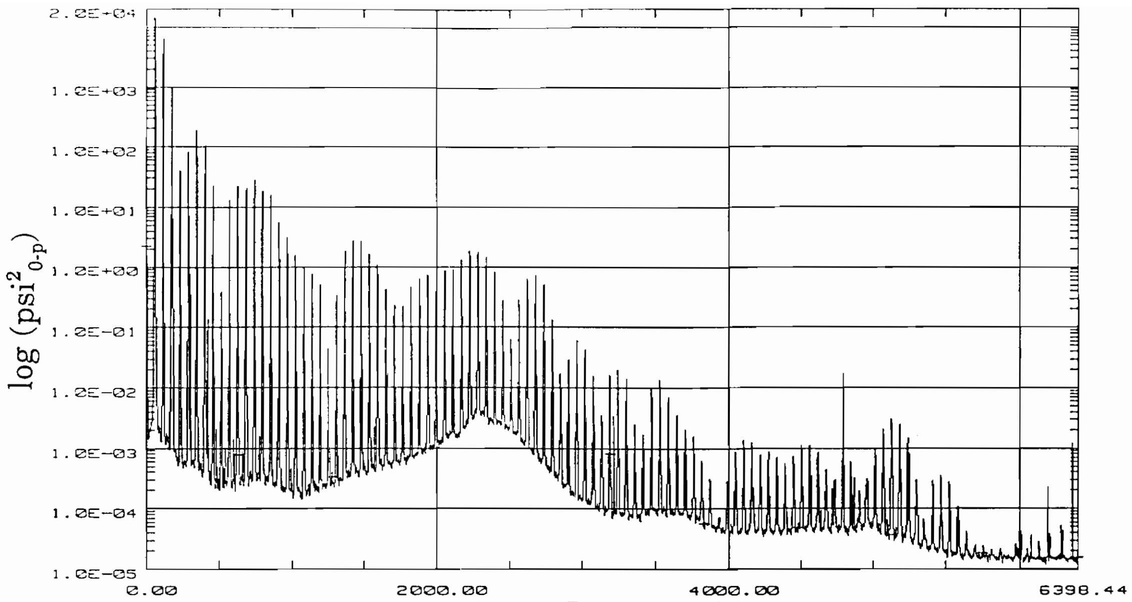

m) Top cylinder

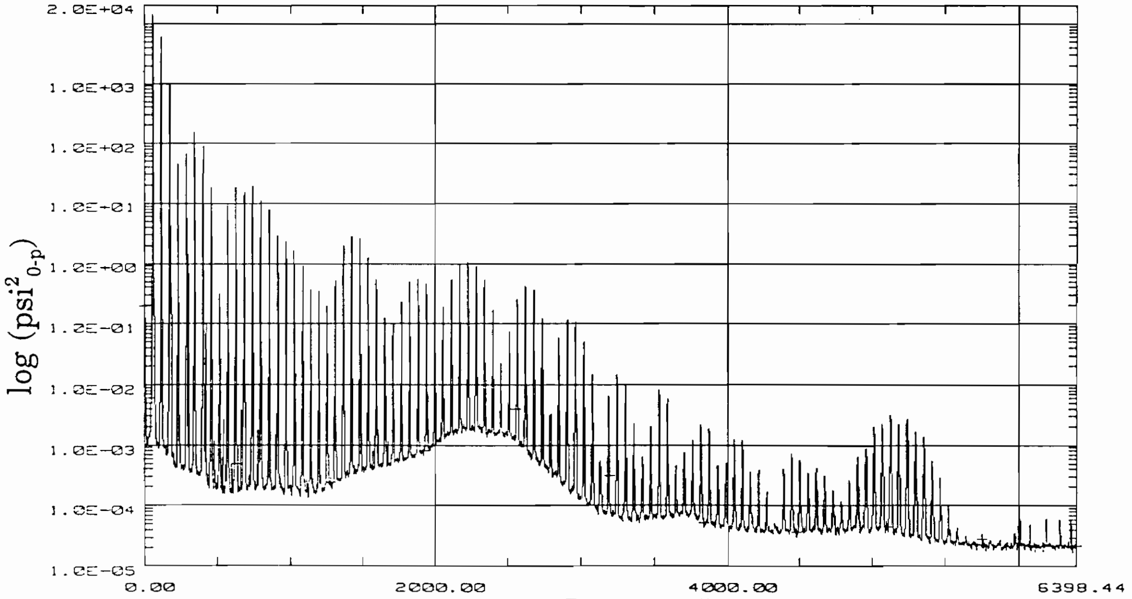

n) Bottom cylinder

Fig. 4-5 continued

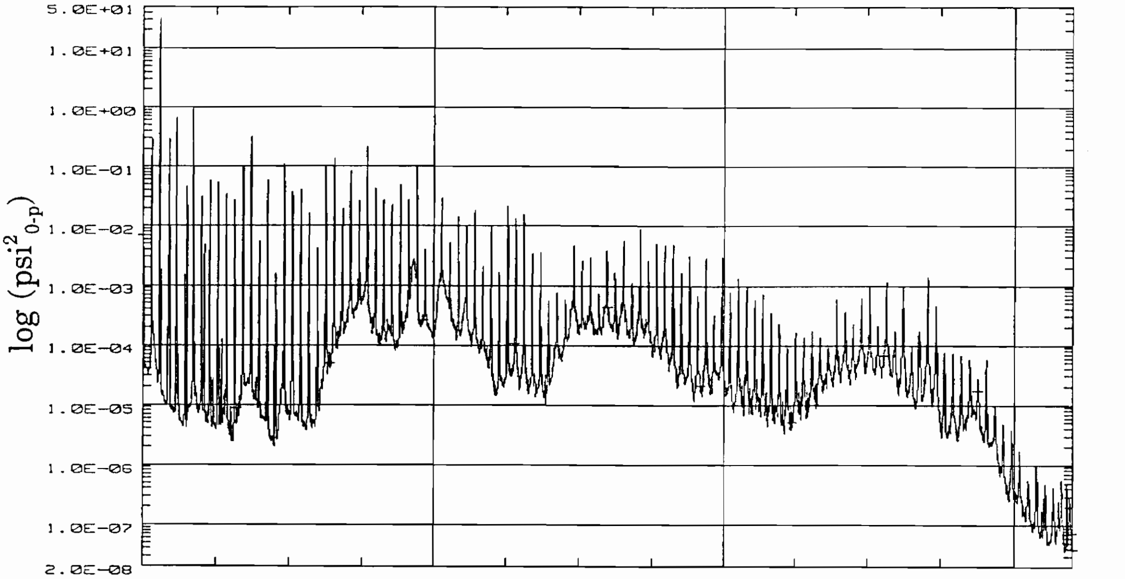

o) Suction

Fig. 4-5 continued

Table 4-1: Transducer time trace peak-to-peak magnitudes and dominant multiples of the compressor running speed

Transducer Location	Time Trace Magnitude (p-p)	Dominant Speed Multiples
Top-X	3.0 lbf (13.4 N)	1,11,15,21
Top-Y	3.9 lbf (17.4 N)	1,6,11,17,24
Top-Z	1.7 lbf (7.6 N)	11,13,15
Front-X	3.5 lbf (15.6 N)	1,10,11,12,15
Front-Y	3.3 lbf (14.7 N)	1,2,11,15
Front-Z	3.3 lbf (14.7 N)	1,2,11,15,16
Back-X	2.9 lbf (12.9 N)	1,11,12,15
Back-Y	3.0 lbf (13.4 N)	1,2,11,12,15
Back-Z	3.8 lbf (16.9 N)	1,2,10,15,16
Housing pressure	0.60 psi (4.14 kPa)	2,6,11
Muffler	54.7 psi (377 kPa)	2,4,15
Shock Loop	24250 in/s^2 (616 m/s^2)	15,17
Suction pressure	23.0 psi (159 kPa)	2,4,6
Top cylinder pressure	468 psi (3230 kPa)	1,2,3,6
Bottom cylinder pressure	450 psi (3100 kPa)	1,2,3,6
Tachometer	1.75 V	-------

compressor may be occurring at 860 Hz in the instrumented compressor. The mobilities from the impact tests on the instrumented and regular production H23A compressor presented in Chapter 3 indicate that the instrumentation installation substantially reduced the modal activity between 900 Hz and 1000 Hz. This is clearly shown by the overlay plots of the top mobility (see Fig. 3-15) and the side location #1 mobility (see Fig. 3-16). A peak near 860 Hz is present in the instrumented compressor which was a low response region in the regular compressor. The system resonance that was originally near 970 Hz in the regular compressor has moved down to 860 Hz due to the modifications required to instrument the compressor, particularly the installation of the three force gages. The prevalence of this harmonic in the triaxial force gage signals helps to explain the dominance of the sound radiation at the fifteenth multiple in the instrumented compressor and the seventeenth multiple in the regular compressor. There is significant vibrational energy transfer between the compressor and shell through the support springs in the 800 Hz to 1000 Hz frequency range.

4.2 Multiple-Reference FRF Analysis

Several multiple input - single output models were analyzed to determine the dominant noise transmission paths and potential noise sources in the compressor. The harmonic nature of the compressor during operation made it difficult to determine when an adequate model had been created. A model is generally determined to be adequate when the model accounts for a significant portion of the output, with the multiple coherence greater than 0.7 [9] serving as one guideline. There was uncertainty determining the proper model for the path analysis. The most logical model is a ten-input model composed of the nine signals from the three triaxial force gages and the housing pressure. The housing pressure was the only pressure included in the model because it represents the refrigeration gas path that can drive the compressor shell. Removing the housing pressure as an input created a nine-input model composed of the triaxial forces which accounts for nearly the same portion of the microphone output that the ten input model does. The harmonic excitation functions of the compressor make it difficult to prove the proper minimum input model since the coherence between individual inputs were usually close to unity at the dominant harmonic sound peaks. It was assumed that the spring forces and housing pressure are the primary transmission paths. Now the task is to determine which of these paths dominate in noise generation.

A multiple-reference analysis requires several of the relationships developed in Chapter 2. This analysis requires the solution of the matrix relationship given in Eq. (2.42). Normally this is accomplished by a form of Gaussian elimination and back substitution as described in Section 2.4.2. After the FRF vector has been determined, most of the analysis involves the summation equation given in Eq. (2.55):

$$G_{yy} = \sum_{i=1}^{m} \sum_{j=1}^{m} H_i^* \, H_j \, G_{ij} \tag{4.1}$$

where *m* is the number of inputs. This summation is the predicted output from the model and will be equal to the product of the total partial coherence calculated from Eq. (2.65) and the output autospectrum. This total coherent output autospectrum indicates the portion of the actual measured output that is linearly related to the measured system inputs. Any unaccounted sources, non-linearity in the transmission paths, and uncorrelated noise on the input and output signals will reduce the predicted output relative to the actual measured output.

The relationship between the model inputs and the output in Eq. (4.1) can be used for several analyses to determine the system characteristics. One of the most basic is to determine the direct contribution of each input to the output by setting *i* and *j* equal to the input of interest and calculating the output autospectrum. If the predicted output for the direct contribution of an input is significantly less than the measured output autospectrum then the input is not a strong contributor. The summation equation can also be used in a shielding study where the effects of certain system inputs can be removed. This shielding is performed by setting the FRF for the shielded inputs to zero and performing the summation. This result can then be compared to the model total coherent output from Eq. (4.1) to determine the reduction from removing the inputs in question. The greater the reduction when an input is removed, the more dominant the contribution of that input is in the output. These two analyses can help determine the importance of each individual input and will indicate if there is high cross-cancellation between the inputs when the summation of these direct contributions is substantially higher than the actual measured output or if removal of an input through shielding increases the predicted model output.

An upper limit on the input selection for this highly coherent system could be established by checking the total coherent output power. When I-DEAS Test computes the multiple-input FRF vector at a spectral line and a singularity occurs in the solution, the coherence is set to zero for that spectral line. The singularity will occur if there is unity coherence between any of the inputs or between the output and one of the inputs. A singularity will also occur if there is no remaining uncorrelated signal content, within the numerical precision of the calculations, left in an input signal during the processing. In terms of the matrix relationship shown in Eq. (2.42), a singularity indicates the the input spectral matrix G_{xx} could not be inverted to compute the FRF vector H. The shock-loop accelerometer as an additional input to any other transducer group would always yield a coherence of zero for spectral lines greater than approximately 20 Hz. The accelerometer motion should be very similar to, and thus highly correlated with, the motion of the compressor motor and crankcase stack because of its mounting location on the shock loop pointing toward the muffler. Since it probably measures most of this motion, the coherence between the accelerometer and some of the triaxial force gage signals is probably close enough to unity that the force transducer signals lack enough incoherent content to stabilize the numerical procedure. The addition of the suction or muffler pressure to the combination of the triaxial force gages and the housing pressure yielded zero coherence at certain compressor harmonics. This could be detected by displaying an overlay plot of the microphone and model coherent output autospectra. The coherent output autospectrum will always be less than or equal to the microphone autospectrum unless there is a bug in the computational algorithm. The singular harmonic frequencies were easy to identify since the coherent output power was zero which left that particular harmonic completely one color in the color overlay plot. The harmonics with zero coherence are probably frequencies where the suction or muffler pressures are fully coherent with the housing pressure. This is expected of the suction pressure since the freon for compression is drawn directly from the inside of the shell where the housing pressure is measured. On the other hand, the muffler is not open to the housing; however, there is the possibility that the muffler could have significant radiation into the housing.

The multiple FRF analysis was performed on one primary group of transducers. The noise transmission path model is composed of the following ten inputs:

- Three triaxial force gages (9)
- Housing pressure (1)

The noise path model appeared to give good results. An attempt was made to determine the importance of each spring and its triaxial forces to the noise radiation. There is significant cancellation between these forcing functions in the output and their individual importance was difficult to determine. The focus was changed to treating the three support springs as a group in the analysis. The removal of spring contribution in the multiple input model will leave the portion of the output contributed by the housing pressure along with the uncorrelated portion of the output. This gives a potential noise reduction if the compressor could be mechanically perfectly isolated from the compressor shell. This is not possible in actual practice, but less significant reductions may be possible with an elastomer or wire rope springs in place of the current support springs. The elastomer or wire rope can potentially dissipate in the form of frictional losses some of the energy currently passing through the spring. This should reduce the amplitude of the mechanical forcing functions driving the shell. Moreover, the elastomer spring should have significantly fewer internal continuum mechanics resonances thus lowering the system modal density. The probability of a forcing function exciting a resonance mode will likewise be reduced.

4.2.1 Microphone Measurement Locations

The three microphone locations used in the multiple-input FRF analysis are shown in Fig. 4-6. A steel security cage surrounded the test stand and compressor which limited the unobstructed microphone locations available for testing. The microphone locations are 3.28 ft (1 m) away from the compressor shell at location 1 and 2 ft (0.6 m) at locations 2 and 3. These locations will be in the near field of the compressor below a certain frequency. This frequency is dependent on the distance from the compressor surface and is affected by the size and radiation pattern of the compressor. One estimate of the transition from the near field to the far field is the relationship $kr < 10$ [32], where k is the acoustic wave number and r is the distance from the machine. The wave

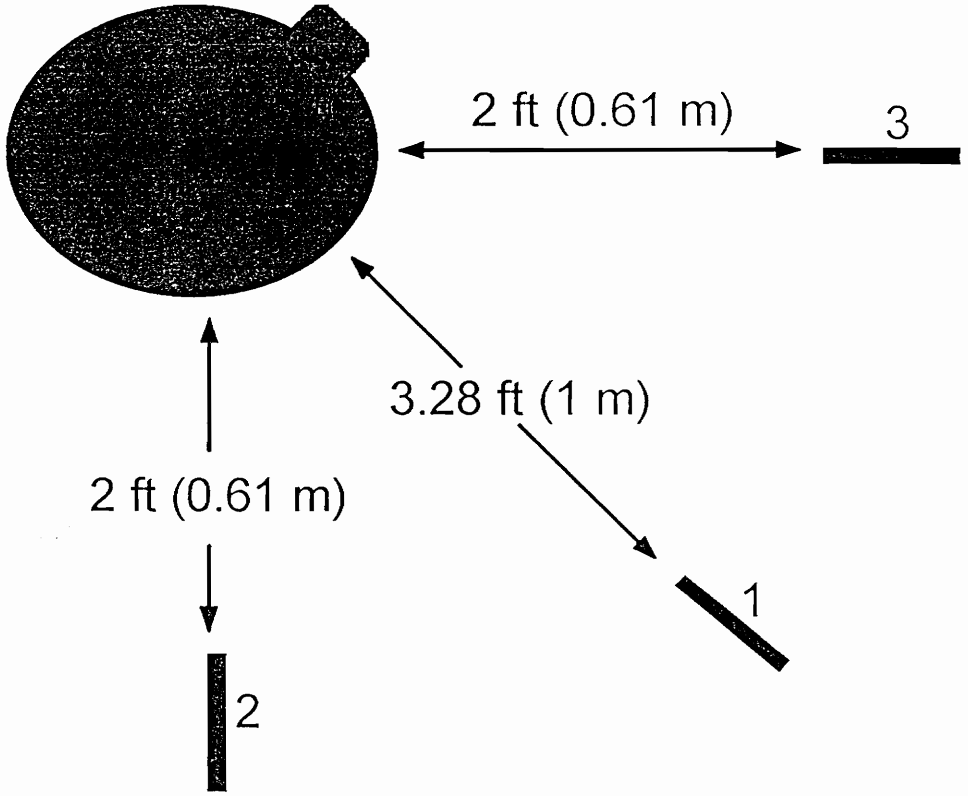

Fig. 4-6: Microphone locations used for the sound measurements

number is the ratio of the frequency in rad/s divided by the speed of sound in air. The speed of sound in air is approximately 13500 in/s (343 m/s) which yields near-field transitions at 545 Hz at location 1 and 895 Hz for locations 2 and 3. At each location the sound level meter was pointed at the center of the compressor and the microphone positioned approximately at the level of the compressor beltline. The same frequency ranges were not used for all of the measurement locations but the resolution was held constant at 1.5625 Hz. Location 1 was the primary test location and extends to cover the 6300 Hz octave band and locations 2 and 3 were used as checks on the low frequency results of the analysis of location 1 and only extend through the 2000 Hz one-third octave band.

The estimated one-third octave sound pressure levels at the three measurement locations are shown in Fig. 4-7. The third-octave sound pressures were A-weighted to reflect the frequency dependent change in perceived loudness. The ear is most sensitive in the 1 kHz to 6.3 kHz third-octave bands. The sensitivity rolls off below 1000 Hz. The weighting can have an effect on the analysis of the compressor sound distribution. The 315 Hz third-octave band was the strongest when the measurements are unweighted. When the third-octave bands are A-weighted, the 800 Hz and 1000 Hz third-octave bands become more important. The A-weighting subtracts 6.6 dB for the 315 Hz third-octave band, subtracts 0.8 dB for the 800 Hz band, and adds 0 dB for the 1000 Hz third-octave band. The weighting can affect the selection of the third-octave bands for sound reduction, since the third-octave bands below 630 Hz and above 8000 Hz are penalized

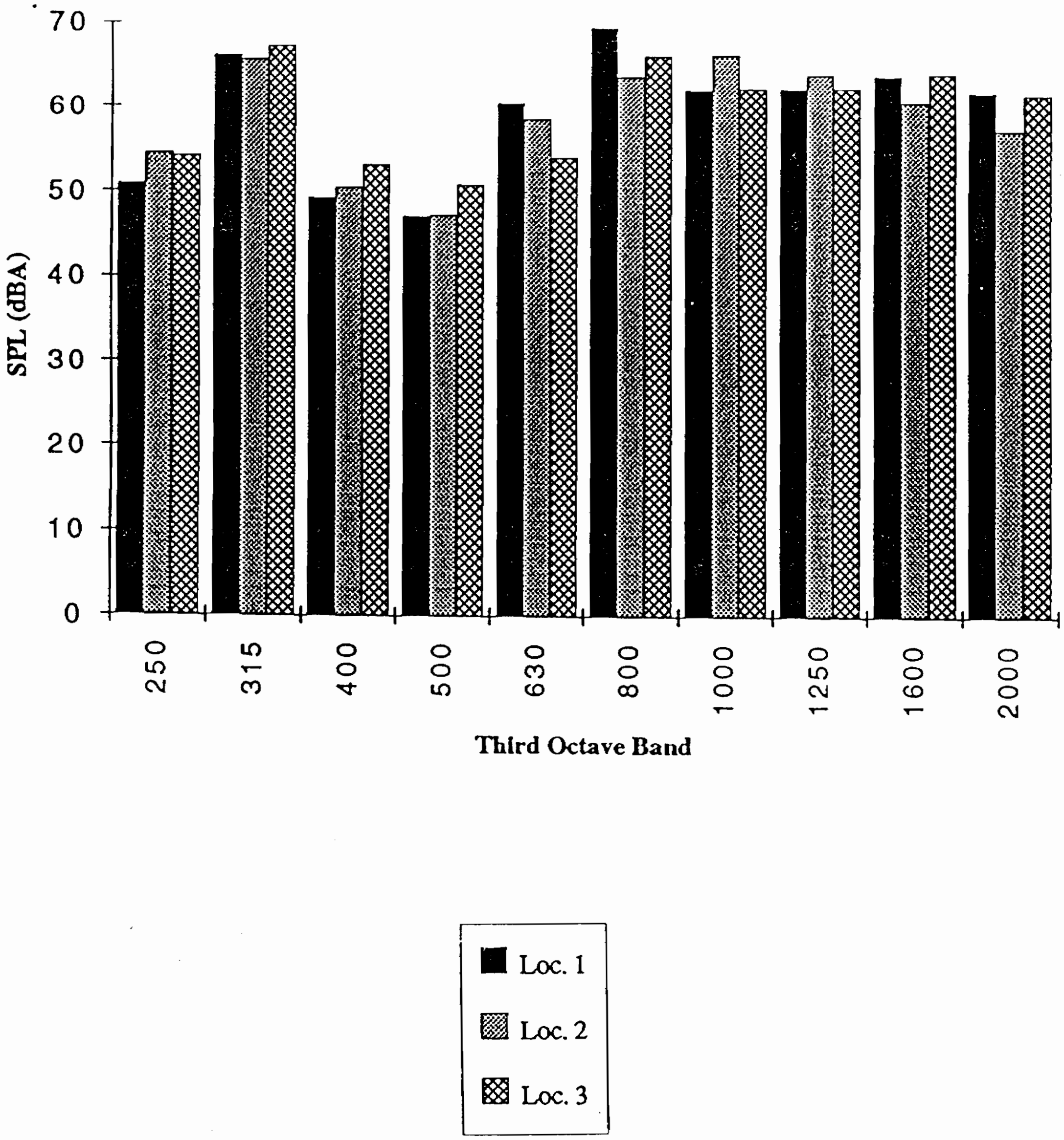

Fig. 4-7: Third-octave sound pressure levels measured at the three test locations

by more than 2.0 dB. The A-weighting does have an effect on the compressor sound pressure distribution since most of the radiated sound is in the 800 Hz to 6300 Hz third-octave bands and will reduce the significance of the 315 Hz third-octave band content. The 315 Hz third-octave band is important, but the third-octave bands near 1000 Hz need to be attenuated to achieve significant sound reduction.

The levels for each one-third octave band varies with the microphone location. Significant sound radiation occurs in the 315 Hz one-third octave band at all three locations. There is a substantial decrease in sound radiation in the 400, 500, and 630 Hz third-octave bands. Radiation increases back to the 315 Hz levels for the 800 through 2000 Hz one-third octave bands. The peak one-third octave values for each microphone location varies with location 1 peaking at 800 Hz, location 2 at 1000 Hz, and location 3 at 315 Hz. The coherent output power for each test was very high with the 10-input model accounting for approximately 95% of the sound power at the microphone. The microphone output and coherent output power calculated from the 10-input model are shown in Fig. 4-8. The correlation is very good for the sound radiation above 65 dB and becomes poorer as the levels drop toward 50 dB.

4.2.2 Direct Contribution Analysis

The model output autospectrum summation given in Eq. (4-1) combines two types of energy paths between the inputs and the output. The first type is the direct path from each input to the output. The model output autospectra for this type of path are

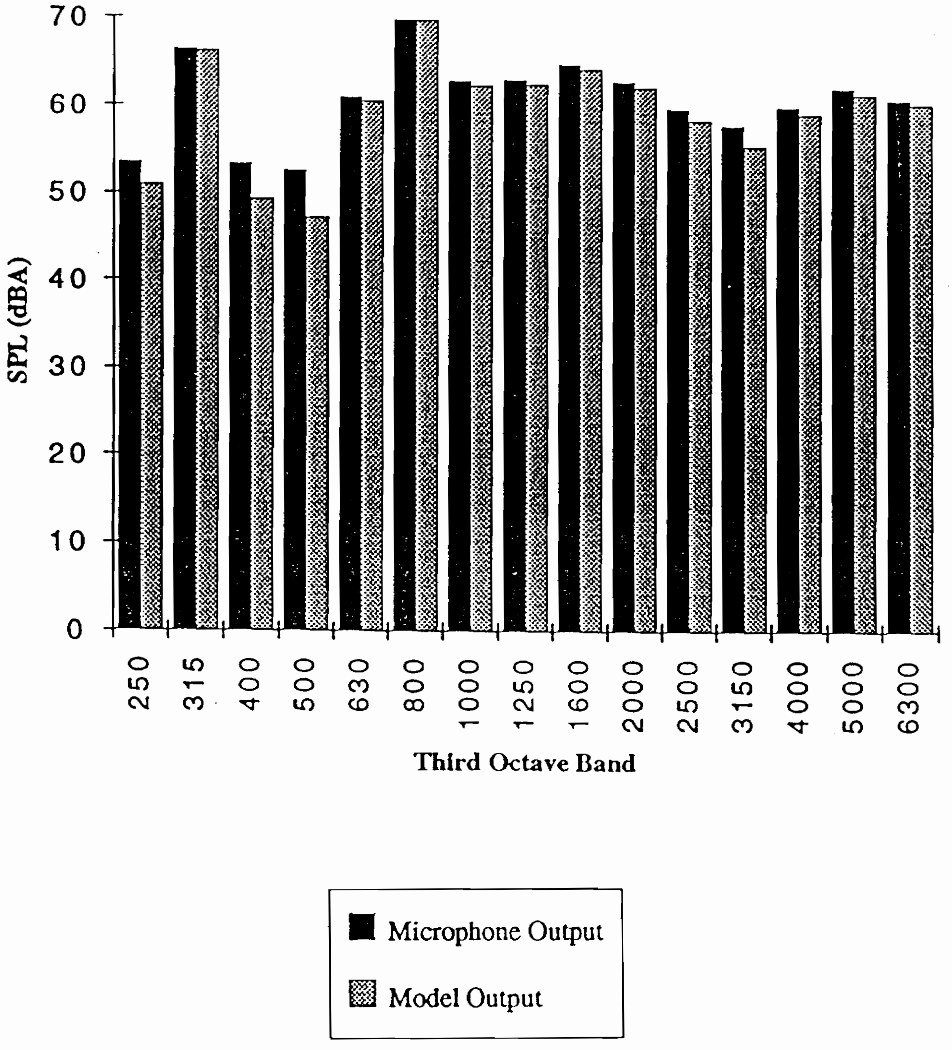

Fig. 4-8: Measured sound pressure levels and 10-input model coherent output for test location 1

calculated when the summation indices i and j in Eq. (4-1) are equal. The other type of path is dependent on the correlation between the inputs, represented by the cross-spectra between the inputs, and accounts for the correlated content in the inputs. The contributions from this second type of path are calculated when the summation indices i and j in Eq. (4-1) are not equal. The correlated path contributions will be zero for a system with mutually uncorrelated inputs, which could be modeled as a parallel set of single-input single-output models.

The direct contribution analysis looks at the contributions to the output autospectrum that come through the direct path from each input. The direct contribution analysis for an input simply takes the product of the input autospectrum and the square of the magnitude of its FRF, then compares it to the total model output autospectrum. If the direct contribution from an input is substantially more than the other inputs then that input should be the dominant source in the multiple-input model. The results of the direct contribution analysis on the path model for the three microphone locations are shown in Table 4-2. The total model output along with the direct contributions of the nine force inputs, housing pressure, and the uncorrelated signal content are given in dBA sound pressure level (SPL). The results are computed from the sum of the 250 Hz to 6300 Hz one-third octave bands for location 1 and the 250 Hz to 2000 Hz one-third octave bands for locations 2 and 3. The largest direct contributor at location 1, with a total model output of 74.4 dBA, is the Back X force at 72.8 dBA with fairly significant contributions from most of the other inputs at this location. The significance of the Back

Table 4-2: The predicted direct sound pressure contribution in dBA of each input to the 10-input noise transmission path model output along with the total model output

Transducer	Location 1	Location 2	Location 3
Total Model Output	74.4	72.2	72.7
Top X	70.0	61.4	64.0
Top Y	71.0	65.9	68.1
Top Z	70.4	70.0	69.7
Front X	70.7	69.9	68.6
Front Y	69.1	66.9	65.4
Front Z	70.6	68.7	65.3
Back X	72.8	67.9	66.5
Back Y	70.3	65.7	66.3
Back Z	71.3	64.6	66.9
Housing Pressure	68.8	63.7	61.7
Uncorrelated Content	64.8	61.5	63.2

X spring contribution at this location is interesting since this spring is located on the opposite side of the compressor from the microphone location. The least significant input at this location, by a margin of 4.0 dBA, is the uncorrelated content at 64.8 dBA. Location 2, with a total model output of 72.2 dBA, has the Top Z and Front X virtually equal as the dominant contributors at 70.0 dBA and 69.9 dBA respectively. Several of the other inputs, led by the Front Z at 68.7 dBA and the Back X at 67.9 dBA also make significant contributions. The least significant contributors at this location, by a margin of over 2.2 dBA, are the Top X at 61.4 dBA and the uncorrelated content at 61.5 dBA. The housing pressure and Back Z are also relatively small contributors at 63.7 dBA and 64.6 dBA respectively. At location 3, with a total model output of 72.7 dBA, the Top Z is the largest direct contributor at 69.7 dBA followed by the Front X at 68.6 dBA and the Top Y at 68.1 dBA. Like location 2, location 3 has several small contributors including the housing pressure at 61.7 dBA, uncorrelated content at 63.2 dBA, and Top X at 64.0 dBA.

The direct contributions from the inputs vary with microphone location. Location 1 has many inputs contributing at a similar level to the output with only the uncorrelated content as the only insignificant contributor. The Back X force input does stand out clearly as the most dominant input. The front location 2 and the right side location 3 both have fewer main contributors than location 1. The Top Z and Front X are dominant in the direct contributions at locations 2 and 3. The importance of the Top Z, Front X, and Back X forces is interesting. These are the spring forces that are normal to the compressor shell surface and should be very effective in driving the shell modes. The difference in results at the three locations should come from the relationship between the radiated noise patterns from particular shell modes and the ability of each forcing function to drive those modes. This potentially explains why the Back X force at the corner and the Top Z force at the front and right side are significant contributors. This analysis does show that at all three locations the housing pressure was not a strong contributor to the measured microphone output in the 10-input model, especially at locations 2 and 3 where the housing pressure was more than 6 dBA less than the most dominant contributor. The housing pressure is more significant at location 1 with a direct contribution only 3 dBA less than the most dominant contributor at that location.

The direct contribution analysis may be misleading for the compressor since it does not account for the correlated content between the inputs, which is significant in this application. This importance can be illustrated by summing the direct contribution components at each location and comparing those values to the total model output. The direct contribution summations are significantly higher than the total model output power at all three locations, with the summation accounting for 431% of the total model output at location 1, 325% at location 2, and 266% at location 3. This indicates that significant cancellation is occurring in the model output calculation due the correlated content and casts doubt on the conclusions from this direct contribution analysis.

4.2.3 Shielding Study

The shielding study uses both the direct path and correlation path energy in its contribution estimate. In the shielding analysis an input, or group of inputs, along with the correlated model content is removed from the predicted model output. The shielding combination that yields the lowest model output is the most significant contributor. A shielding analysis was performed for each of the three microphone locations using the same data used for the direct contribution analysis. In the shielding analysis of the 10-input model, the predicted output of the model is calculated for the shielding of each individual spring force, the housing pressure, the three forces from each individual spring, the lower support springs as a pair, and all three springs combined.

The shielding of the forces from all three springs will leave the direct contribution of the housing pressure in the model output. This analysis can verify whether the springs or the housing pressure is the major noise transmission path. It can also help determine which springs are the most significant contributors. The direct contribution analysis results indicate there is significant cancellation of the transmission path contributions at the microphone locations. Assuming the compressor shell natural modes dominate the radiated sound from the compressor, this cancellation would indicate that the forcing functions measured by the triaxial force gages and the housing pressure transducer drive the shell modes at relative phases that destructively interfere with each other. The direct contribution analysis accounts for several times the actual model output. The contributions from the inputs are phase cancelling at the output and makes it possible for the model output with an input shielded to be larger than the original total model output.

The results of the shielding reductions from isolating each transducer signal is presented in Table 4-3. These shielding results are not consistent from location to location and the shielding usually increased the predicted model output, indicating that the correlated content was more significant than the direct contribution of the input. The largest reduction was 1.0 dBA for the Top-Y force at location 3 and the most substantial increase was 1.8 dBA from shielding the Back-Z force at location 1. These results indicate that no substantial reductions can be achieved by trying to neutralize any of the

Table 4-3: The predicted model output sound pressure in dBA from the shielding of each input in the 10-input noise transmission path model

Transducer	Location 1	Location 2	Location 3
Total Model Output	74.4	72.2	72.7
Top X	75.0	72.4	73.3
Top Y	74.8	72.6	71.7
Top Z	75.6	73.3	72.8
Front X	74.8	73.3	73.0
Front Y	75.6	72.5	72.6
Front Z	75.4	72.5	73.5
Back X	74.7	72.4	72.9
Back Y	75.6	72.6	73.2
Back Z	76.2	72.9	73.4
Housing Pressure	74.5	72.0	72.9

individual transmission paths represented by these measurements. Moreover, the correlated content of each of the shielded transducers must have been phase cancelling the output contributions from the other transducer outputs if the shielded result is greater than the original total model output.

The next step was to group the 10 inputs to represent the actual paths. The three triaxial forces for each spring were shielded to represent the triaxial force exerted by each support spring, the six forces from the two lower support springs were shielded to determine the contribution from the lower suspension, and all nine forces were shielded to estimate the sound reduction if all three springs behaved as ideal isolators. The results from this shielding study for the three microphone locations are given in Table 4-4. Some mild reduction from shielding the top spring forces is seen at all three microphone locations, ranging from 0.2 dBA at location 2 to 2.3 dBA at location 3. The front and back spring shielding did not consistently attenuate the predicted model output. Shielding the lower springs as a pair led to larger reductions than the top spring shielding, with the reductions ranging from 1.6 dBA at location 1 to 3.2 dBA at location 2. The most substantial reductions occur when all three springs are isolated, which leaves only the housing pressure direct contribution, yielding a 5.5 to 11.0 dBA reduction in predicted model output. These results indicate that the springs are driving the natural modes of the shell and are shifted in phase so that there is significant cancellation in the output. The

Table 4-4: The predicted model output sound pressure in dBA from the shielding of the support springs

Shielded Springs	Location 1	Location 2	Location 3
Total Model Output	74.4	72.2	72.7
Top	73.9	72.0	70.4
Front	74.9	71.1	72.5
Back	73.5	72.2	72.4
Lower Pair	72.8	69.0	70.8
All	68.8	63.7	61.7

predicted sound pressure with the housing pressure contribution and the suspension spring contributions shielded separately is plotted against the model output for locations 1, 2, and 3 in Fig. 4-9. The housing pressure shielding does not show significant reductions in the sound pressure predictions relative to the shielding of the spring contributions. This shielding study indicates that the spring forces are the dominant transmission path to the compressor shell.

4.2.4 Conclusions

The direct contribution and shielding analyses on the 10-input path model indicate that the three support springs are the dominant transmission path between the compressor and the shell. The dynamic housing pressure was not found to be a substantial transmission path overall. It may be a contributor at the lower frequencies but does not appear to be a major transmission path over the frequency range where the compressor radiated noise is substantial. The separate shielding of the top spring forces and the lower suspension springs as a pair yielded mild reductions in the model output. The shielding of all springs yielded the most dramatic reductions. The prediction reductions from removing the spring forces are as follows:

• top spring:	0.2 - 2.3 dBA
• lower spring pair:	1.6 - 3.2 dBA
• all springs:	5.6 - 11.0 dBA

More realistic results for actually attenuating the spring forces is probably 4 - 6 dBA.

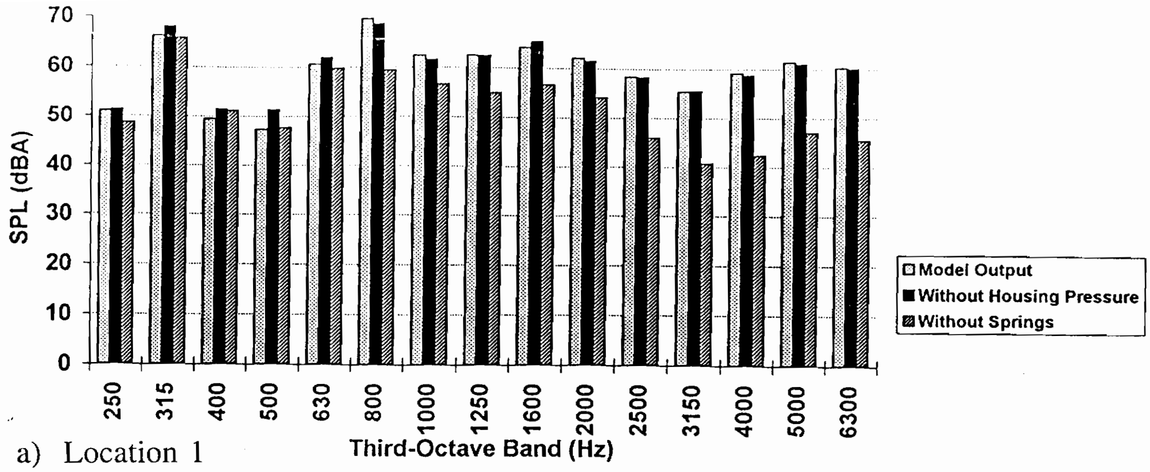

a) Location 1

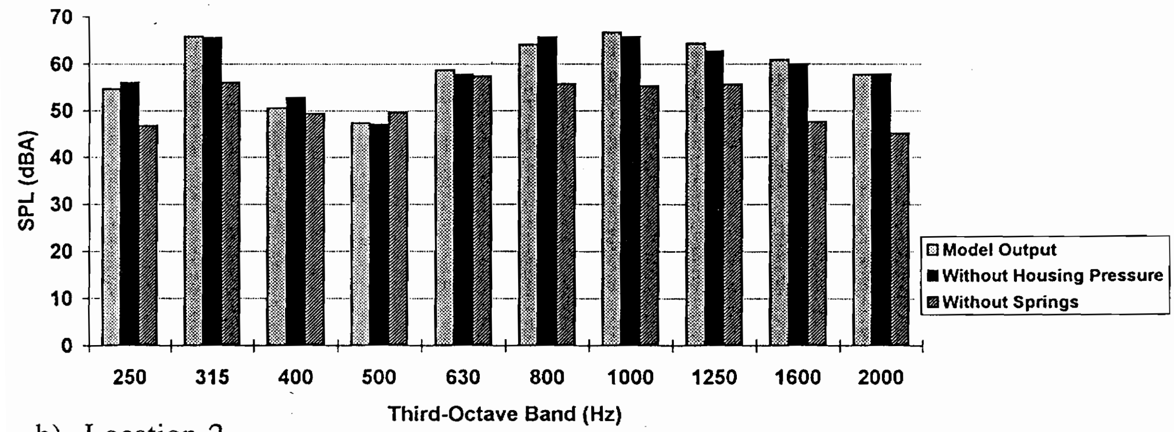

b) Location 2

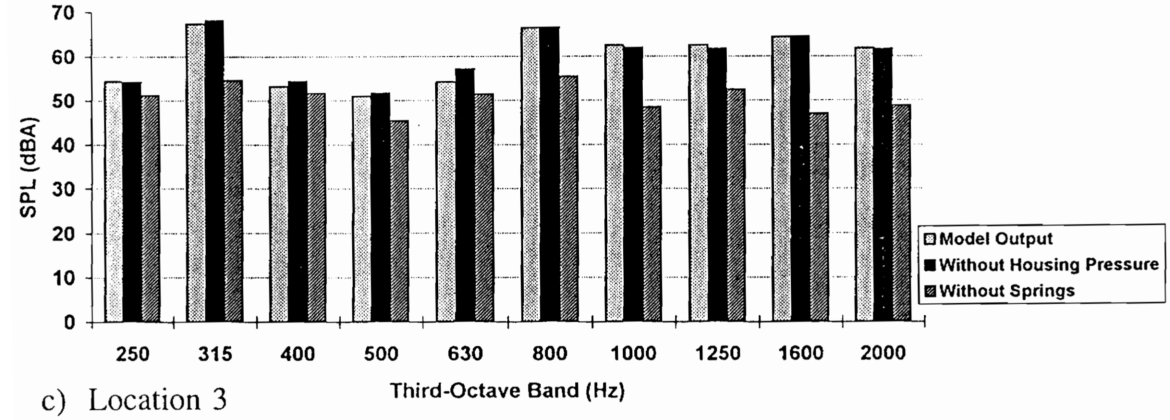

c) Location 3

Fig. 4-9: Model total sound pressure and predicted sound pressure with the housing pressure contribution and the spring contributions shielded separately for the three microphone locations

With this analysis there several unknowns that affect the results. The first is the source of the uncorrelated content in the microphone signal. It could be from transmission paths that were not measured or it could be the reverberant sound energy in the room that takes time to decay. The other unknowns are transmission paths that are not practical to measure, such as the contribution of the shock loop and the moments exerted by each spring. It is assumed that the characteristics of the moments are represented in the triaxial force measurements.

The strong transmission path through the springs is supported by the finite element model of a regular H23A compressor with the support springs modeled with beam elements to preserve the surge behavior possible in the springs. The first 50 modes of the finite element model are presented in Table 4-5. The first column of frequencies are the results of the model solution with ideal springs and the second column is the solution with the springs modeled with beam elements to allow for spring surge. There are a number of spring surge frequencies near the 343, 740, and 970 Hz regions that dominate the sound radiation from the regular H23A compressor. The multiple-input FRF analysis and the FEM analysis point toward spring surge as the dominant transmission path. When the support springs are in surge, there are compression, bending, and torsional waves traveling within the spring and the inertia from this motion will result in the amplification of the excitation force being transmitted across the spring at that frequency. These amplified spring excitation forces then drive the natural modes of the shell. The assumed vibration isolation from the suspension springs only holds true until

Table 4-5: The first 50 modes of the finite element model of the compressor, the natural frequencies with ideal springs, the natural frequencies with meshed springs to allow for surge, and a description of each mode (after [33]).

Mode	[k] Springs Freq., Hz	Meshed-Springs Freq., Hz	Mode Description
1-6	0	0	Rigid Body
7	8.6	18.4	
8	13.3	20.1	
9	14.8	22.2	compressor suspension modes
10	22.2	31.9	
11	26.2	33.6	
12	32.3	35.7	
13	99.4	99.4	shockloop
14	163	163	shockloop
15	208	208	shockloop
16	----	347	top spring
17	----	369	top spring
18	492	493	shockloop
19	----	497	top spring
20	----	504	top spring
21	535	536	shockloop
22	----	627	top spring
23	----	646[1]	side spring, housing M8(3,1)[2]
24	----	652	side spring
25	662	662[1]	modified housing mode M8(3,1)
26	----	685	top spring
27	----	690	top spring
28	726	710[1]	modified housing mode M9(3,1)
29	----	719	top spring
30	----	731[1]	side springs, housing M9(3,1), M10(2,1)
31	----	733	side spring
32	772	747[1]	modified housing mode M10(2,1)
33	----	760	side springs
34	----	777[1]	side springs, housing M9(3,1)
35	----	790	side springs
36	----	808	top spring
37	----	810[1]	all springs, housing M10(2,1)
38	853	854	shockloop
39	874	880[1]	modified housing mode M11(4,1)
40	----	909	top spring
41	----	937	top spring, housing M12(top), M13(4,1)
42	----	968	top spring, housing M12(top)
43	968	977	modified housing mode M12(top)
44	972	971[1]	modified housing mode M13(4,1)
45	----	985	top spring, housing mode M12(top), M13(4,1)
46	1016	1020	shockloop
47	1102	1100	modified housing mode M14(2,1,top)
48	1253	1266	shockloop
49	----	1286	top spring, housing mode M15(5,1)
50	1291	1289	modified housing mode M15(5,1)

[1] Identified housing deflection experimentally

[2] Housing deflection is described by an (n,m) type descriptor, where n corresponds to the circumferential pattern and m corresponds to the axial pattern.

the support springs begin to surge from their own internal resonances.

5.0 OPERATING SHAPE MEASUREMENT

The H23A compressor has strong acoustic radiation at the sixth multiple of the running speed, or 343 Hz. This is well below the structural natural resonance modes determined by experimental modal analysis and finite element modeling. The acoustic intensity measurements at this frequency shown in Fig. 5-1 shows a dipole radiation pattern with the strong intensity at the narrow ends of the compressor shell. The compressor shell vibration pattern at this frequency which produces this intensity may help identify the transmission path which drives the shell. It may also help explain this significant 343 Hz radiation substantially lower than the compressor shell natural modes. This operating vibration shape can be measured with a scanning laser velocimeter along with a lock-in amplifier, a tunable narrow band filter, and a signal generator. The scanning laser velocimeter is a recent development and to our knowledge this is the first time that it has been used to measure an operating vibration shape. Operating shapes measured with the laser velocimeter should be very useful in machinery vibration analysis and diagnostics.

5.1 Setup

The test equipment setup required for measuring the compressor operating

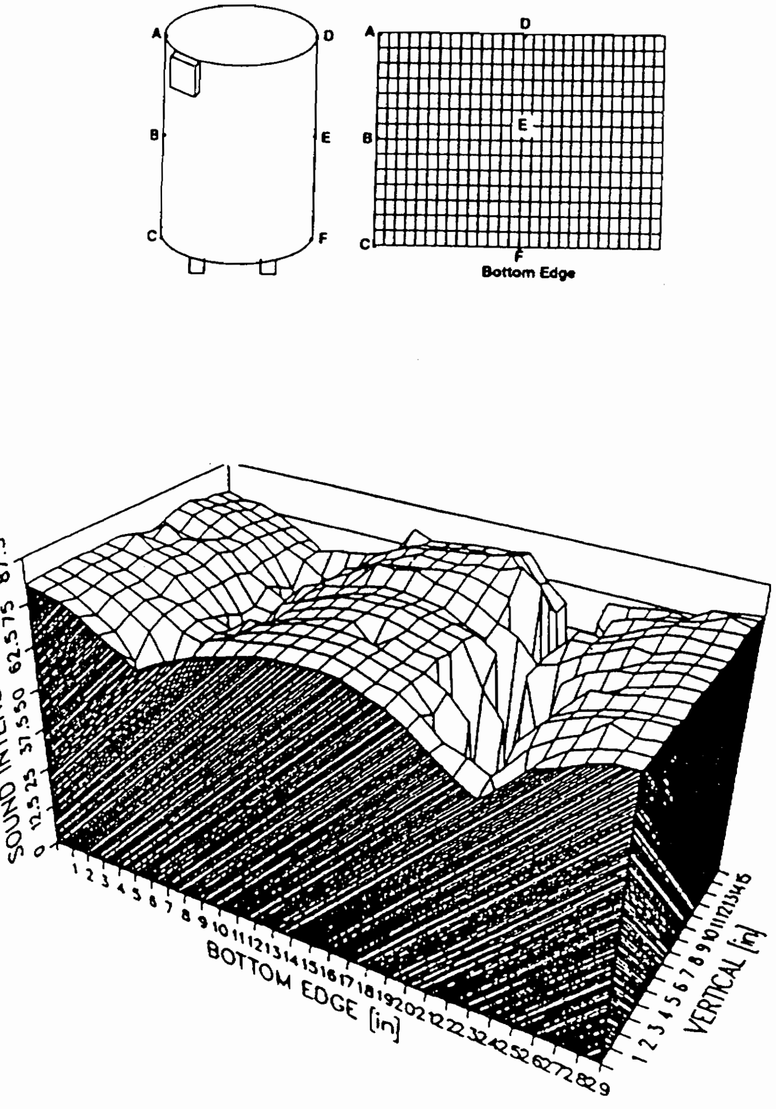

Fig. 5-1: The 343 Hz sound intensity radiation pattern (after [34])

vibration shape is shown in Fig. 5-2. The key component in the system is the Ometron VPI 9000 Laser Velocimeter which uses a He-Ne laser to measure the surface velocities of a vibrating surface. The laser unit has a pair of rotating mirrors which allow the laser beam to be scanned up, down, and side-to-side. This allows the laser to scan virtually any two-dimensional surface geometry. The surface velocities can be measured in more detail and substantially less time than can be achieved using traditional accelerometers. The non-contact measurement with the laser also avoids the problem of surface mass loading which can occur with accelerometers. The VPI laser sensor determines the velocity normal to the laser beam of the moving surface from the doppler frequency shift in the laser beam reflected back from the vibrating surface.

The scanning laser is controlled by Ometron software running on a Hewlett Packard 340 workstation in HP-BASIC. This menu-driven software sets up the scan area geometries, the lock-in amplifier and laser unit settings, displays the results of the scan, and allows limited post processing of the scanned data. The area to be scanned is determined by moving the laser beam with the computer mouse to define the borders of a rectangle, circle, or other type of polygon. Several shapes can be defined within the ±25° scanning limits of the laser and each can be marked for scan or no-scan. The no-scan feature can reduce the time required for a velocity measurement on a structure with substantial open areas within it that are not important to the velocity measurement. The software receives the laser velocity information from the EG&G Lock-in amplifier and controls the laser scanning mirrors over the HP-IB communications bus. The lock-in

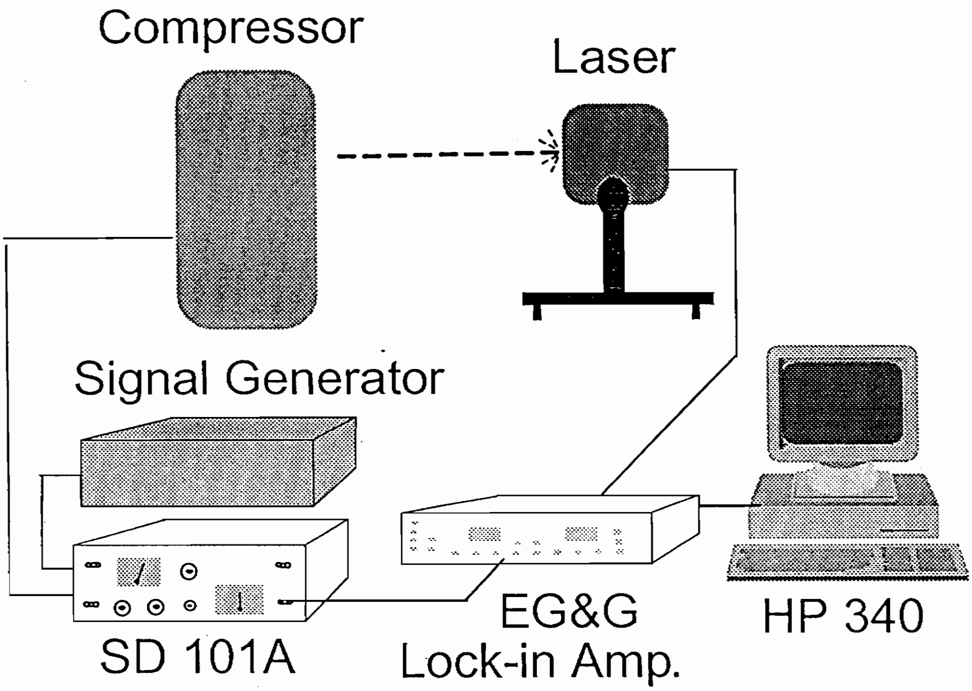

Fig. 5-2: Operating shape measurement test setup

amplifier processes the velocity signal from the laser and determines the portion that correlates with the reference signal input. The lock-in amplifier has adjustable input low-pass, high-pass, and band-pass filters. For normal mode shape measurements the lock-in reference signal is a sine wave from a signal generator. Since this same sine wave is also being used to drive a shaker attached to the structure, the velocity signal from the lock-in amplifier will be the mode shape surface velocity.

Measuring the operating shape of the shell of the reciprocating freon compressor has several complications. The compressor is operating in its normal freon compression cycle and will be vibrating at more than a hundred of the running speed harmonics. A reference signal from the compressor at the harmonic of interest is required to allow the lock-in amplifier to determine the proper operating shape. This was achieved by processing the reference signal with a Spectral Dynamics SD-101A tunable filter from the early seventies. This unit will filter an incoming signal with a narrow-band filter that is 5, 10, 20, or 50 Hz wide with 120 dB/octave attenuation on both sides depending on which crystal filter sets are installed. The center frequency of this narrow-band filter is tuned against a reference sine wave from a signal generator. A narrow filter, such as the 10 Hz or 20 Hz widths, can be tuned to a compressor harmonic to get a fairly clean sinusoidal waveform from a transducer mounted on or in the compressor. This sinusoidal waveform from the SD-101A can then be used as the reference signal for the EG&G Lock-in amplifier. The laser velocity signal can be processed by the lock-in amplifier with the input band-pass filter set to the compressor harmonic and it will determine the portion that correlates with the processed compressor reference signal. This process should yield the compressor operating mode shape at the particular harmonic of the running speed since it is a highly coherent harmonically driven system.

5.2 343 Hz Operating Shape

The laser system was positioned in the four positions shown in Fig. 5-3 for the scans of the operating shape. The scans of the four sides were taken with the compressor operating at the ARI standard operating condition. The top spring triaxial force component normal to the broadsides of the compressor, which is the Top-X force, was used as the reference. This signal was chosen as the reference because the shielding study showed a significant reduction in the predicted sound output at this frequency with the removal of this spring force as a system input for the microphone measurement at location 1. The selection of the reference will affect the phasing of the real and imaginary components in the scans. The reference should not have a significant effect on the magnitudes since the coherence between this top spring transducer signal and the other internal transducer signals are greater than 0.98 at this frequency. Animation of the nine measured forces at 343 Hz show a dominant orbiting lateral force at the top spring. The Top-X force magnitude was 0.088 lbf (0.39 N) and the Top-Y force was 0.138 lbf (0.61 N). Since the compressor should act like a rigid-body at this frequency, the shell should exhibit a similar orbit with little motion at the rubber isolators on the feet. This

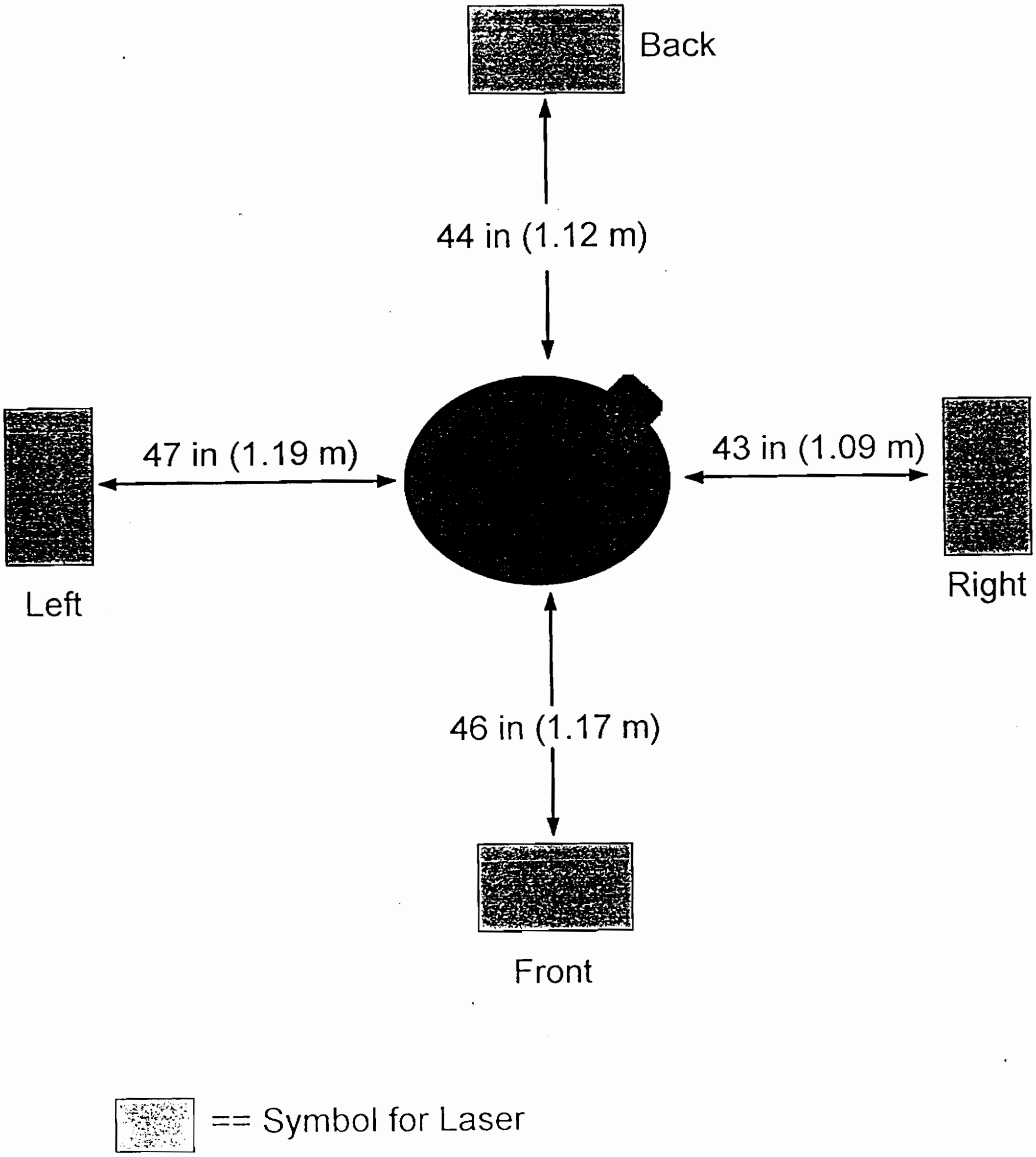

Fig. 5-3: The four measurement positions for the operating shape measurement

may not be easy to identify since there is also a significant pulsation in the housing pressure at this frequency. The laser scan will be the composite of the mechanical and internal acoustic forcing function responses.

The laser velocity scans are shown in Fig. 5-4 with positive velocities shown in red and yellow and negative velocities in blue and green. Since the sound intensity measurements had shown significant sound radiation from the narrow ends, the laser lock-in amplifier phase was adjusted so that the highest velocity region on the right end of the compressor was in phase with the reference signal. The distance between the laser and the compressor will result in slight errors in measuring the normal velocity of the shell in the vertical direction, from the floor to the top of the compressor, but the measured velocities will have a much higher error as the laser scan moves across the compressor face where the shell is curving away from the beam.

These velocity scans show some very interesting behavior at 343 Hz that may explain the significant sound radiation at this harmonic. One important phenomenon to look for is rigid-body shell motion driven by the orbiting forces. This is important because this sound radiation occurs at a frequency where there are no significant natural modes in the structure. The sound radiation can be driven by the forces transmitted through the springs or acoustic modes inside the shell. It could be hypothesized that since the shell has little modal activity in this region, an acoustic mode must be driving the shell. The operating vibration shape must be analyzed for content indicative of mechanical forces and acoustic standing waves.

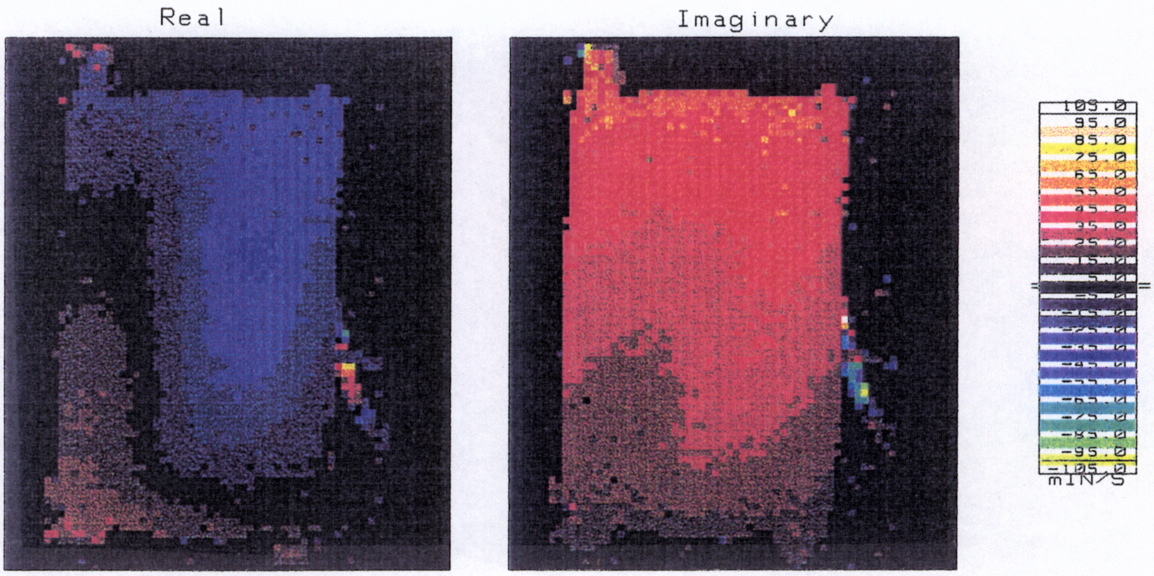

a) Front

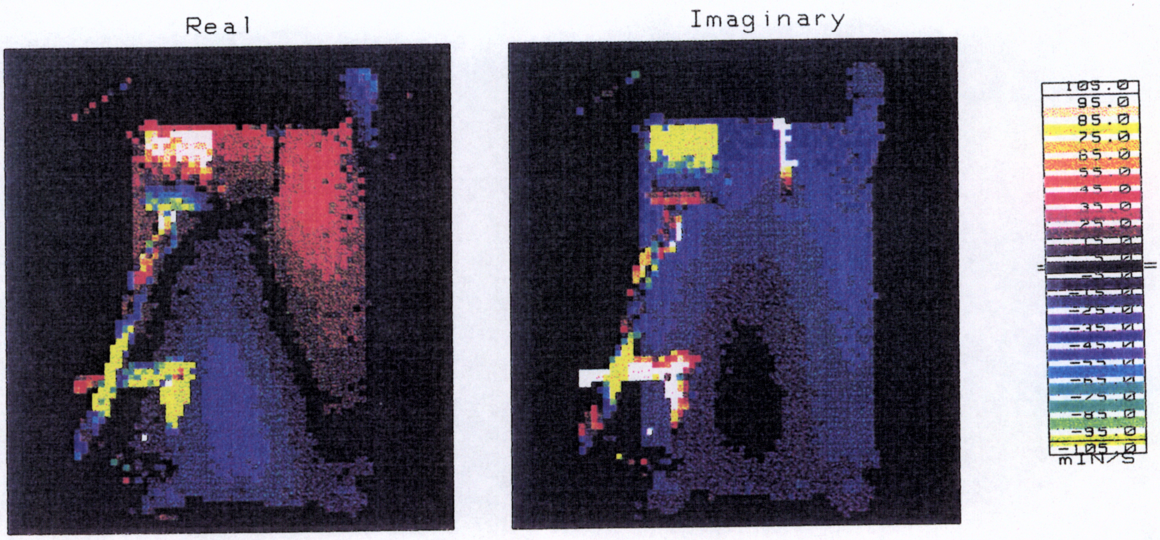

b) Back

Fig. 5-4: The 343 Hz operating velocity vibration shape

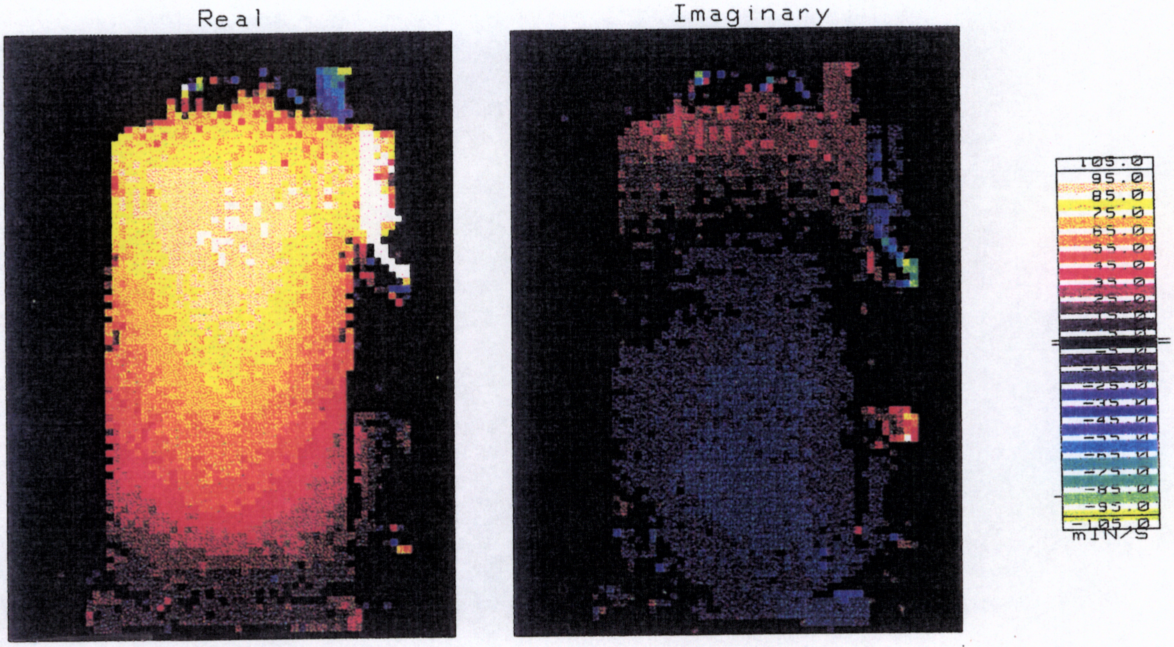

c) Right

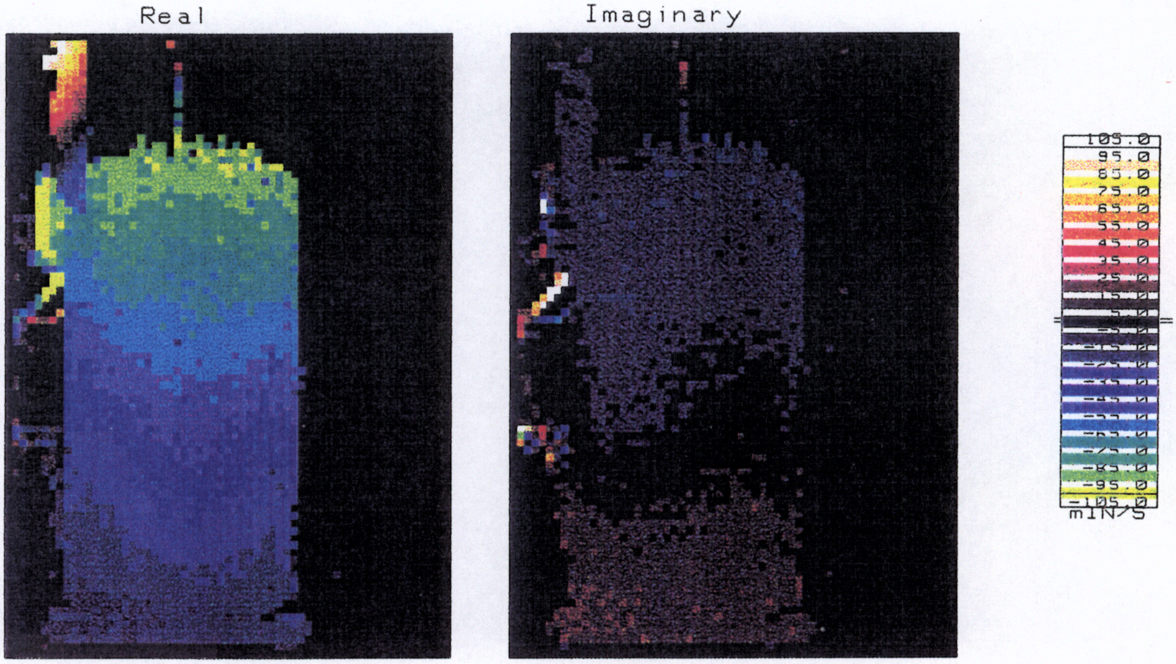

d) Left

Fig. 5-4: continued

The laser scanner was set to yield a positive peak velocity near the top of the right side, which defines the frame of reference for detecting rigid-body motion driven by the orbiting internal compressor assembly. Using this initial calibration to the right side, assuming that this electric motor is turning the crankshaft following the right hand rule, and using the complex circle coordinate system to represent relative phase, the velocity pattern expected for the 343 Hz orbit can be predicted. Because of the initial referencing is to the right side, it should have peak positive real velocity. Following the motor rotation around the complex circle, the front side should have peak positive imaginary velocity, the left side should have peak negative real velocity, and the back should have peak negative imaginary velocity. Since the feet hold the compressor on the floor, the vibration should have increasing velocity from near zero at the floor to a maximum value near the top of the shell. This pattern with the velocities increasing from near zero at the feet to the peak velocities near the top of each side of the compressor can be clearly seen in the velocity plots. This simple view is most accurate near the center of the compressor. Since the velocities are driven by an orbiting phenomenon, there will be some magnitude reduction near the edges of the shell in addition to the shell curvature. This results from the normal velocities of the shell driven by the orbiting forces are shifting phase as the internal compressor assembly rotates from the center of one side to the next.

There is some shell motion that does not correlate well with the rigid-body orbiting and could be driven by the shell internal acoustics. The most distinct activity occurs in the real velocity scan of the front and back sides. This pattern of motion has lower peak velocities than the rigid-body motion and fits the vibration pattern of a circumferential acoustic mode. A circumferential acoustic mode can exist in a toroidal cavity between two cylinders, which is basically shaped like a doughnut when viewed from the top. The circumferential standing wave travels around the toroidal cavity and has a wavelength close to the perimeter of a circle with a radius equal to the average radii of the inner and outer cylinders. The toroidal cavity in the compressor between the motor and the shell is close to the dimensions required for a 343 Hz circumferential standing wave. This fundamental standing wave will have two peak lobes, one pushing the shell out while the other lobe is pulling in. There will be a region of little activity midway between the lobes. One of the peak lobes should be near the excitation point of the standing wave. The primary exciter of the freon in the shell will be the suction process. Most of the freon will be drawn from the shell through the small hole in the motor cap. There is a positive peak in the real velocity near this hole in the motor cap as seen in the back side velocity scan. This location for one lobe of the circumferential acoustic mode makes sense since there is a large amount of freon being drawn through this small hole. There is a broad region of negative real velocity on the opposite side of the shell, shown in the real front side velocity plot. This is the other lobe of the acoustic mode.

There are other velocity patterns present in the velocity scans. These velocity patterns generally have much smaller magnitudes than the orbiting forces and the acoustic mode vibration patterns. Many of the flexible fittings and the power connector cover had very high velocities, but are not the focus of this analysis and have small radiating surfaces. One pattern that draws attention is the peak positive real velocity occurring at a location below the top of the right side. Another pattern is the negative real velocity near the lower spring mount on the back side of the compressor. The high velocity point on the right side of the compressor is very close to the top of the muffler and suction tubes on the inside of the shell. This local peak velocity could be the result of oil splattering off the muffler and suction tubes, or a local coupling effect between the muffler and the shell that is a result of small clearances. The negative velocity at the lower spring mount on the back side of the shell is small and its source is not obvious. It could be driven by orbiting forces rotating about a center point somewhere within the compressor and not at the feet. These orbiting forces could explain much of the other activity shown in the plots that do not fit the orbiting forces or the circumferential acoustic mode.

5.3 Operating Shape Conclusions

The measurement of the compressor operating shape using a scanning laser appeared to be a success. The major motion of the compressor shell reflects the orbiting forces exerted by the internal compressor assembly. The velocities are much higher at the narrow ends of the shell than at the broad sides. This is probably a by-product of the compressor spring suspension system. It will provide much more resistance to the internal compressor assembly rotation toward the broad sides of the compressor than toward the narrow ends. The less stiff top spring has to resist the compressor motion toward the narrow ends, with the resulting forces and moments driving the shell toward the narrow ends. Since the top spring provides most of the resistance against compressor rotation toward the narrow ends, the net moment exerted on the shell at the top spring will be significantly higher than the reaction force exerted by the lower support springs. The vibration pattern from the orbiting forces looked very similar to the acoustic intensity measurements taken on the running compressor. This indicates that the rigid-body motion of the compressor shell, driven by the spring resistance forces, and the ground reinforcement effects are the main contributors to the 343 Hz sound intensity pattern.

An acoustic circumferential mode driving the shell could also be observed. Its peak shell velocities and area of effect were much smaller than the velocities from the orbiting spring forces. The highest velocities were near two diagonal corners, the one between the back and left side, and the opposite one between the right and front side. This vibration pattern does not correlate very well with the dipole behavior shown in the intensity plots. This indicates that the acoustic mode is less significant than the rigid-body motion in driving the sound radiation at this frequency.

6.0 CONCLUSIONS

The MIMO analysis of the compressor shows that the support springs are the primary vibration path to the shell. The acoustic modes do not appear to be a significant contributor in the H23A623 instrumented compressor used in this test, especially in the third-octave bands above 630 Hz. Shielding the spring forces at the three microphone locations yield significant reductions in the predicted microphone sound pressures. The shielding of the housing pressure and spring forces yielded the following predicted sound pressure changes:

• Housing pressure:	0.2 dBA decrease to 0.2 dBA increase
• Top spring:	0.2 - 2.3 dBA decrease
• Lower spring pair:	1.6 - 3.2 dBA decrease
• All springs:	5.6 - 11.0 dBA decrease

Shielding the housing pressure at the three microphone locations had little effect. The 5.6 - 11.0 dBA reductions with all spring forces blocked is the ideal case. Reductions in the 4 - 6 dBA range are more realistic. The 5.6 dBA reduction with all springs blocked at location 1 is 2.9 dBA less than at location 2 and 5.4 dBA less than the 11.0 dBA reduction at location 3. The smaller reduction at location 1 is probably due to an internal acoustic resonance in the 315 Hz third-octave band. This internal resonance prevents the spring force shielding from reducing the 315 Hz third-octave band at this location. Locations 2 and 3 show significant reductions in the 315 Hz third-octave band with the spring forces shielded.

An internal acoustic standing wave does appear to be present at approximately 343 Hz. The acoustic path is not the dominant path because much of the compressor sound pressure is radiated in the third-octave bands above 630 Hz where the spring path dominates. In the MIMO analysis this 343 Hz acoustic mode is important at location 1 but not at locations 2 and 3. The 343 Hz harmonic can be clearly observed in the autospectrum of the housing pressure in Fig. 4-5(j). The pattern of a fundamental circumferential acoustic mode in the shell can also be observed in the operating vibration shape discussed in Chapter 5. The microphone at location 1 was pointed at the region of the shell that is driven by this acoustic mode. The sound pressure generated by this acoustic mode driving the shell dominates the microphone measurement at location 1 at 343 Hz. This is why the spring force shielding has little effect on the 315 Hz third-octave band at location 1. Microphone locations 2 and 3 must see the sound pressure radiated by the rigid body motion driven by the spring forces observed in the operating shape. Internal acoustics may also explain the small effect spring force shielding has on the 630 Hz third-octave band. The second acoustic circumferential mode should occur in this third-octave band. The 630 Hz third-octave band is not a significant sound radiator at the three microphone locations.

The measured forces and analysis results apply to the instrumented compressor. An effort was made to keep the instrumentation from significantly altering the dynamics of the compressor. Comparison with a production H23A623 compressor showed some significant changes in the structural dynamics. The most dramatic was the disappearance of the significant modal activity in the top in the 900-1000 Hz frequency range on the instrumented compressor. This may have reduced the importance of the top spring forces in the instrumented compressor analysis. The acoustic path, particularly the shell internal acoustics, should remain nearly the same. The mechanical transmission path due to the coupling of spring surge and shell modes should be true in both the instrumented and production H23A compressors. The peak frequencies in the spring forces and radiated sound pressure will be different due to the structural dynamic changes. The fifteenth harmonic, which is approximately 860 Hz, is a major peak in eight out of the nine triaxial force measurements. The eleventh harmonic at 630 Hz was also significant in eight out of the nine triaxial force measurements. The modal response of the structure at 630 Hz is much less than it is near 860 Hz, but both are in the frequency region where the instrumented compressor is modally active.

7.0 RECOMMENDATIONS

The spring forces appear to drive most of the sound radiation in the instrumented compressor. Like a normal production compressor, the sound radiation peaks near 343 Hz and again in the 800 Hz to 1200 Hz frequency region. The most dramatic sound reduction could be achieved by attenuating these two frequency regions. The MIMO modeling results show that the springs in combination with a responsive shell drive the 800 Hz to 1200 Hz sound radiation. The 343 Hz peak sound radiation appears to be driven by rigid-body shell motion driven by the top spring forces. There is evidence of an internal acoustic standing wave inside the compressor shell at this frequency. The analysis indicates that effect of the acoustic standing wave at 343 Hz is a smaller and more localized effect than the rigid body motion. The acoustic standing wave appears to be driven by the freon being drawn from the shell through the round hole in the side of the motor cap. Modification of the suction path through the motor cap should help attenuate this standing wave. One possible solution is to increase the number of holes in the motor cap, locating them at points where the pressure pulsations from the suction process are less efficient in driving the circumferential standing wave.

Significant sound reduction can be achieved by changing the modal response of structure, changes in the spring suspension geometry, or modifications to the springs themselves. The structural changes should move the strong natural modes currently near 970 Hz to a higher frequency range. External treatments that add damping to the compressor shell may attenuate the shell response. The effectiveness of the damping treatment is dependent on the existing damping in the shell and the mode shapes. Modification of the support spring geometry should also have a major impact. The support spring locations should be very effective driving the shell modes near 970 Hz. Relocation of the support springs to locations at stiff points in the shell, such as where the top and bottom transition to the side shell, should be effective in reducing the radiated sound level. The spring relocation will reduce the ability of the spring forces to drive the shell modes but may improve the ability of the spring moments to drive the shell modes. Changes in the layout of the three spring support system, or possibly an additional spring, should reduce the sound radiation in the 315 Hz third-octave band. The compressor orbiting force exerted through the top spring appears to be the dominant source of sound radiation at this frequency. The other option is to modify the individual support springs to reduce the surge and add damping. There are two potential approaches that are readily available. One is to change the geometry and construction of the support springs to raise the surge frequencies. This will greatly reduce the vibration transmission to the shell through the springs near 1000 Hz. The other approach is to add damping to the spring so that the vibrational energy is absorbed within the spring instead of transmitted to the shell. This can be achieved though an elastomer element serving as a spring or sandwiched between the spring and the structure. Another method of adding damping would be to use another form of spring, such as one made of wire rope where the friction between the strands absorbs the vibrational energy.

For compressor models already in production, either external shell treatments that increase the damping or spring modification are the best alternatives. Neither should require significant retooling and can be added to the existing production process. The spring modification should be the most effective since their surge modes amplify the forces exerted by the compressor. Redesigning the springs so that the surging is less of a problem while keeping most of the existing spring interface hardware on the compressor and shell should be less difficult than redesigning the compressor.

REFERENCES

1. Agee, B., Burnett, R., Cardany, K., Gardner, B., Kelly, A., Smith, J., Vipperman, J., Wallace, K., Hurst, C.J., Knight, C.E., and Mitchell, L.D., *Investigation of the Potential for Noise Reduction of a Reciprocating Compressor*, Project Report, Virginia Polytechnic Institute and State University, 1990.

2. Bendat, J.S. and Piersol, A.G., *Random Data*, Wiley-Interscience, New York, 1986. TA340 B43

3. Bendat, J.S. and Piersol, A.G., *Engineering Application of Correlation and Spectral Analysis*, Wiley-Interscience, New York, 1980. TA340 B427

4. Halvorsen, W.G. and Bendat, J.S., "Noise Source Identification Using Coherent Output Power Spectra", *Sound and Vibration*, Vol. 9, No. 8, August 1975, pp. 15-24. QC 221 S6x

5. Dodds, C.J. and Robson, J.D., "Partial Coherence in Multivariate Random Processes", *Journal of Sound and Vibration*, Vol. 42, No. 2, 22 Sept. 1975, pp. 243-249. QC 221 J6

6. Romberg, T.M., "An Algorithm for the Multivariate Spectral Analysis of Linear Systems", *Journal of Sound and Vibration*, Vol. 59, No. 3, 8 Aug. 1978, pp. 395-404. QC 221 J6

7. Bendat, J.S., "Statistical Errors in Measurement of Coherence Functions and Input/Output Quantities", *Journal of Sound and Vibration*, Vol. 59, No. 3, 8 Aug. 1978, pp. 405-421. QC 221 J6

8. Seybert, A.F., and Hamilton, J.F., "Time Delay Bias Errors in Estimating Frequency Response and Coherence Functions", *Journal of Sound and Vibration*, Vol. 60, No. 1, 8 Sept. 1978, pp. 1-9. QC 221 J6

9. Bendat, J.S., "Modern analysis procedures for multiple input/output problems", *J. Acoust. Soc. Am.*, Vol. 68, No. 2, Aug. 1980, pp. 498-503. QC 221 A4

10. Trethewey, M.W. and Evensen, H.A., "Evaluation of the Structural Noise Sources of a Four-Piece Gravity Drop Forge Hammer by Residual Spectrum Techniques", *Internoise 80 Proceedings*, Miami, FL, Dec. 8-10, 1980, pp. 487-490. TD 892 I58

11. Trethewey, M.W., and Evensen, H.A.,"Identification of Noise Sources of Forge Hammers During Production: An Application of Residual Spectrum Techniques to Transients", *Journal of Sound and Vibration*, Vol. 77, No. 3, 8 August 1981, pp. 357-374. QC 221 J6

12. Trethewey, M.W., Evensen, H.A., and Shapton, W.R., "Combination of Multiple Input Models and Experimental Modal Analysis for Identification of Structural Noise Generating Mechanisms: With Application to Forge Hammers", *Noise Control Engineering Journal*, Vol. 21, No. 3, Nov.-Dec. 1983, pp. 89-102. TD 891 N65

13. Trethewey, M.W. and Evensen, H.A., "Development and application of multiple-input models for structural noise source identification of forge hammers. Part I: Development", *J. Acoust. Soc. Am.*, Vol. 75, No. 4, April 1984, pp. 1092-1098. QC 221 A4

14. Trethewey, M.W. and Evensen, H.A., "Development and application of multiple-input models for structural noise source identification of forge hammers. Part II - Application", *J. Acoust. Soc. Am.*, Vol. 75, No. 4, April 1984, pp. 1099-1104. QC 221 A4

15. Trethewey, M.W., *Establishment of Multiple Input Modeling Techniques for Transient Noise Source Identification: With Application to Structural Sources of Forge Hammer Noise*, Ph.D. Dissertation, Michigan Technological University, 1981.

16. Chung, J.Y., Crocker, M.J., and Hamilton, J.F., "Measurement of frequency responses and the multiple coherence function of the noise-generation system of a diesel engine", *J. Acoust. Soc. Am.*, Vol. 58, No. 3, Sept. 1975, pp. 635-642. QC 221 A4

17. Alfredson, R.J., "The Partial Coherence Technique for Source Identification on a Diesel Engine", *Journal of Sound and Vibration*, Vol. 55, No. 4, 22 Dec. 1977, pp. 487-494. QC 221 J6

18. Price, S.M., and Bernhard, R.J., "Virtual Coherence: A Digital Signal Processing Technique for Incoherent Source Identification", *Proc. of 4th Int. Modal Anal. Conf.*, Los Angeles, CA, Feb. 3-6, 1986, pp. 1256-1262. TA 654 I57

19. Leuridan, J., Roesens, D., and Otte, D., "Use of Principal Component Analysis for Correlation Analysis between Vibration and Acoustical Signals", *ISATA 87*, Florence, Italy, May 11-15, 1987, pp. 488-504. TL 285 I54

20. Otte, D., Sas, P., and Snoeys, R., "Use of Principal Component Analysis and Virtual Coherence for Dominant Noise Source Identification", *Proc. of 2nd Intnl. Sem. on Noise Identf. and Numer. Mthds. in Acoustics*, Sept. 1987, pp. 1-10.

21. Ufford, D.A. and Bernhard, R.J., "A Signal Processing Technique to Identify the Number of Incoherent Sources in a System", *Internoise 89 Proceedings*, Newport Beach, CA, Dec. 4-6, 1989, pp. 1123-1128. TD 892 I58

22. Ufford, D.A., and Bernhard, R.J., "An Investigation of the Number of Incoherent Sources in an Internal Combustion Engine", *Internoise 90 Proceedings*, Gothenburg, Sweden, Aug. 13-15, 1990, pp. 1061-1064. TD 892 I58

23. Mitchell, L.D., Cobb, R.E., Deel, J.C., and Luk, Y.W., "An Unbiased Frequency Response Function Estimator", *Proc. of 5th Int. Modal Anal. Conf.*, London, England, April 6-9, 1987, pp. 364-373. TL 285 I54

24. Cobb, R.E., and Mitchell, L.D., "Estimation of Uncorrelated Content in Experimentally Measured Frequency Response Functions Using Three Measurement Channels", *Mechanical Systems and Signal Processing*, Vol. 4, No. 6, Nov/Dec 1990, pp. 449-461.

25. Rocklin, G.T., Crowley, J., and Vold, H., "A Comparison of H_1, H_2, and H_v Frequency Response Functions", *Proc. of 3rd Int. Modal Anal. Conf.*, Orlando, FL, Jan. 28-31, 1985, pp. 272-278. TL 285 I54

26. Wicks, A., and Vold, H., "The H_s Frequency Response Estimator", *Proc. of 4th Intl. Modal Anal. Conf.*, Los Angeles, CA, Feb. 3-6, 1986, pp. 897-899. TL 285 I54

27. Anonymous, "Operating Instructions - Quartz Force Transducer for 3 Components Type 9251A", Kistler Instrument Corporation, B6.9251e ed. 12.68.

28. Bristol Compressors, Inc., Production Drawing No. 230050, April 25, 1989.

29. Bristol Compressors, Inc., Production Drawing No. 209022, December 11, 1989.

30. Young, D.L., and Mitchell, L.D., "Static and Dynamic Calibration of a Triaxial Force Gage for Monitoring the Structureborne Forces Within a Freon Compressor", *Proc. of 1992 International Compressor Engineering Conference at Purdue*, July 14-17, 1992, Purdue University, West Lafayette, IN, pp. 779-787.

31. Soom, Andres, and Kubler, John, "Measurement of Dynamic Forces", Kistler Instrument Corporation Paper, K20.220.

32. Wilson, Charles E., *Noise Control*, Harper & Row, New York, 1989.

33. Kelly, A.D., and Knight, C.E., "Helical Coil Suspension Springs in Finite Element Models of Compressors", *Proc. of 1992 International Compressor Engineering Conference at Purdue*, July 14-17, 1992, Purdue University, West Lafayette, IN, pp. 779-787.

34. Smith, J.P., Kiel, D.H., and Hurst, C.J., "Intensity Measurements and Radiated Noise Reduction for a Freon Compressor", *Proc. of 1992 International Compressor Engineering Conference at Purdue*, July 14-17, 1992, Purdue University, West Lafayette, IN, pp. 947-954.

APPENDIX A: COMPRESSOR INSTRUMENTATION

Location	Transducer Type	Model	Serial Number
Top Spring	Triaxial Force	Kistler 9251A	157181
Front Spring	Triaxial Force	Kistler 9251A	439440
Back Spring	Triaxial Force	Kistler 9251D	50090
Housing	Pressure	PCB 116A	1842
Top Cylinder	Pressure	PCB 113A22	6259
Bottom Cylinder	Pressure	PCB 113A22	6260
Discharge Muffler	Pressure	PCB 113A24	6261
Suction	Pressure	PCB 113A24	6262
Shock Loop	Accelerometer	Kistler 8626	C22382
External Microphone	Sound Level Meter	B&K Type 2331	

APPENDIX B:

MEASURED TRANSDUCER LINEAR SPECTRA

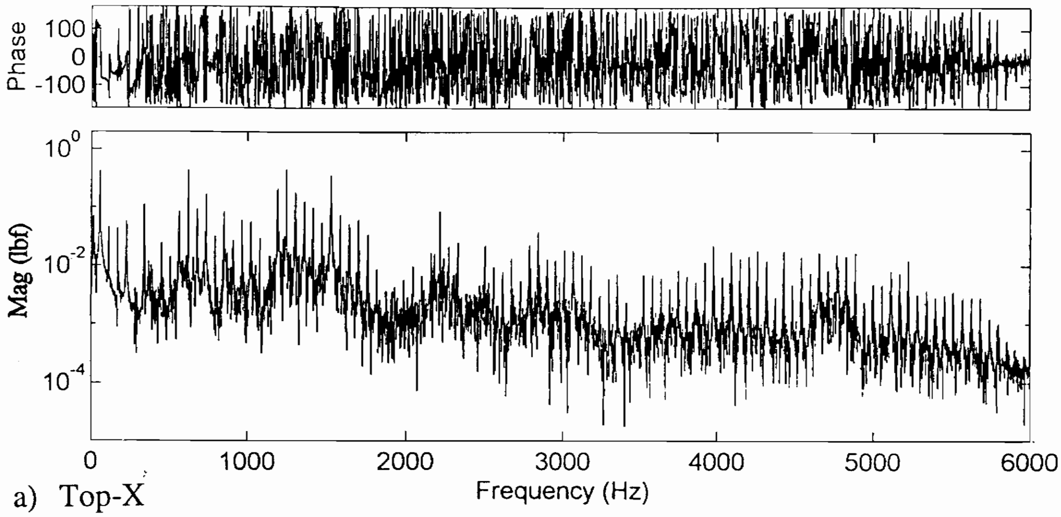

a) Top-X

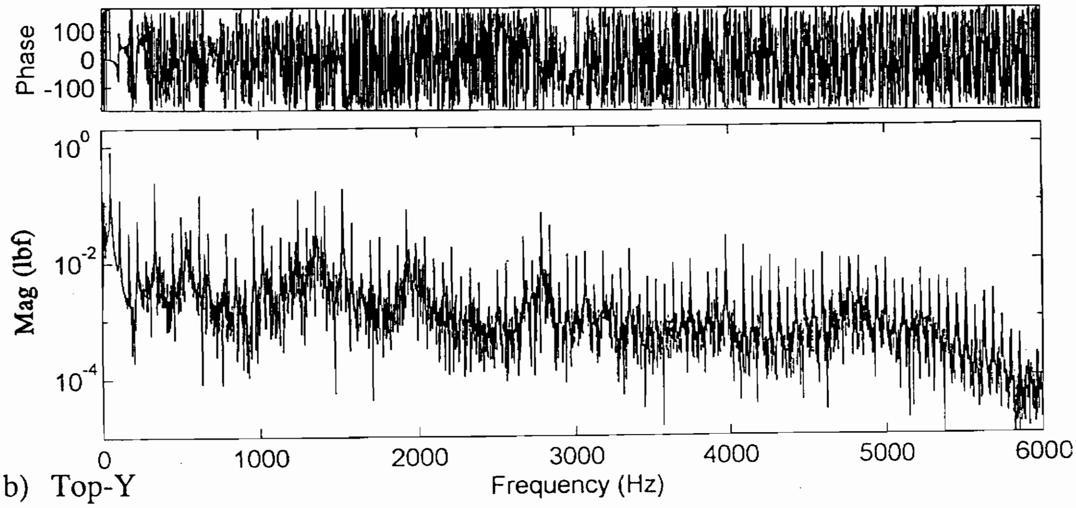

b) Top-Y

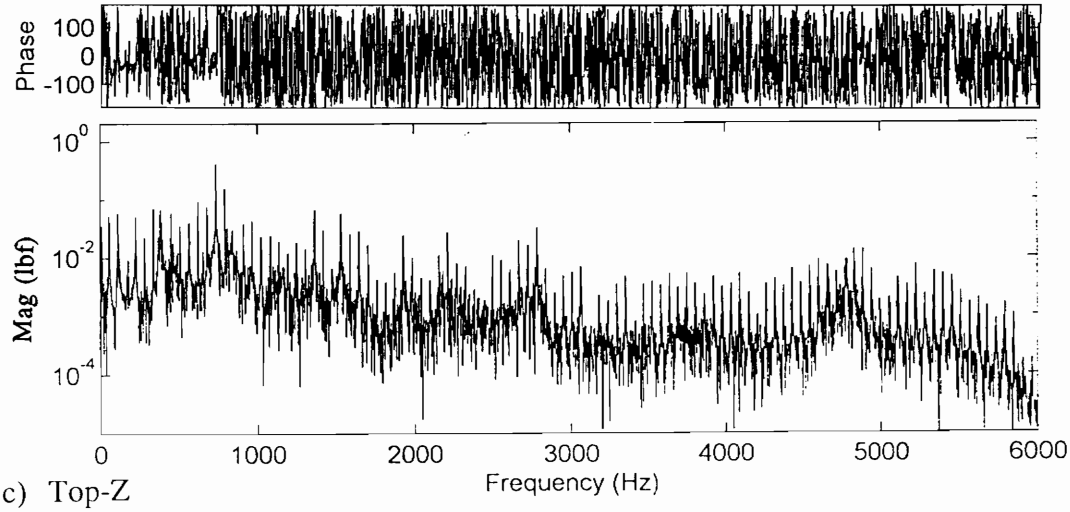

c) Top-Z

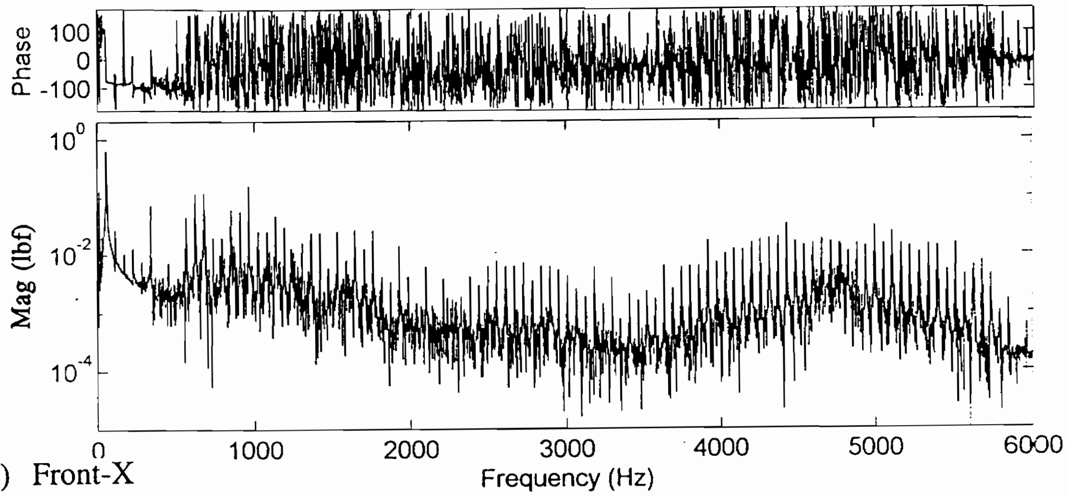

d) Front-X

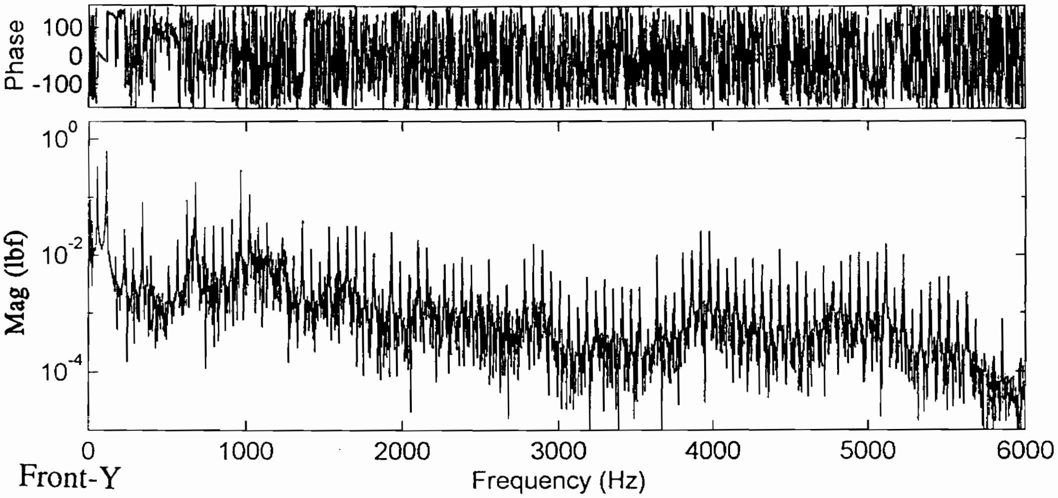

e) Front-Y

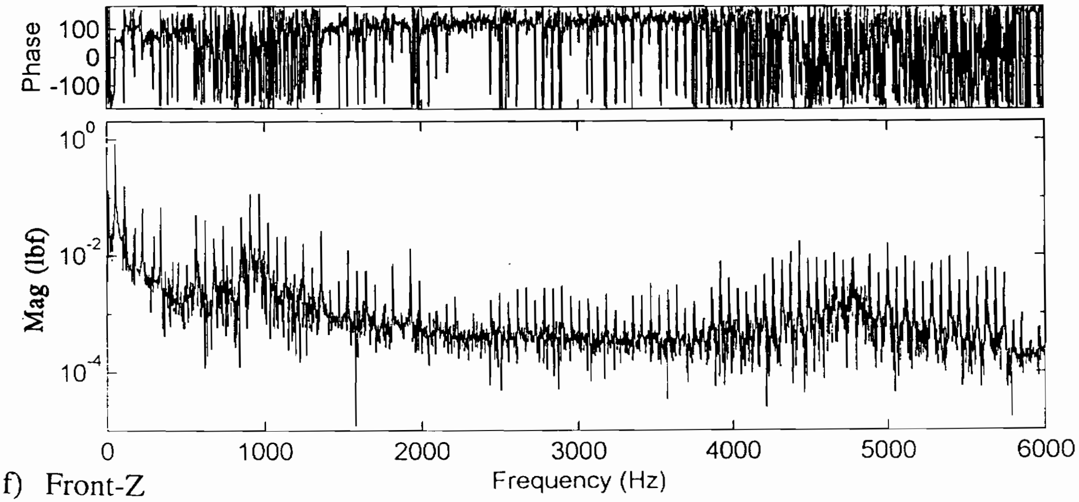

f) Front-Z

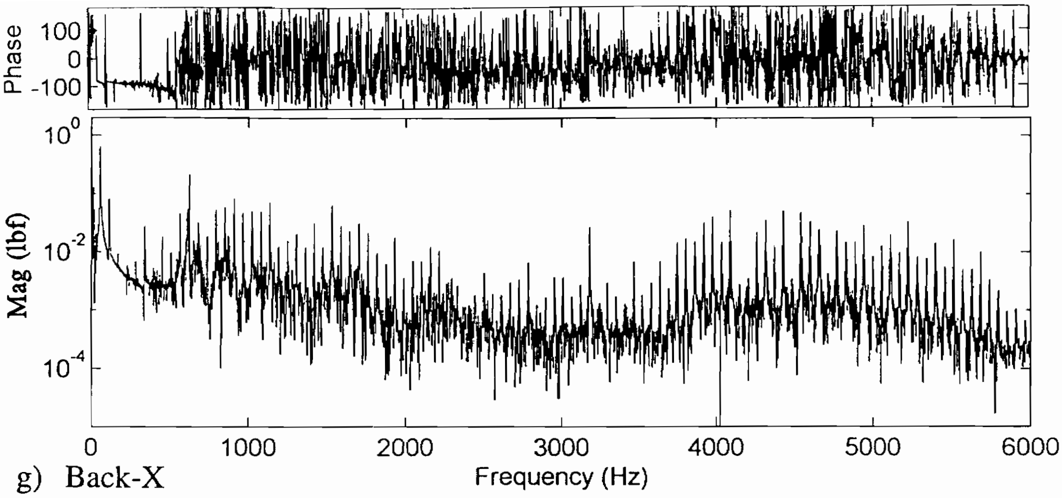

g) Back-X

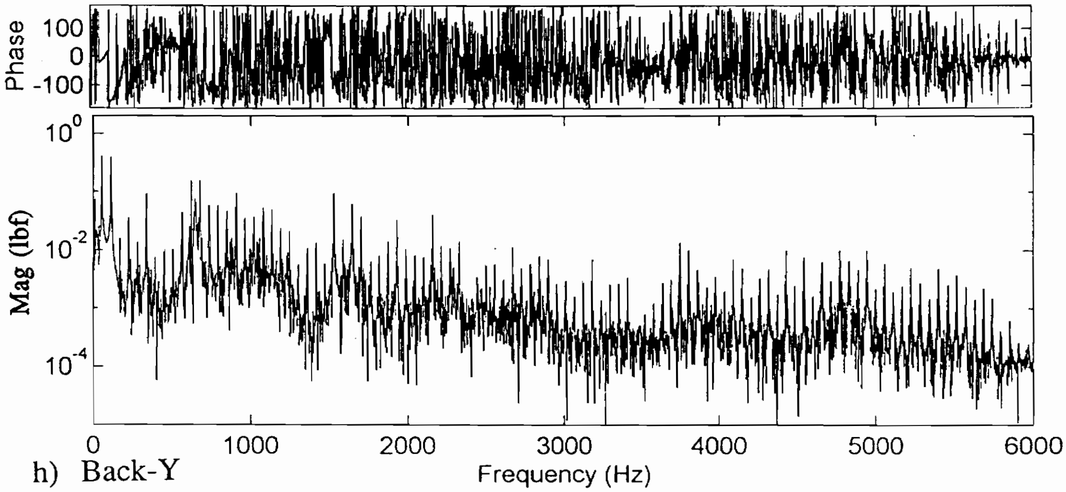

h) Back-Y

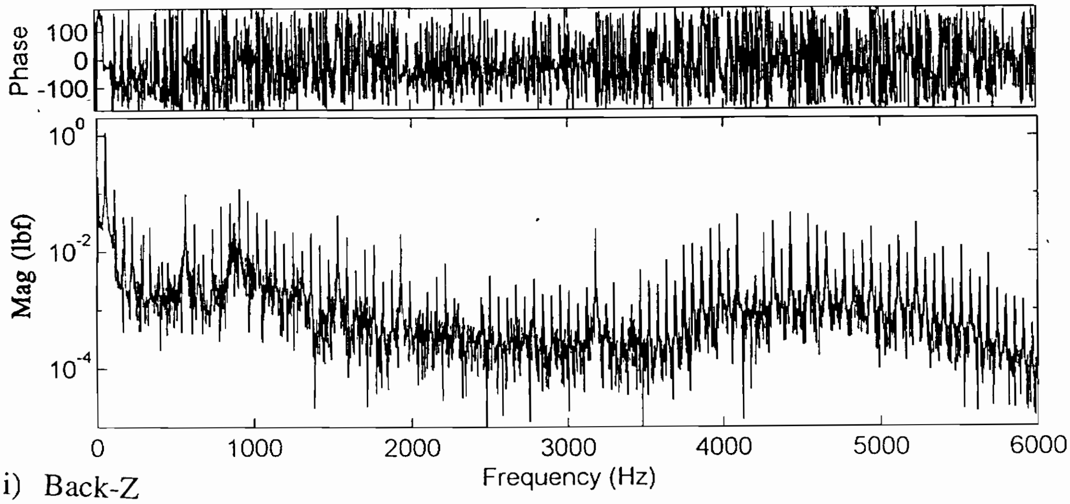

i) Back-Z

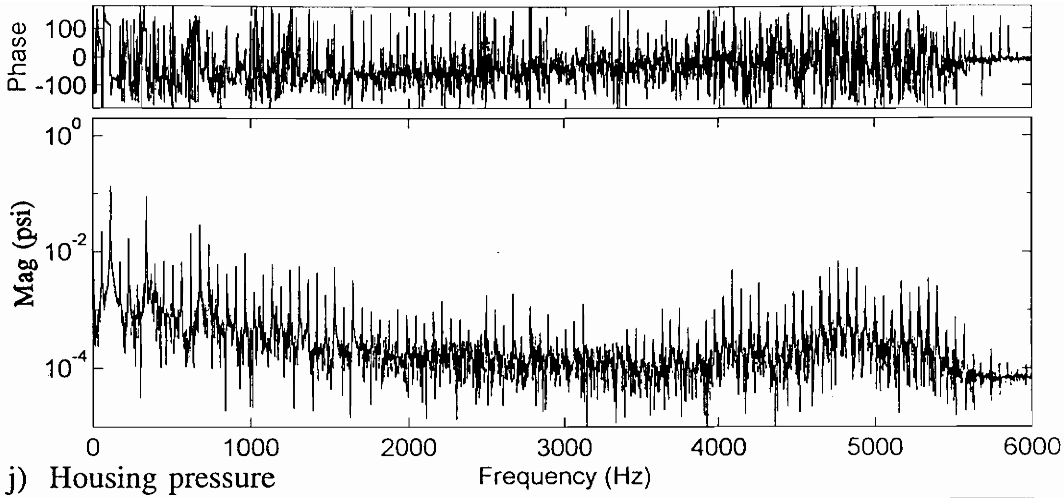

j) Housing pressure

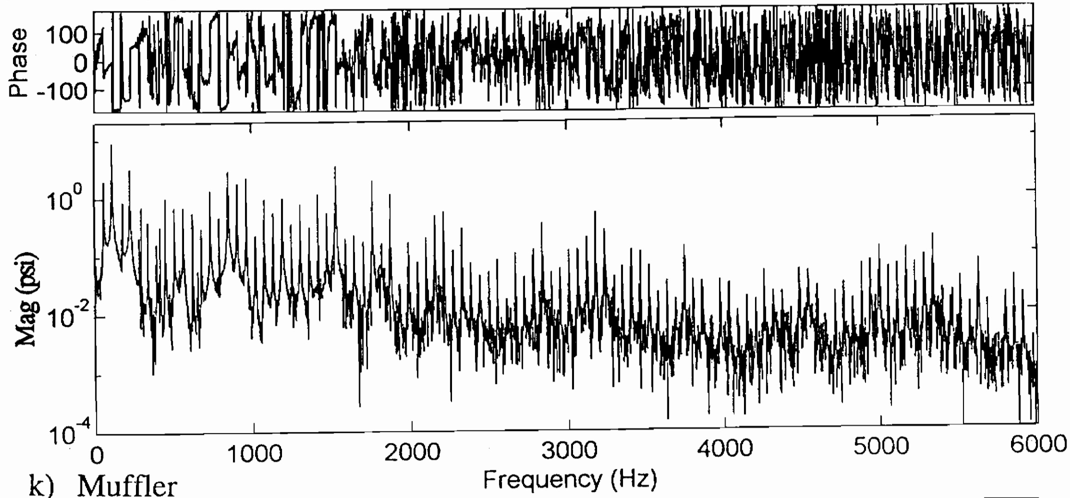

k) Muffler

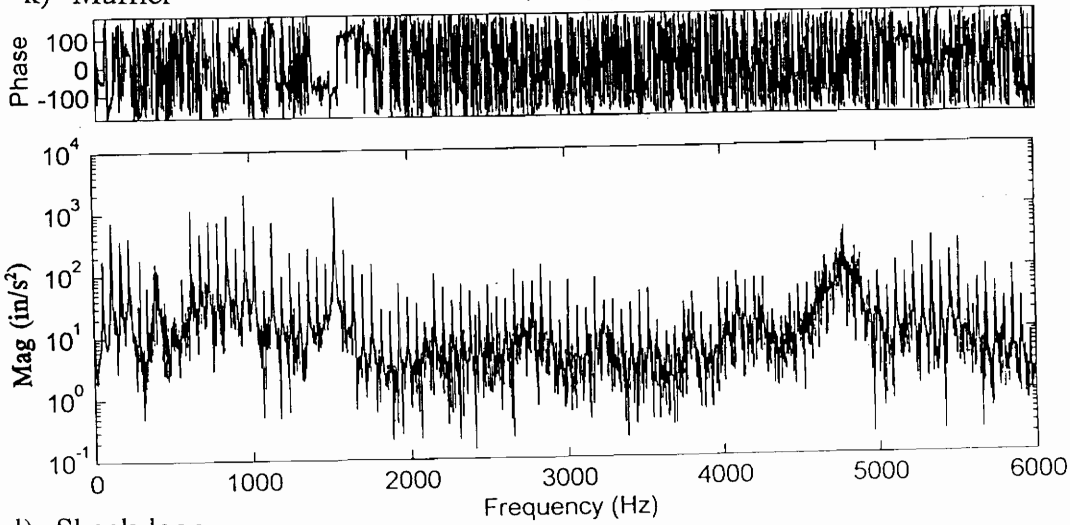

l) Shock loop

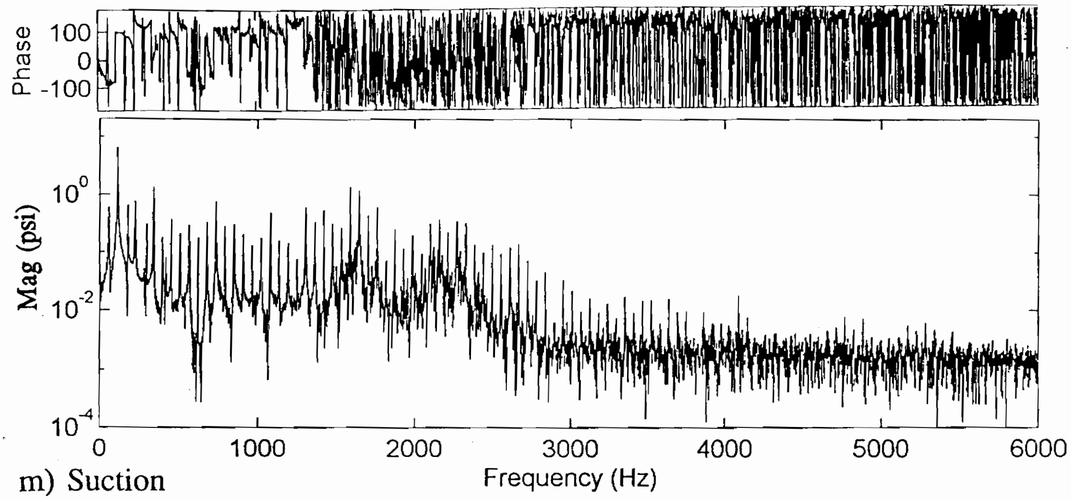

m) Suction

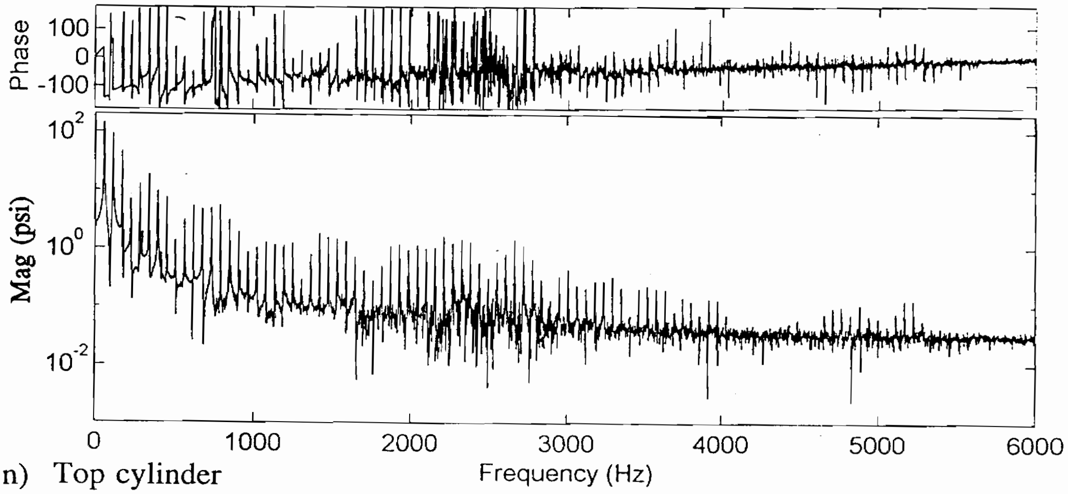

n) Top cylinder

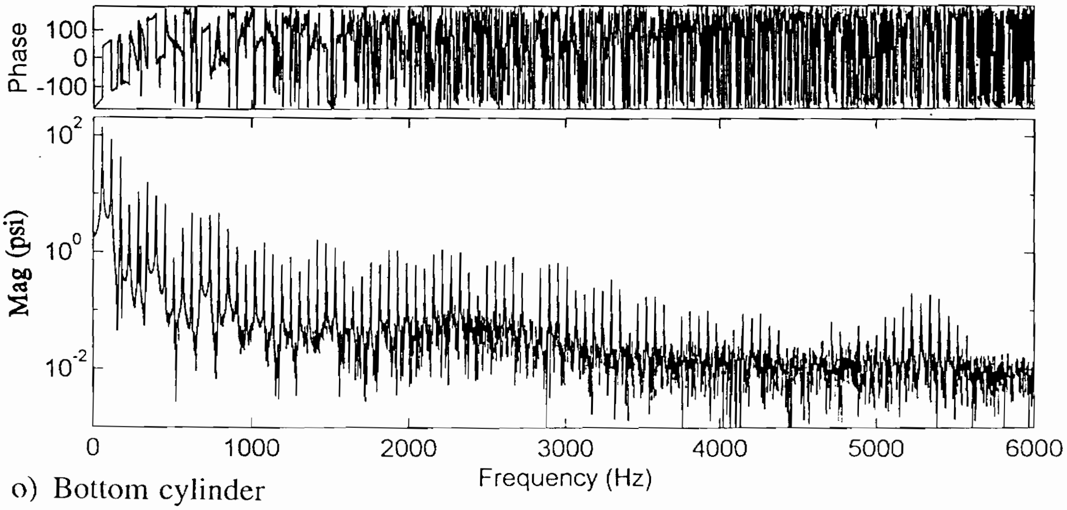

o) Bottom cylinder

VITA

The author was born on October 19, 1966 in Columbia, South Carolina. He grew up in Greensboro, North Carolina graduating from Western Guilford High School in 1985. That fall he started Virginia Tech and received a B.S. degree in Mechanical Engineering in May 1990. The pursuit of a M.S. degree in Mechanical Engineering began in the Fall of 1990. In August 1992, he started work as a research engineer at the United Technologies Research Center in East Hartford, Connecticut.

David L. Young, Jr.